Optimization of MARS Scanners for Material Imaging of Biological Samples

Joseph Leo Healy

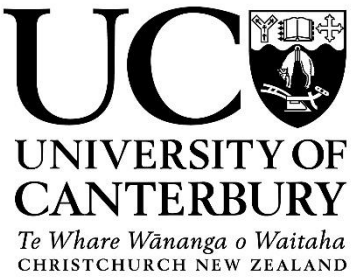

A thesis submitted in partial fulfilment

of the requirements for the Degree of

Doctor of Philosophy

Department of Biological Sciences,

University of Canterbury,

Christchurch, New Zealand

2018

Table of Contents

Acknowledgements

My wife, Tara, and children, Etta and Henry, are the calm in my storm and I thank them for all of their support and love.

My parents, John and Dorothy, were/are the best, that's it. The same goes for my siblings Teresa, Kate and my late brother Tim (I wish you were here).

I also thank the rest of my extended family, in-laws and friends that have given me their love, friendship and help along the way.

Associate Professor Steven Gieseg, Professor Phil Butler and Professor Anthony Butler have provided constant support and patience throughout my studies as my supervisory committee. Without their understanding and help, this thesis would not have been possible.

My appreciation goes to the entire MARS team. The progression to a commercial product is marked with many milestones and all of them are hard to get to. I would like to express my admiration to the entire team for its work and the help I have received along the way. By name I would like to thank former MARS teammates Judy Mohr, Derek Smithies and Kishore Rajendran. Within the current team I would like to thank Niels de Ruiter, Alex Chernoglazov, Mike Walsh, Robert Doesburg, Lieza Vanden Broeke and Brian Goulter. For their help, hours of good scientific conversation and friendship I owe special thanks to Hannah Prebble, Ali Atharifard, Muhamad Shamshad, Marzieh Anjomrouz, Mahdieh Moghiseh, Aamir Raja, Nigel Anderson, Stephen Bell and Raj Panta.

The members of Steven Gieseg's Free Radical Biochemistry lab also deserve mention. Former member Tejraj Janmale was my first mentor upon my arrival at the University of Canterbury and helped me to settle in. Sean Cross and Izani Othman are other former members who helped me in the lab. Greg Parker was of great assistance in handling the macrophage culturing for Section 4.6.

Others that helped me along the way include: David Collings, Graeme Bull, and Manfred Ingerfeld formerly of the University of Canterbury, Matthew Walters, Craig Galilee, and Nicole Lauren-Manuera at the University of Canterbury; Aaron Dyer, Katie Saunders, Robin Fraser and Leigh Ellmers current and former staff at the University of Otago, Christchurch, Professor Justin Roake of the University of Otago, Christchurch and the Canterbury District Health Board, and finally, Catherine Williamson at Christchurch Women's Hospital.

Abstract

Properly calibrated, a spectroscopic x-ray computed tomography (CT) machine can perform quantitative chemistry. The MARS scanner is built around the Medipix family of photon counting, energy discriminating x-ray detectors. A MARS image is a material representation of a volume reconstructed from spectral x-ray projections. I used atherosclerosis and cancer models to show that MARS images can be used to identify spatial and material traits of disease. For atherosclerosis, I simulated clinical human scans using photons from ~30 to 120 keV. I scanned excised carotid plaques and produced MARS images of a necrotic lipid core with spotty calcifications, which are indicative of plaques vulnerable to rupture. These images were confirmed with histological analysis. Plaques submerged in gadolinium contrast agent, to mimic contrast enhanced angiography, showed that the lipid and calcium signals were maintained. In mice, I demonstrated the simultaneous identification of lipid, calcium, and three contrast agents, gold, iodine and gadolinium. This opens the possibility of targeting three different traits of interest while maintaining the intrinsic material information. I also demonstrated tumour detection using intravascular injection of 15 nm gold nanoparticles in a mouse infected with a sub-dermal Lewis lung carcinoma.

Both the detector and the machine are young technologies requiring extensive testing and adjustment. So, to achieve the results described above, I spent great effort on machine and protocol optimization.

I developed automated pixel masking software and the associated graphical user interface (GUI) that identifies unreliable pixels and inhibits them on the MARS camera. This system was modified and adapted for pixel masking of raw data before reconstruction by other MARS team members and a patent application has been submitted. I helped develop a technique to measure the energy offset of each counter from the global energy threshold chosen by the user. This produces more precise energy discrimination and may be used to improve material reconstruction in future MARS versions. I also lead the initial attempt to develop an automated foil fluorescence energy calibration technique. This work lead to a model to estimate the optimal foil thickness needed for each calibration material and the number of fluorescence photons emitted.

Material calibration is also required. I helped develop and manufactured the current commercial versions of the MARS calibration phantoms. I tested material decomposition using these phantoms and helped develop a simple system for optimizing protocol energy thresholds for simultaneous identification of multiple k-edge containing materials.

I have contributed software and hardware that is included in the commercial release of the MARS scanner. My work appears in 16 journal or conference publications, with two more currently in preparation. I have presented posters or given talks at domestic and international conferences.

I have improved the function and understanding of MARS scanners through pixel masking, energy and material calibration analyses, and threshold and protocol optimization. My work helps show that MARS images will provide a new valuable tool for clinicians in assessing disease, injury and the treatment of both. Quantitative location of materials can help to identify atherosclerosis and cancer. As targeted contrast agents are developed, physiological, histological and biochemical traits will be identifiable with this non-invasive imaging technique.

Glossary and Abbreviations

- **ART**: Algebraic Reconstruction Technique. Used in CT reconstruction.
- **Atherosclerosis**: a disease in which fatty lesions called plaques develop in the innermost layer of artery walls.
- **ASIC**: Application specific integrated circuit. A circuit built for a specific purpose. The Medipix chip is an ASIC for spectral imaging
- **AuNPs**: Gold Nanoparticles
- **Cancer**: Cancer is the uncontrolled proliferation of native cells that can spread to neighbouring tissues, sometimes metastasising to varied locations throughout the body
- **CdTe**: Cadmium telluride. A semiconductor used as an X-ray sensor
- **CZT**: Cadmium zinc telluride. A semiconductor used as an X-ray sensor
- **CERN**: European Organization for Nuclear Research.
- **Contrast to noise ratio**: a measure of image quality using contrast between two regions and the noise
- **CSM**: Charge Summing Mode. A mode of operation available in the Medipix3RX that corrects for charge sharing across pixels.
- **CT**: Computed Tomography. A mathematical technique used in X-ray imaging to reconstruct cross sections of a sample
- **CVD**: Cardiovascular Disease. Any disease that affects the cardiovascular system. Atherosclerosis is a form of CVD.
- **DAC**: Digital-to-Analog Converter. An electrical device that turns a digital number into an analog value
- **Dual Energy CT**: a CT technique that creates two datasets, each representing a different energy regime for the input beam. It can use two different sources, or two different detectors or the same source with rapid kVp switching
- **FWHM**: Full Width Half Maximum. A measure of the spread of a function that gives the difference between the values of the independent variable on either side of the function at a value of the dependent variable that is half of its maximum value
- **GaAs**: Gallium arsenide. A semiconductor used as an X-ray sensor
- **GUI**: Graphical User Interface.
- **HU**: Hounsfield Unit. A linear transformation of measured linear attenuation coefficients in a CT scan. The transformation forces water's attenuation value to be 0 HU and air's attenuation value to be -1000 HU

- **K-edge**: a sudden increase in X-ray attenuation of an atom occurring when increasing X-ray energy matches the binding energy of the K shell electrons
- **kVp**: Peak Kilovoltage. The maximum voltage across the anode and cathode of an X-ray tube. It determines the maximum photon energy emitted by the tube.
- **Linear Attenuation Coefficient**: The fraction of an incident beam of photons that is absorbed or scattered per unit thickness of the absorber
- **MARS**: Medipix All Resolution System. MARS Bioimaging Ltd. is a company based in Christchurch dedicated to producing medical imaging technologies with the Medipix chip
- **MD**: Material Decomposition. A process of turning spectral X-ray attenuation data into material images.
- **NIST**: National Institute of Standards and Technology
- **Noise Floor**: A DAC value for the global low threshold DAC below which a counter begins to count even with no X-ray input. The DAC value corresponds to a photon energy below which the counter low thresholds cannot be set.
- **ODD**: Object to Detector Distance. The distance from the centre of rotation of the rotating gantry to the surface of the X-ray sensor layer in the camera
- **SDD**: Source to Detector Distance. The distance from the focal spot on the X-ray tube anode to the surface of the X-ray sensor layer in the camera. It is the sum of the ODD and the SOD.
- **SOD**: Source to Object Distance. The distance from the focal spot on the X-ray tube anode (the source of X-rays) to the centre of rotation of the rotating gantry.
- **SNR**: Signal to Noise Ratio. A measure of the signal quality of a data set
- **Spectral Imaging/CT**: Energy differentiated X-ray attenuation measurements in more than two energy bins, acquired simultaneously.
- **SPM**: Single Pixel Mode. A mode of operation in Medipix3RX in which each pixel operates independently. Therefore, there is no correction for charge sharing as in CSM.
- **ST**: Soft Tissue. In this thesis, a soft tissue voxel has only water and lipid components in the material decomposition.
- **Threshold Equalization**: The process of adjusting each pixel in the Medipix3RX chip to respond to energy in the same way.
- **Voxel**: A voxel, or volume element, is the three dimensional image counterpart of a pixel in a two dimensional image.
- **XRF**: X-ray Fluorescence. An X-ray photon emitted when an electron falls from a higher energy level to a lower one after the lower energy electron was ejected from the atom

- **Z**: Atomic Number. The number of protons in the nucleus of an atom. For this thesis, a high Z voxel in the material decomposition receives a concentration for two materials: water and one of either calcium, iodine, gadolinium or gold. No lipid value is ever assigned.

Scientific Contributions

Commercialized Outputs

1) Camera pixel inhibition masking algorithm and the associated software and GUI interface for the MARS scanner.

Inventors: JL Healy, A Atharifard, ST Bell

- The algorithm quickly establishes the reliability of pixels and creates a mask to inhibit (turn off) unreliable pixels on the camera. The GUI allowed users to run the protocol and examine the mask created before saving it for scanner use. The basic framework of function and GUI were retained for the much expanded second generation masking software [1, 2]
- I contributed to all aspects of the pixel masking protocol: algorithm, data collection and analysis, software and GUI design
- This work is presented in Chapter 5

2) Developed and manufactured standardized material phantoms for use in automated material calibration of the MARS scanner.

- The phantoms consist of water based solutions of salts containing the elements of most interest in material decomposition. Concentrations range from easily detected to just below the current detection limit. Vials are arranged in a set geometric pattern to allow automation.
- I contributed to phantom design, choice of concentrations and was mainly responsible for manufacture
- This work is presented in Chapter 2 but is not discussed in great detail due to its elementary nature

Publications and Conference Proceedings

Published

3) RK Panta, CJ Bateman, J Healy, JL Mohr, N de Ruiter, AP Butler, NG Anderson, SP Gieseg. Simultaneous discrimination of multiple intrinsic bio-markers in excised atheroma with spectral molecular imaging. New Zealand Medical Journal 2013, 126(1375): 3.

- This work demonstrated the detection of lipid-, water- and calcium-like materials in phantoms and excised atherosclerotic plaques at photon energies relevant to human scanning (30 – 120 keV) using a Medipix3RX camera with GaAs sensor layer operating in Single Pixel Mode
- I contributed to all phases of the work: experimental design, data collection, data analysis, abstract preparation, slide layout for talk by Panta.
- This work is presented in Chapter 3

4) Raj Kumar Panta, Christopher Bateman, Joe Healy, Alex Chernoglazov, Steven P. Gieseg, Anthony Butler, Phil Butler, Nigel G Anderson. Implementing spectral molecular imaging (spectral CT) in soft tissue. Conference Proceeding of 34th National Conference of Association of Medical Physicist in India (AMPICON-2013, November 13-16, Kolkata, India), 90-91.

- This work demonstrated the detection of lipid-, water- and calcium-like materials in atherosclerotic plaque and lamb tissue samples using a MARS scanner with a Medipix3RX camera and GaAs or CdTe sensor layer. Atheroma data was collected using 30 – 120 keV photon range while lamb data was collected using the 10 to 50 keV range.
- I contributed to the all aspects of this work, experimental design, data collection, data analysis, abstract preparation, slide preparation.
- This work is presented in Chapter 3

5) R. Aamir, A. Chernoglazov, C.J. Bateman, A.P.H. Butler, P.H. Butler, N.G. Anderson, S.T. Bell, R.K. Panta, J.L. Healy, J.L. Mohr, K. Rajendran, M.F. Walsh, N. de Ruiter, S.P. Gieseg, T. Woodfield, P.F. Renaud, L. Brooke, S. Abdul-Majid, M. Clyne, R. Glendenning, P.J. Bones, M. Billinghurst, C. Bartneck, H. Mandalika, R. Grasset, N. Schleich, N. Scott, S.J. Nik, A. Opie, T. Janmale, D.N. Tang, D. Kim, R.M. Doesburg, R. Zainon, J.P. Ronaldson, N.J. Cook, D.J. Smithies, K. Hodge MARS Spectral Molecular Imaging of Lamb Tissue: Data Collection and Image Analysis. *Journal of Instrumentation* 9, no. 02 (February 17, 2014): P02005–P02005. doi:10.1088/1748-0221/9/02/P02005.

- This work demonstrates material decomposition of lipid-, water- and calcium-like materials in a lamb chop using photon energies from approximately 10 to 50 keV. The study was conducted for the purpose of making a quality data set available online which included raw, reconstructed and material reconstructed data
- I contributed to protocol development and manuscript preparation.
- This work is presented in Chapter 3

6) K. Rajendran, M.F. Walsh, N.J.A. de Ruiter, A.I. Chernoglazov, R.K. Panta, A.P.H. Butler, P.H. Butler, S.T. Bell, N.G. Anderson, T.B.F. Woodfield, S.J. Tredinnick, J.L. Healy, C.J. Bateman, R. Aamir, R.M.N. Doesburg, P.F. Renaud, S.P. Gieseg, D.J. Smithies, J.L. Mohr, V.B.H. Mandalika, A.M.T. Opie, N.J. Cook, J.P. Ronaldson, S.J. Nik, A. Atharifard, M. Clyne, P.J. Bones, C. Bartneck, R. Grasset, N. Schleich and M. Billinghurst. Reducing beam hardening effects and metal artefacts in spectral CT using Medipix3RX. 2014 JINST 9 P03015

- This work describes the reduced artefacts and increased contrast in narrower and/or higher energy bins for spectral reconstruction of scans of metal scaffolds. It discusses the implications for scanning protocols used to scan tissues with embedded metal. All raw and reconstructed data are available online
- I contributed to protocol development and manuscript editing. I was responsible for training the first author in use of the scanner
- This work is not discussed in this thesis as I was primarily involved as a sounding board for ideas and then in significant editing, but not in the work that was actually done, except to make phantoms.

7) RK Panta, R. Aamir, JL. Healy, K. Rajendran, NJA. de Ruiter, M. Moghiseh, APH. Butler, NG. Anderson, SP. Gieseg and PH. Butler. Multiple K-edges imaging with MARS-CT: proof of concept. The Annual Conference of the New Zealand Branch of the Australasian College of Physical Scientists and Engineers in Medicine (November 20-21, 2014, Christchurch, New Zealand), 63.

- This was a phantom study using human relevant photon energies (30 – 120 keV) to demonstrate simultaneous differentiation of four high atomic number materials (Gold, Gadolinium, Iodine, Calcium) based on spectral patterns revealing K-edge effects.
- This study used phantoms of my construction. I contributed to experimental design, data acquisition, data analysis and abstract editing

- This work is presented in Chapter 4

8) JL Healy, RK Panta, R Aamir, K Rajendran, NJA de Ruiter, CJ Bateman, AI Chernaglozov, MF Walsh, ST Bell, NG Anderson, APH Butler, PH Butler, SP Gieseg. Differentiating lipid, water and calcium-rich regions within atherosclerotic plaques using multi-energy CT. (2015) New Zealand Medical Journal 128(No. 1421):96.

- This work demonstrated spatial histologic correlation of lipid and calcification in an atherosclerotic plaque with the material decomposition of plaque scans at human relevant photon energies (30 – 120 keV). It is the first time a MARS scanner equipped with a Medipix3RX camera operating in Charge Summing Mode was confirmed to correctly identify traits of plaque vulnerable to rupture (a necrotic lipid core and spotty calcifications) while excluding low energy photons (below 30 keV) from the data set.
- I was primarily responsible for all aspects of this work: experimental design, protocol development, scanning samples, histologic processing, image correlation and abstract writing. See reference in Oral Presentations.
- This work is presented in Chapter 3

9) A Lindsay, J Healy, W Mills, JG Lewis, N Gill, N Draper, SP Gieseg. Impact-induced muscle damage contributes to oxidative stress in professional rugby union (2015) New Zealand Medical Journal 128(No. 1421):96.

- See contribution 12 for description

10) M. Moghiseh, R. Aamir, R.K. Panta, N. de Ruiter, C.J. Bateman, A. Chernoglazov, J.L. Healy, A.P.H. Butler, N.G. Anderson. Multi-energy spectral data of multiple high-Z materials – a phantom study. (2016) JSM Biomed Imaging Data Pap 3(1): 1007

- This work shows simultaneous material decomposition of gold, iodine, gadolinium, calcium, lipid and water in a phantom. The full raw, reconstructed and material reconstructed data sets are available online. The paper illustrates K-edge detection and the degree of material mis-identification as a function of concentration.
- This study used phantoms of my construction. I contributed to experimental design and manuscript preparation.
- This work is presented in Chapter 4

11) L. Vanden Broeke, A. Atharifard, B. P. Goulter, J. L. Healy, M. Ramyar, R. K. Panta, M. Anjomrouz, M. Shamshad, A. Largeau, K. Mueller, M. F. Walsh, R. Aamir, D. J. Smithies, R. Doesburg, K. Rajendran, N. J. A. de Ruiter, D. Knight, A. Chernoglazov, H. Mandalik, C. J. Bateman, S. T. Bell, A. P. H. Butler, and P. H. Butler. Oblique fluorescence in a MARS scanner with a CdTe-Medipix3RX. 2016 JINST 11 C12063

- This work describes a model for using off-axis X-ray fluorescence from monoatomic foils to perform per-pixel energy calibration of MARS scanners *in situ*. The model calculates the X-ray fluorescence intensity across the detectors field of view to enable positioning the camera in the ideal location for maximum fluorescence and minimum scatter from the primary beam. Initial experimental comparisons with the model are presented
- I participated in all aspects of this work including model development, experimental design, data collection and analysis.
- This work is presented in Chapter 6

12) A. Lindsay, J. Healy, W. Mills, J. Lewis , N. Gill, N. Draper, S. P. Gieseg. Impact-induced muscle damage and urinary pterins in professional rugby: 7,8-dihydroneopterin oxidation by myoglobin. Scandinavian Journal of Medicine & Science in Sports [2016, 26(3):329-337]

- This work examines the possible reactions of myoglobin and iron released from injured muscles with pterins produced in humans (some of which are thought to serve as anti-oxidants during oxidative stress). Products of reactions between myoglobin or iron and 7,8-dihydroneopterin were studied in vitro and then measured in urine samples from rugby players before and after games. Impact muscle injury had positive correlations with the reactants and reaction products.
- I participated in sample collection, data analysis and ran the enzyme-linked immunosorbent assay for myoglobin concentration in the urine samples. I also helped edit the manuscript.
- This work was not part of my proposal and is not discussed further in this thesis. It represents a contribution I was able to make to a fellow student's work because of the skills I developed working in Steven Gieseg's lab.

13) Gieseg SP, Healy JL, Prebble HM, Panta RK, Aamir R, de Ruiter NJA, Bateman CJ, Walsh MF, Bell ST, Anderson NG, Butler APH, Butler PH, White V, Roak J. Spectral Imaging of Unstable Atherosclerotic plaque by MARS-Scanning. Internal publication of the European Organization for Nuclear Research, CERN.

- This work is an overall review of progress in imaging of atherosclerotic plaque with MARS scanners. It includes material decomposition of intrinsic markers of vulnerable plaque in excised plaques in air and in a solution of gadolinium contrast agent. It also demonstrates the use of Calcium measurements from MARS scanning of plaque sections to correct metabolic measurements on live plaque sections for the amount of calcification present. We also demonstrated the ability of human macrophages to uptake gold nanoparticles in quantities sufficient to allow imaging with MARS which is a first step in developing spectral CT contrasts for imaging atherosclerosis.
- I was involved in all aspects of research presented in this overview: design and execution of experiments and scanner protocols, data analysis, image creation, training of Hannah Prebble in use of the MARS scanner, cell culture, and abstract preparation
- This work is covered in Chapters 3 and 4

14) Ali Atharifard, Joe L. Healy, Brian P. Goulter, Mohsen Ramyar, Lieza Vanden Broeke, Michael F. Walsh, Chikezie C. Onyema, Raj K. Panta, Raja Aamir, Derek J. Smithies, Robert Doesburg, Marzieh Anjomrouz, Muhammad Shamshad, Kishore Rajendran, Niels J. A. de Ruiter, David Knight, Alex Chernoglazov, Harish Mandalik, Stephen T. Bell, Christopher J. Bateman, Anthony P. H. Butler and Philip H. Butler. Per-pixel Energy Calibration of Photon Counting Detectors. 2017 JINST 12 C03085

- This work describes a technique for finding the energy offset of each counter on each pixel in the MARS camera from the global energy calibration of the counter thresholds. The technique will allow future MARS reconstruction software versions to correct for the variations in energy response between pixels that cannot be adjusted for using hardware settings. This will enable more accurate material identification using corrected spectral data.
- I was involved in concept development, experimental design, data acquisition and manuscript review.
- This work is covered in Chapter 6

15) Mahdieh Moghiseh, Aamir Raja, Joe Healy, Anthony Butler, Nigel Anderson. Identification and quantification of multiple high-Z materials by spectral CT. European Congress of Radiology, Vienna Austria, 2017.

- This work describes experiments that demonstrate the continued progression and improvement in simultaneous identification of three contrast agents (gadolinium, gold and iodine based) and bone (calcium) in a MARS scan. Phantoms and mice with each material concentrated in separate compartments were scanned and the material decomposition results examined visually and quantitatively.
- I produced the phantoms, was primarily responsible for experimental design and performed the mouse tail vein injections of gold and iodine contrast agents. I was involved in scanner protocol development and data analysis.
- This work is covered in Chapter 4

16) Muhammad Shamshad, Marzieh Anjomrouz, Derek J Smithies, Antoine Largeau, Gray Lu, Ali Atharifard, Lieza Vanden Broeke, Raja Aamir, Raj Kumar Panta, Michael F Walsh, Brian P Goulter, Kishore Rajendran, Srinidhi Bheesette, Joe L Healy, Niels de Ruiter, Alex Chernoglazov, Harish Mandalika, Robert Doesburg, Stephen T Bell, Christopher J Bateman, Anthony P Butler, and Philip H Butler. Semi-analytic off-axis X-ray source model. 2017 JINST 12 P10013

- This work describes a Monte Carlo-based model for estimating the relative and absolute intensity of X-rays of arbitrary energy bins produced by a broad spectrum X-ray source. The model is used in assessing X-ray source and camera function for quality assessment of MARS scanners. In the future, it will be a patented part of the commercial MARS imaging chain.
- I trained the primary author in use of the machine and was involved in manuscript development.
- This work is not covered in this thesis as I was heavily involved in manuscript development but not in the work described.

17) Raj Kumar Panta, Stephen T. Bell, Joe L. Healy, Raja Aamir Younis, Christopher J. Bateman, Niels J. A. de Ruiter, Mahdeih Moghiseh, Steven P. Gieseg, Anthony P. H. Butler and Nigel G. Anderson. Element-specific spectral imaging of multiple contrast agents: a phantom study. 2018 JINST 13 T02001

- This work describes a simple procedure for choosing threshold X-ray energy settings to optimize simultaneous detection of material k-edges using the MARS spectral scanner. The k-factor is introduced and used in combination with the relative X-ray intensity of each bin (which will correspond to the signal to noise ratio) to establish a rank for each protocol for each material. The summed ranks for each protocol are compared and the lowest total is deemed optimal. Results are shown that illustrate the effectiveness of the procedure.
- I helped develop the ranking system and experimental protocols. I helped in manuscript preparation and editing. I manufactured the phantoms.
- This work is covered in Chapter 4

18) Hannah Prebble, Sean Cross, Edward Marks, Joe Healy, Emily Searle, Raja Aamir, Nigel Anderson, Anthony Butler, Justin Roake, Barry Hock and Steven P. Gieseg. Induced macrophage

activation in live excised atherosclerotic plaque. Immunobiology https://doi.org/10.1016/j.imbio.2018.03.002

- This work describes the use of MARS material reconstruction to measure the quantity of calcium in live excised carotid endarterectomy samples. Plaques were manipulated to activate macrophages present in the tissue and then physiological responses and neopterin production was measured. Calcium measurement were assumed to represent material in the plaque that could not contribute to physiologic response and so each sections data were corrected based on the proportion of that section occupied by calcification.
- I was involved in protocol development, plaque visualization, the calcium measurements, and document editing
- This work is not presented in this thesis as my role was primarily advisory and in training the first author in use of the MARS visualization software for calcification measurements.

In Preparation

19) Identification of lipid and calcium-rich regions in excised carotid atherosclerotic plaque using spectral CT—intended for submission to European Radiology.

20) Material visualization of excised carotid plaque submerged in contrast agent solutions using spectral CT—intended for submission to European Radiology.

Posters

21) Healy JL, Gieseg SP, Prebble HM, Panta RK, Aamir R, de Ruiter NJA, Bateman CJ, Chernoglazov AI, Walsh MF, Bell ST, Anderson NG, Butler APH, Butler PH, White V, Roake J. Imaging of Cardiovascular disease by Spectral CT imaging. Joint Scientific Meetings of the Australian Atherosclerosis Society, the High Blood Pressure Research Council of Australia and the Australian Vascular Biology Society, Hobart, Australia 07-10/12/2016.

- This poster showed the ability to visualize an excised atherosclerotic immersed in a gadolinium contrast agent at 6 mg Gd/ml solution. Material decomposition was compared between scans of the same plaque in air and then in the Gd solution. The lipid and calcium component images were maintained in the Gd background. This is an indicator that intrinsic material information of interest will be attainable simultaneously in clinical contrast enhanced scans such as CT angiography.
- I was primarily responsible for all aspects of this study. I designed and carried out the experiments, helped in design of the scanner protocol, produced the phantom, analysed the data, performed the custom material decomposition protocol and produced the images used in the poster.
- This work is covered in Chapter 3

22) Healy JL, Panta RK, Aamir R, Rajendran K, de Ruiter NJA, Bateman CJ, Chernaglozov AI, Walsh MF, Bell ST, Anderson NG, Butler APH, Butler PH, Roake, J, Gieseg SP. Multienergy X-ray-CT Identification of Lipid Cores and Calcium Mineralisations in Excised Carotid Plaques. Annual Scientific Meetings of the Australian Atherosclerosis Society, Fremantle, Australia, 21-23/10/2015.

- This poster illustrates the work described in publication 8.

23) RK. Panta, R. Aamir, JL. Healy, K. Rajendran, NJA. de Ruiter, M. Moghiseh, ST. Bell, MF. Walsh, APH. Butler, NG. Anderson, SP. Gieseg and PH. Butler. Element specific spectral imaging using a MARS scanner. 'MedTech in Christchurch' workshop, University of Otago, Christchurch, New Zealand, 16/12/2014.

- This poster illustrated the simultaneous discrimination of multiple materials in a MARS scan using phantoms of gold, iodine, gadolinium, calcium, water and lipid.
- I was constructed the phantoms and was involved in protocol design, data collection and analysis.
- This material is covered in Chapter 4

24) Christopher J. Bateman, Raj Kumar Panta, Judy Mohr, Niels de Ruiter, R. Aamir, Anthony Butler, Philip Butler, Peter Renaud, Alexander Chernoglazov, Joe Healy, Nanette Schleich, Steven Gieseg, Stephen Bell, Karen Alt, Karlheinz Peter, Christoph Hagemeyer. Material discrimination with MARS. HOPE Meetings, Tokyo, Japan, 11-15/03/2014.

- This poster was an overview of the MARS system and the material reconstruction results available at that time.
- I provided the atheroma data sets and images used and helped edit the poster
- This work is contains material covered in Chapters 3 and 4

25) M.Moghiseh, R.Aamir, J.Healy, Dh.Kumar, K.Chitcholtan, P.Sykes, G.Dachs, R.K.Panta, N.J.de.Ruiter, A.I.Chernoglazov, C.J.Bateman, D.Knight, A.M.Henning S.T.Bell, A.Butler, P.Butler , N.Anderson. MARS Spectral Imaging of Nano-Particles As a New Modality For Detecting Cancer. Otago Spotlight Series: Cancer Research, University of Otago, Christchurch, New Zealand, 20/10/2015

- This work showed the detection and quantification of 2 nm gold nanoparticle in phantoms and a Lewis lung carcinoma tumour grown subcutaneously in a mouse. The abnormally large endothelial fenestra in the tumour neovasculature allows the build-up of gold nanoparticles specifically in the tumour. In the future, using MARS to identify gold nanoparticles in tumours may be useful in cancer diagnosis, assessment of quality of targeting of treatments and monitoring of cancer progression/regression.
- I was involved in experimental design, data collection, data processing and poster development. I performed the tail vein injections.
- This work is covered in Chapter 4

Oral Presentations

26) Healy JL. Breaking down arterial walls: testing the ability of spectral CT to image carotid atherosclerotic plaques. MARS mini-conference. Centre for Bioengineering, University of Otago, Christchurch, New Zealand, 22/05/2013.

- This talk described my research goals with respect to MARS imaging of intrinsic biomarkers of atherosclerosis
- This work is covered in Chapter 3

27) Healy JL. Spectral X-ray Tomography Imaging of Vulnerable Atherosclerotic Plaque. Annual Biology Conference, University of Canterbury, Christchurch, New Zealand, 17/10/2013.

- This talk covered the data presented in publication 3 above.

28) Healy JL, Atharifard A. Detector Characterisation for Improving Image Quality. MARS seminar, University of Canterbury, Christchurch, New Zealand, 16/10/2013.

- This talk presented the first results testing a pixel masking technique for inhibiting pixels on the MARS camera and described to MARS users how to use and make use of the masking protocol on the scanners.
- This work is covered in Chapter 5

29) Healy JL. Spectral X-ray Tomography Imaging of Vulnerable Atherosclerotic Plaque. Vascular Surgery Team meeting, Christchurch Hospital, New Zealand, 20/11/2013.

- This talk presented our findings to the surgeons who collaborate with us in obtaining carotid endarterectomy samples.

30) Healy JL, Panta RK. CT 10 and 11 Assessment. MARS IQ team meeting, University of Canterbury, Christchurch, New Zealand, 07/04/2014.

- This talk described our assessment and work in commissioning two MARS scanners
- I was involved in all aspects of this work as equal investigator
- This work is covered in Chapter 5

31) Healy JL. Material Characterisation of Atherosclerotic Lesions with Spectroscopic X-ray CT. Annual Biology Conference, University of Canterbury, Christchurch, New Zealand, 23/10/2015.

- This talk describes intrinsic imaging of atherosclerotic plaque
- I am responsible for all work presented
- The work is covered in Chapter 3

32) Healy JL. Differentiating lipid, water and calcium-rich regions within atherosclerotic plaques using multi-energy CT. Scientific Meetings of the Health Research Society of Canterbury, University of Otago, Christchurch, New Zealand, 22 & 29/11/2015.

- See description for previous citation

33) Healy JL. Interpreting the Calcium Component of Atheroma MD. MARS seminar, University of Canterbury, Christchurch, New Zealand, 06/07/2016.

- This work described strategies and problems with interpreting the calcium component of MARS MD of atherosclerotic plaque
- I was involved in all aspects of this work and am entirely responsible for the calcium assessment ideas
- This work is partially covered in Chapter 3

Awards

34) Best poster. MedTech in Christchurch Workshop poster competition. 16/12/2015. For Healy JL, Panta RK, Aamir R, Rajendran K, de Ruiter NJA, Bateman CJ, Chernoglazov AI, Walsh MF, Bell ST, Anderson NG, Butler APH, Butler PH, Roake, J, Gieseg SP. Multienergy X-ray-CT Identification of Lipid Cores and Calcium Mineralisations in Excised Carotid Plaques.

Student Supervision

35) Hayley Schoch. Radiation survival of cells within excised plaque during spectral-CT imaging. University of Canterbury Summer Research Scholarship, 2014.

- Hayley established that excised plaques scanned in MARS at room temperature and then cultured for 48 hours showed no difference in metabolic activity compared to unscanned plaques. This was the first step in establishing the feasibility of using MARS to characterise physiological or biochemical processes in live plaques. Hayley learned how to: run scans on the MARS scanner, create publication quality images using MARS Vision software, design replicated experiments, culture human derived cell lines, culture human derived tissues, and collect data with UV-vis spectrometers and HPLC machines.
- This work is covered in Chapter 3

36) Dylan Paterson. Small animal monitoring for live spectral imaging for non-invasive quantification of multiple biomarkers in different mouse models. University of Canterbury Summer Research Scholarship, 2015.

- Dylan tested small animal monitors for heart rate, breathing rate, blood oxygenation and temperature to be used inside the MARS scanner when live animal scanning begins. He learned proper handling technique and anaesthesia procedures for live mice while testing the equipment on anaesthetized wild type mice. He also demonstrated the importance of external warming sources to maintain mice body temperature at safe levels while under anaesthesia.
- This work is covered in Chapter 3

Chaired Conference Sessions

37) Annual Biology Conference, University of Canterbury, Christchurch, New Zealand, 23/10/2015.

38) Annual Biology Conference, University of Canterbury, Christchurch, New Zealand, 20/10/2016.

39) Chaired MARS Hardware and Robotics Team meetings for 6 months.

Editing

40) Abstracts for the Annual Biology Conference, University of Canterbury, Christchurch, New Zealand, 20/10/2016.

Funding

41) University of Canterbury PhD scholarship 12/1012

Collaborations

42) Baker IDI. Imaged excised carotid atherosclerotic plaques incubated in anti-platelet scfv-antibody-gold nanoparticle conjugates. Imaged mice with the same antiplatelet functionalized gold nanoparticles injected before and after carotid injury

1 Introduction

1.1 Objectives

This work was undertaken to explore and refine the use of spectral CT to locate, identify and quantify materials that indicate disease or injury in biological samples, with an emphasis on mimicking true human CT scans by filtering low energy photons (< ~30 keV) from the X-ray spectrum. The platform used for spectral CT is the MARS small animal scanner (MARS Bioimaging Ltd., Christchurch, New Zealand). As the MARS scanner is an emerging new technology, this work necessarily and intentionally includes developmental work on scanner and camera adjustment, calibration and assessment. The scanner's material output is termed a MARS image and is a quantitative material reconstruction of a scanned volume. Materials of interest were both intrinsic: lipid and calcium, and foreign: gold, gadolinium and iodine contrast agents.

Some diseases and their progression can be identified directly by characteristic intrinsic material distributions. Atherosclerosis is characterised by abnormal lipid accumulation and calcium hydroxyapatite deposition in the arterial wall. Excised atherosclerotic plaques were scanned to test the differentiation of high lipid and calcium regions from the soft tissue background.

Spectral X-ray CT is especially suited to contrast imaging because the K (or 1s) shell photoelectric effect occurs for high atomic number elements (arbitrarily, $Z > 50$ with a K-edge at 29.2 keV) in the human CT imaging photon energy range. X-ray attenuation decreases as the cube of increasing photon energy but rises sharply at atomic K-edges. This discontinuity can be detected with spectral CT and means that multiple contrast agents can be identified simultaneously.

Diseases are detectable by the use of introduced contrast agents. Anatomical, physiological, cellular and biochemical traits can be revealed with proper targeting of high atomic number contrasts. To test simultaneous differentiation of contrast agents and intrinsic materials, excised atheromas and whole mice were scanned. Atheromas were scanned in air and submerged in gadolinium contrast agent to test the fidelity of the lipid and calcium signals in contrast enhanced CT. To demonstrate cancer detection, mice with implanted subcutaneous Lewis Lung carcinoma tumours were scanned after injection of 15 nm gold nanoparticles (AuNPs). The particles do not pass through the fenestrae (pores) of healthy vascular endothelium, but will accumulate in tumours due to abnormally large endothelial fenestrae in the neovasculature that supplies the tumour. A feasibility study for simultaneous identification of three contrasts (gold, gadolinium and iodine) and three intrinsic materials (lipid, water and calcium) in a biological sample was undertaken using healthy wild-type mice.

The MARS scanner uses energy discriminating, photon counting technology to simultaneously obtain multiple X-ray attenuation datasets in one scan. The X-ray source used in CT imaging produces a broad spectrum with photon energies that range from the lowest allowed by filtration, 10 keV or more, to a maximum around 140 keV. Conventional CT measures only total energy attenuation across the spectrum but the MARS scanner can measure photon count attenuation within up to eight adjacent energy ranges.

Every element has a different spectral X-ray attenuation profile. Adjacent volumes with different elemental makeup can have the same total energy attenuation across the spectrum and are thus indistinguishable in conventional CT. However, the pattern of attenuation across multiple energy ranges will differ which allows spectral X-ray detection to identify materials.

As with any measurement, the quality of the raw data collected (energy sensitive photon count attenuation) determines the quality of the conclusions (material identification and quantification). Any adjustment or technique that improves the accuracy of the photon counting or the energy resolution will also improve material identification. This thesis includes work on assessing and masking the MARS camera pixel matrix to eliminate pixels that produce faulty data. Also, standard commissioning tests are described along with a new quality assessment technique for the quantitative material images or material decomposition (MD). Finally, two techniques for producing pixel specific energy calibrations are described which could replace the chip-wide energy calibration currently in use.

The ability to identify materials and measure concentrations within a volume using a noninvasive measurement has potential value in many fields, including geology, security, food processing and medicine. Both clinical practice and clinical research will benefit from material reconstructions which add a new dataset to the diagnostic toolbox.

1.2 Overview

The thesis chapters are organized into three sections. Chapters 1 and 2 provide context and background on both the machine and the biological models used for scanning. Chapters 3 and 4 describe imaging experiments. Phantoms and biological samples were scanned to test material identification under various conditions. The ultimate goal was to refine protocols to optimize material identification using photon energies relevant to human scanning (30 to 120 keV for this thesis). This is in anticipation of the first MARS human-sized scanner which is undergoing commissioning now. Chapters 5 and 6 describe technical work on the machine, data assessment and pixel specific energy calibration. The thesis concludes with a chapter summarizing the results and describing future work in spectral CT inspired by the outcomes of this thesis.

The background (Chapter 2) is designed to be read unless the reader is very familiar with a particular topic. Each section describes an important field related to the thesis and in some cases includes comments specific to the work. The sections are intended to act as broad

introductions that provide the context for much of the research described. In so doing, it prevents repetition in the introductions and discussions of each chapter and chapter section.

Chapters 3 and 4, intrinsic and contrast enhanced imaging of biological samples with MARS, respectively, include a range of studies carried out with several different collaborators, but all part of the MARS clinical teams goals to explore the potential of spectral CT and material reconstructions to aid disease diagnosis, assessment, progression/regression and treatment. The introductions and discussions of some chapter sections are more detailed than others and address the MARS scanner's potential and deficiencies at greater length. These longer chapter sections are the studies that were most interesting to me and/or involved my greatest input but the discussions are, largely, applicable to other studies in the same chapter which are kept shorter to prevent repetition.

Each chapter follows the same structure: **Introduction**, **Study 1**, **Study 2** etc., and **Conclusion**. Within each **Study** section, the format is also the same. An **Introduction** divided into subsections: **Aim**, **Significance**, **Publication** and **Contribution**, is followed by **Methods**, **Results** and **Discussion**.

Finally, a note on the terminology used for the material decomposition. Each voxel of the material reconstruction has a concentration for water and one of the other materials used in the calibration phantom, e.g. gold or lipid. While publications from MARS team members typically refer to lipid-like or gold-like voxels to make clear the uncertainty in knowing the actual content, this thesis will simply say lipid or gold and assume the reader is aware that unknown materials have been mapped onto a limited set of calibration materials.

1.3 Chapter topics

Chapter 1 introduces the thesis goals, reviews the general organization and describes each chapter's content.

Chapter 2 provides background information to familiarize readers with broad topics of importance in the thesis. Principles and techniques of computed tomography and spectral CT are described. The MARS scanner, camera and software are explained so that readers understand the collection and processing of raw photon count data and its transformation into attenuation and material reconstructions. Important biological topics are described, in particular, atherosclerosis and cancer.

Chapter 3 investigates the use of MARS spectral CT to measure lipid and calcium content within biological samples, with an ultimate goal of identifying lipid cores and spotty calcification in atherosclerotic plaque. Studies progress from macroscopic views of a lamb chop using low energy photons that maximize soft tissue information to an in depth analysis of the lipid and calcium content of atherosclerotic plaque scanned with higher energy photons similar to those used in actual human CT scanning.

Chapter 4 demonstrates the potential of MARS spectral CT in measuring contrast agent distributions and intrinsic material arrangements in biological samples, simultaneously. Phantom studies are used to investigate and refine energy threshold placement to optimize K-edge detection. Single contrasts are used to show cancer detection by accumulation of contrast within a tumour in a mouse model, atheroma detection even when the plaque is submerged in contrast solution and macrophage detection resulting from active uptake of contrast. Three contrast agents, bone and lipid are all differentiated simultaneously in a mouse.

Chapter 5 describes efforts to assess the quality of the imaging chain and indicate areas that could be improved. The highlight is preliminary work on determining pixel quality in the MARS camera and the subsequent masking software to eliminate bad pixels. The commissioning effort of two MARS small animal scanners is briefly described. A new data graphing technique comparing attenuation values to material concentrations is described that provides a strong measure of the impact of the partial volume effect on material decomposition.

Chapter 6 presents two strategies for developing a per pixel energy calibration to replace the whole camera calibration currently used. First, a method for calculating an energy offset for each pixel using threshold scans similar to the current global calibration technique is described. Second, a direct per pixel energy calibration is demonstrated using K_α fluorescence from molybdenum and lead.

Chapter 7 concludes the thesis. An outline of the significant results of each chapter is presented. Future research possibilities are described along with a vision of the potential of spectral CT in clinical imaging.

2 Background

2.1 MARS scanners

The MARS small sample scanner (Figure 2.1) is a spectroscopic X-ray CT (see Section 2.4) unit. A lead protected vault houses a micro-focus X-ray source opposite a MARS X-ray camera on a rotating gantry with horizontal axis of rotation. The sample holder moves the scan subject horizontally through the X-ray beam near the centre of rotation. Objects up to ~100 mm in diameter may be scanned. The source to object distance (SOD), object to detector distance (ODD) and source to detector distance (SDD) are adjustable and the camera can be moved tangential to the rotation in order to cover larger diameter objects by repeating the scan for multiple vertical camera positions and stitching the overlapping images together.

Figure 2.1: The MARS small animal scanner from outside and in.

The MARS scanner is built around the Medipix chip family of photon counting, energy resolving detectors developed at the European Organization for Nuclear Research (CERN) (see Section 2.2). Currently, cameras have between 1 and 5 chips arranged vertically or tiled as a four chip square. A detailed description of the camera is found in the PhD work of Robert Doesburg [3].

The eight counters per pixel have adjustable lower energy threshold settings. A threshold sets a lower limit for photon energy detection. In theory, all photons attenuated within a pixel that have an energy above the threshold are counted, photons attenuated but below the threshold are ignored. By setting the eight thresholds to different values, simultaneous spectroscopic X-ray attenuation data can be acquired. In reality, sensor and application specific integrated circuit (ASIC) imperfections and the variability of quantum physical

interactions create noise in the data [4]. Correcting for this noise is accomplished through Medipix chip adjustment and MARS data processing software.

MARS vision software consists of reconstruction [5], material decomposition (MD) [6] (see Section 2.6) and visualization units [7]. A reconstruction is created for each energy bin using a proprietary iterative algebraic reconstruction technique which will be referred to as mART. The MD uses the energy bin reconstructions to analyse the spectral behaviour of each voxel and determine the material content and concentration. MARS vision software provides a platform for visualizing and making measurements of the attenuation and/or the material reconstructions. Data can be viewed in grayscale or colour, with customisable transfer functions based on attenuation or concentration, using 2-D and 3-D projections. A virtual 3-D space can be visualized through integration with a zSpace® (zSpace, Inc., Sunnyvale, CA, USA) platform.

The X-ray sources are by source-ray, inc., Ronkonkona, New York, USA. In this thesis, sources have a peak kilovoltage (kVp) of 80 kVp with a ~33 µm focal spot or 120 kVp with a ~50 µm focal spot. They are broad spectrum sources with a tungsten target. The operating voltage and current are adjustable, allowing control over the spectrum content and flux.

2.2 Medipix chip and photon counting

The Medipix chip is an Application-specific Integrated Circuit (ASIC) computer chip originally developed for high energy particle detection by an international collaboration based at CERN [8–11]. Bonded to a semiconductor sensor it forms a hybrid pixel detector for counting single event particle interactions. It converts electron/hole pair clouds created by photon interaction in the sensor into a current that is proportional to the energy of the photon. Thus, it can count individual photon interactions and assess if the energy is above an arbitrary threshold. It has been adapted for use in medical X-ray imaging [12].

The chip contains electronics for processing the magnitude of electrical signals (i.e. a current or voltage) on a timescale of ~25 ns or less [13]. It is divided into 55 µm pixels each with two counters that tally individual electric signals over an arbitrary current magnitude, called the energy threshold.

For the MARS X-ray cameras used in this thesis, a semiconductor sensor layer is bump bonded to the Medipix chip on a 110 µm pattern which combines four 55 µm ASIC pixels to make one pixel with 8 independent energy sensitive photon counters [11]. At 14.08 mm X 14.08 mm, the sensor has 128 pixels per row and column for 16,384 pixels total.

Because the sensor layer is not pixelated the charge clouds created by photon attenuation may diffuse across multiple pixels in the ASIC leading to multiple counts for one event, all with incorrect energy assessment. This is called charge sharing. Medipix has charge summing and arbitration electronics for assessing which pixel the photon interaction actually occurred in and assigning the total energy deposited to a single count in that pixel (see Section 2.4).

While each counter on each pixel processes the event amplitude signal independently, the pixels are not truly independent. The energy threshold value for each counter is set globally using a digital-to-analog converter (DAC). So, counter one has the same threshold DAC value for all pixels, counter two has the same DAC value for all pixels and so on for all eight counters (see Section 2.3).

2.3 Equalization, energy calibration and material calibration

The MARS camera requires pixel equalization and energy calibration to maximize its spectroscopic function [14, 15]. Equalization minimizes threshold dispersion in the energy calibration. Threshold dispersion means that at a specific global DAC value for a given counter, each pixel will actually be set to a slightly different energy threshold. Equalization involves adjusting each pixel so that just above the noise floor (which is presumed to be at the same energy for all pixels) corresponds to the same DAC value in the global energy threshold settings for each counter. The adjustment is imperfect and a certain level of threshold dispersion remains (see Chapter 6) [4, 11].

After equalization, the global energy threshold DAC values must be calibrated to actual photon energy values (see Chapter 6). Currently for MARS cameras, energy calibration is done with the X-ray kVp technique [16]. Very simply, the X-ray tube is set to a series of voltages and at each the camera is run through a range of DAC thresholds. The DAC value at which half of the pixels are counting and half not is established as the global DAC value corresponding to the highest energy photons present in the current beam (which is equal in keV to the kVp of the X-ray tube). A calibration line is then fit for each counter through the series of values for each voltage setting.

Material calibration is required for the MD (see 2.6). The materials that are identified by the MD are arbitrary; therefore, the user establishes the materials of interest and must make a phantom for each to use in calibration. The material phantom with a range of concentrations for each material is scanned using the same protocol to be used for sample scanning and the attenuation is measured for each material concentration. This is converted to a mass attenuation coefficient for each material at each energy bin. This series of spectral signatures is used as the calibration. The sample scans are then compared to these signals to determine content.

2.4 Charge Summing Mode and Single Pixel Mode

Charge sharing gives rise to noise due to incorrect counting and energy measurement. To correct for charge sharing, Medipix3RX introduced functional charge summing mode (CSM) [11, 17]. The chip can be operated with CSM on or off. When off, it is operating in single pixel mode (SPM) [18].

In SPM, each pixel operates independently of the surrounding pixels. The charge collected from the sensor layer in each pixel is compared to the thresholds for each counter and tallied or not regardless of the source of the signal. This means that a single photon interaction can give rise to a signal in multiple pixels and its energy is divided between them. The signal may be counted as too many photons each with a lower energy or the photon may not be counted at all if the energy is dispersed in such a way that no thresholds are exceeded, even though the total energy would have been counted by some counters if deposited in a single pixel. In MARS cameras, SPM allows the use of eight energy bins.

To correct for charge sharing, CSM was introduced. See 2013 JINST 8 C02016 by Ballabriga et al. for a good description of the chip architecture and function [11]. In Charge Summing Mode (CSM), the current generated simultaneously in adjacent pixels is summed and assigned to the pixel with the largest portion as a single photon where it is counted by any counters with thresholds set below the measured total. In theory, this eliminates the counting and energy noise from charge sharing.

To enable CSM, the eight counters on each pixel are used in different ways, which means that eight equivalent energy bins are no longer available. One counter, the arbitration counter, is used for assigning the summed signal to the correct pixel and three are left operating in SPM, meaning they do not contain the charge sharing correction. Thus, four counters remain for CSM.

For all SPM scans in this thesis, eight counters were used for reconstruction and MD. For all CSM scans in this thesis, four counters were used for reconstruction and MD.

2.5 Spectral CT and K-edge imaging

Spectral CT which was suggested by Hounsfield in his original paper on CT [19] is simply the combination of X-ray spectroscopy (measuring the different attenuation of X-rays of different energy) with computed tomography reconstruction of the interior appearance of an object based on X-ray projections from multiple angles. By measuring the attenuation of each voxel at two or more different energy ranges, conclusions may be made about the material composition and concentration of each voxel that are independent of our prior knowledge of what materials we expect to see. It adds another source of information for scientists and clinicians, beyond the spatial images of broad-spectrum CT.

Every element has a unique X-ray attenuation profile across the range of X-ray energies (Figure 2.2). X-ray spectroscopy can identify specific elements or combinations of elements in complex samples based on these attenuation differences [20, 21]. Dual energy CT and MARS CT bring a rough X-ray spectroscopy to medical imaging and allow material identification and quantification [12, 19, 22, 23].

Attenuation across energies is not a continuous function for elements. As X-ray photon energy increases attenuation decreases in general, but, as the binding energy of each

successive electron shell is reached and electrons from that shell may be ejected from the atom by the photoelectric effect [24], a sharp rise in attenuation occurs. The K-edge is the discontinuity in attenuation due to the binding energy of the 1s orbital and is of particular interest in clinical X-ray technologies because the K-edge of many elements occurs in the range of photon energies used in imaging. For example, if we assume the typical human CT scan has photon energies from ~30 keV to ~120 keV, then every element from antimony (Z = 51) to uranium (Z = 92) has a K-edge in the clinical imaging range. This means that high Z elements have particularly strong attenuation in CT imaging and are potentially valuable as X-ray contrast agents (see Section 2.7).

The combination of spectral CT and high Z contrasts with K-edges in the imaging spectrum opens up the possibility of identifying multiple materials in the same scan. Figure 2.2 shows how materials with exactly the same concentration could be distinguished based on their differing spectral attenuation. Carbon (as a surrogate for soft tissue), calcium (surrogate for bone) and iodine would have to be distinguished based on the curvature of the graph, but gadolinium, hafnium and gold would all show distinct rises in attenuation from one lower energy bin to the next higher energy bin. This K-edge effect simplifies the detection of more materials in a simple four energy bin spectrometer like the MARS scanner [6].

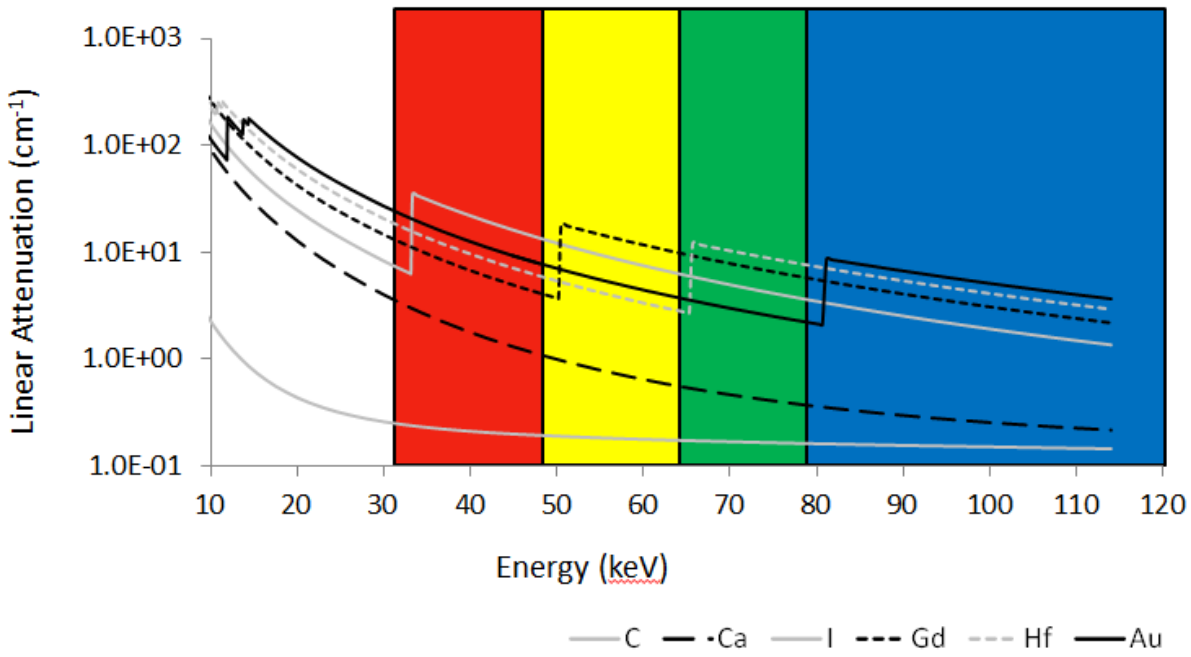

Figure 2.2: Linear attenuation for equal densities of six elements. The colour regions show how thresholds might be set in a spectral CT system to detect the K-edges of three different contrasts made with gadolinium, hafnium and gold. In MARS, each colour represents a subtracted energy bin, meaning that, for two adjacent threshold settings, like 32 and 48 in the graph, the counts from the 48 to 120 keV bin are subtracted from the counts for the 32 to 120 keV bin to give counts from 32 to 48 keV.

2.6 Material Decomposition

For spectral CT, material decomposition is using attenuation patterns across energies to estimate the material make-up of each voxel, giving a material reconstruction [6, 25–28]. With proper calibration, the concentration of each material may also be estimated.

The material image produced in MARS is a quantitative reconstruction of the concentration of materials in each voxel. In the MD, each voxel's spectroscopic linear attenuation pattern is compared to the calibration materials using a constrained linear least squares algorithm [6]. Each voxel is assumed to consist of two materials, water and one other calibration material that contributes most strongly to the spectral response. Any voxel consisting of only lipid and water is termed a soft tissue (ST) voxel; while voxels with other calibration materials are deemed high Z (for atomic number). All ST voxels are reported in concentrations of lipid and water (pure lipid and pure water must be included in all material calibration phantoms). All high Z voxels are reported in concentrations of water and one of the high Z materials from the calibration phantom (can be an element, compound or complex mixture).

For the intrinsic material scans in this thesis, the only high Z material is calcium. For the contrast based scans, high Z materials may be calcium, iodine, gadolinium or gold. The material data are reported as concentrations in mg/ml.

For intrinsic materials with appreciable concentrations, there are no K-edges within the range of photon energies used in MARS scanners. The arbitration counter, which always has the lowest threshold, is usually set around 10 keV. Figure 2.3 shows the difficulty of this problem, especially for scans using energies relevant in human clinical scanning (considered 30 to 120 keV for this thesis). In this case, the useful energies for lipid/water differentiation basically lie between 30 and 50 keV.

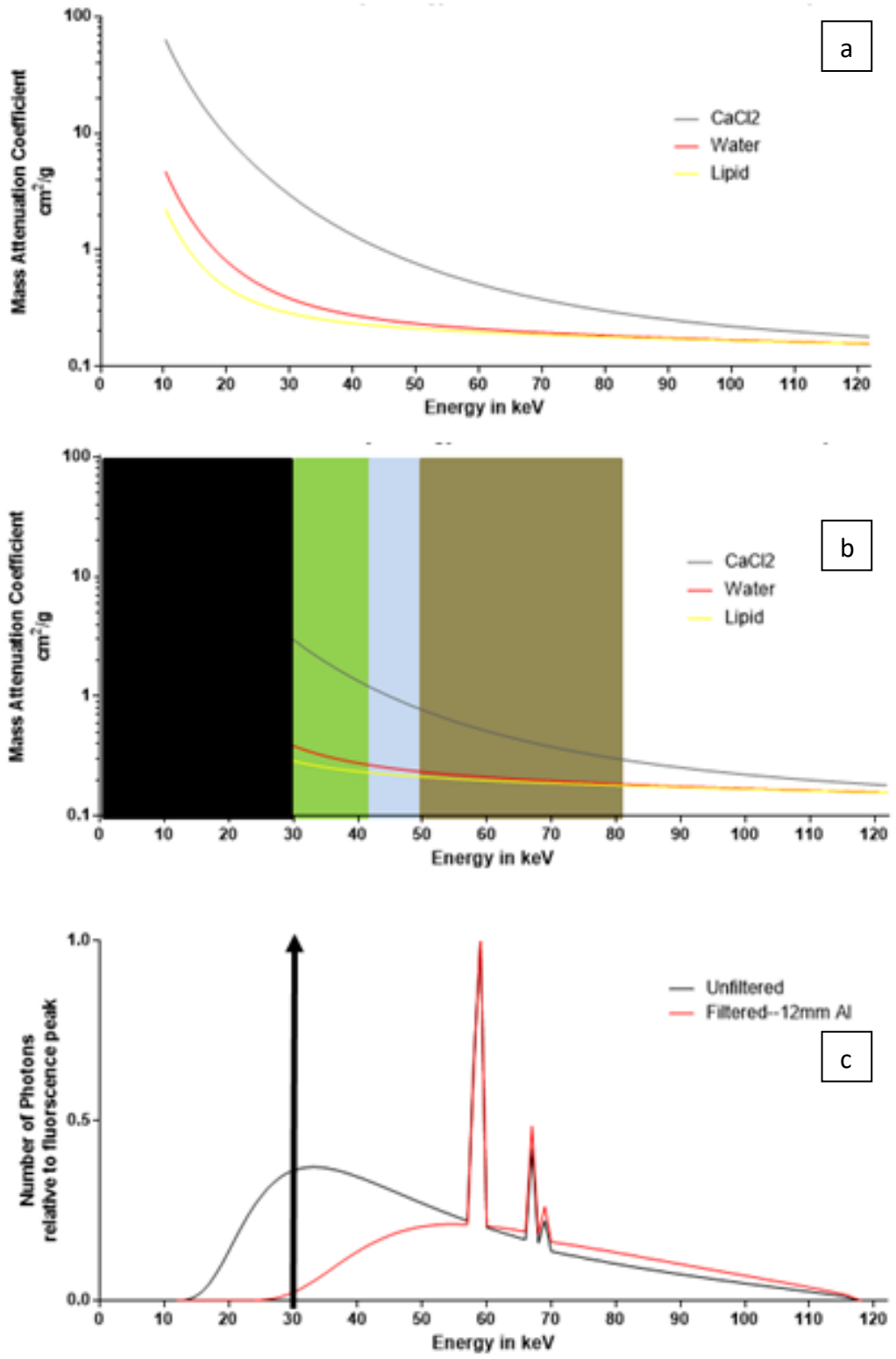

Figure 2.3: The problem of MD for intrinsic materials. Panel (a) shows the mass attenuation of $CaCl_2$, water and lipid across all energies. (b) shows how the area with the greatest differences in magnitude and slope are eliminated by the filtration of the spectrum, shown in (c) with and without 12 mm of added aluminium. The coloured regions in (b) represent the energy bins used for plaque 108 (see Section 3.4).

2.7 Contrast Agents

Contrast agents are materials added to the sample to increase the difference in signal between a region of interest and the surrounding area. They can act by creating hypo- or hyper intensity in the region of interest (ROI) or the surrounding area. In CT, an increase in attenuation using high Z materials is the norm.

Iodine and barium are the most common elements used in X-ray contrast agents. Many other elements are being investigated for future use, especially gold nanoparticles because of gold's high attenuation and the ease of manipulating its chemical surface to make biologically compatible contrasts [29–32].

All contrasts are targeted to some degree. For example, we inject iodine contrast agents intravascularly to see the vasculature, looking for stenosis, haemorrhage, tumours etc. or we drink barium sulphate to show abnormalities in the digestive tract. As chemistry and biochemistry advance, the ability to target specific structures, cells, proteins, diseases and so on with contrast agents and/or treatments is growing. The degree of specificity ranges from targeting by size for tumours with abnormally large endothelial fenestrae (see 2.9) [33] to targeting a specific conformation of a single glycoprotein using iron oxide or gold conjugated to anti-body fragments [34, 35] (see Table 2.1 for a small sample). See some recent reviews for a more thorough examination of targeting contrasts for medical imaging and research [29–32, 36–38].

Table 2.1: Targeted contrast agents

Contrast Material	Target	Targeting Method	Reference
Gold nanorod	Cancer tumour	EPR effect (size)	[33]
Gold nanoparticle	Vasculature/kidneys	Size and biocompatibility	[39]
Iron oxide	Activated platelets	anti-glycoprotein IIb/IIIa anti-body	[34]
Gold core HDL	Atherosclerotic plaque	Biocompatibility/plaque lipid physiology	[40]
Bismuth sulphide nanoparticle	Cancer tumour	LyP-1 tumour targeting peptide	[41]
Gold nanoparticle	Cancer tumour	Anti-GD2 antibody	[42]

2.8 Atherosclerosis

Cardiovascular disease (CVD) causes one fourth of all deaths worldwide [43] and includes coronary heart disease, carotid artery disease, peripheral artery disease and chronic kidney disease. One of the primary causes of CVD is atherosclerosis, which is the formation of lesions in the artery walls called plaques. The thromboses that cause heart attack and stroke often result from the rupture of atherosclerotic plaques. Abnormal physiology and biochemistry leads to abnormal structure and composition of the artery wall [44–50]. In particular, the retention of lipid-rich particles such as low density lipoprotein (LDL) in the intimal layer of artery walls is associated with the initiation and progression of plaques [51]. The vulnerable plaque most often associated with rupture is characterised by a lipid-rich necrotic core, spotty calcifications, a thin fibrous cap, positive remodelling of the artery wall, intra-plaque haemorrhage, neovascularisation, and inflammation associated with immune cells such as macrophages [52–58]. Detecting these abnormalities noninvasively before they cause severe clinical events is a focus of atherosclerosis research [59–68].

In this thesis, the focus will be on MD of the spatial arrangement of high lipid regions (corresponding to the necrotic lipid core) and calcifications. The earliest stages of lesion development involve the accumulation of lipids in the form of low density lipoprotein (LDL). As plaques progress, a necrotic lipid core forms within the intima and its size correlates with the risk for rupture. Calcifications are hypothesized to stabilize plaques or promote rupture depending on their size and location. Large, continuous calcifications that wrap around most of the circular arc of a vessel are thought to promote plaque stability while spotty calcifications are often proposed to promote rupture [69–78]

2.9 Cancer

Cancer caused 15.2% of all deaths worldwide in 2010 [43]. Cancer is the uncontrolled proliferation of native cells that can spread to neighbouring tissues, sometimes metastasising to varied locations throughout the body [79, 80]. It can form solid tumours or exist as circulating cells.

Cancers are frequently imaged with CT. In unenhanced CT imaging, cancers may be viewed by abnormal hypodensity [81], hyperdensity [82] or isodensity [83]. Calcifications are common in certain cancers and can be imaged [82, 84]. Solid tumours frequently have traits that can be exploited for contrast enhanced imaging, both in the research and clinical environment, including neovascularization with abnormally large endothelial fenestrae [85, 86] and protein expression that is not normally found in healthy, mature tissues [41, 42, 87–90].

In this thesis, the leaky nature of cancerous neovascular endothelium is exploited to investigate the use of gold nanoparticles for cancer tumour detection and monitoring.

Calcifications are not specifically investigated in a cancer model, but the microcalcification work on atheromas is applicable.

2.10 Phantoms

Phantoms are artificial objects designed to test or calibrate some aspect of the scanner set-up or performance. For material calibration, phantoms are tubes of known concentration of the materials of choice for the MD. At least two concentrations for each material are necessary, but since the MD assumes that all voxels contain water and one other material, one of the concentrations is always zero (i.e. 100% water) for all materials. The MD requires that water and lipid are present in all material calibration phantoms. For all scans in this work, lipid is canola oil and water is Milli-Q® ultrapure water (Merck KGaA, Darmstadt, Germany). Other materials are water solutions or resin suspensions.

All phantoms in this thesis were produced by me except the commercial hydroxyapatite phantoms (QRM GmbH, Moehrendorf, Germany).

2.11 Foil fluorescence

When a 1s electron is ejected from an atom by photoelectric attenuation (see Section 2.4), an electron from a higher energy shell may release energy as an X-ray fluorescence (XRF) photon and fill that lower energy state. The electron can come from any shell but the most common transition is from the second, or L, shell to first, or K, shell [91]. This transition is termed K_α fluorescence. It typically has two photon energies present, representing the transition from the 2s and 2p orbitals. The most likely transition is 2p to 1s, or $K_{\alpha 1}$, which has a slightly higher energy than the 2s to 1s, or $K_{\alpha 2}$, transition. The K_α fluorescence signal from various monoatomic foils can be used for energy calibration of the MARS camera (see Chapter 6), and for this purpose, the two K_α energies are considered to be a single, nearly mono-energetic signal at the $K_{\alpha 1}$energy.

Not every K-edge photon attenuation results in a photoelectric X-ray emission. The proportion of K-edge attenuation events that result in photoelectric X-ray emission is the fluorescence yield, ω [92]. The fluorescence yield of just K_α photons is labelled, $\omega_{K\alpha}$. Only K_α and $\omega_{K\alpha}$ are used in this thesis (Chapter 6).

3 Intrinsic Material Differentiation with MARS

3.1 Introduction

Medical imaging is basically the search for anomalous views that reveal injury or disease. When viewing intrinsic tissues using unenhanced CT (i.e. no contrast agents), anomaly consists of abnormal spatial arrangements or abnormal X-ray density in relation to known anatomy. The latter includes hyperdense abnormalities like calcifications in breast cancers and atherosclerosis (see 2.8 and 2.9) or uric acid crystals in gout [93] and hypodense abnormalities like lipid cores in atherosclerosis, fatty liver diseases [94] or glioblastomas of the brain [95]. The MARS team is investigating unenhanced imaging in all of these diseases and I have contributed to each, but my focus has been atherosclerosis.

Atherosclerosis provides an excellent model for testing intrinsic MD. Plaques take many forms, but the most common structures associated with plaque rupture and subsequent adverse ischaemic events are a plaque with a lipid-rich necrotic core, spotty calcifications, a thin fibrous cap, positive remodelling of the artery wall, intra-plaque haemorrhage, neovascularisation, and inflammation associated with immune cells such as macrophages. While all of these may be identifiable with MARS images, this preliminary work concentrates on the basic separation of lipid-rich and calcium-rich regions from background tissue, termed water-rich. The lipid core and the range of sizes of calcification from sub-voxel to many cubic millimetres offer a good test of the material separation and quantification capabilities of MARS.

Each of the energy bins in MARS systems is a separate view with different information based on the varying interactions of materials and X-rays of different energies. While these multiple views of the same region can be analysed by eye, analytic software like MARS MD assess the attenuation profile of each voxel across the energy bins and convert it to material concentrations (see Chapter 2). This provides researchers and clinicians with an analysis of spatial arrangements of materials in a sample independent of their own interpretations of a set of attenuation reconstructions.

The three scans described in this chapter were designed to test the limits of the MARS system in identifying lipid-rich and calcium-rich regions under gradually more difficult conditions. First a scan of lamb meat is described that tests intrinsic MD at low kVp where soft tissue contrast is superior. Second, an eight energy bin SPM scan of an excised, partially dehydrated carotid atherosclerotic plaque was done in the hope of maximizing the lipid contrast at the human energy range (~30 to 120 keV). The third scan uses fully hydrated tissue and demonstrates lipid core and spotty calcium identification in the MD using CSM and, again, photons from 30 to 120 keV.

Table 3.1: Scan parameters for the samples in this chapter

Sample	Lamb meat	Plaque 72	Plaque 108	Plaque 90
Detector	Medipix3RX	Medipix 3.1	Medipix3RX	Medipix 3.1
Sensor	2 mm CdTe	600 µm GaAs	2 mm CdTe	600 µm GaAs
Camera mode	CSM	SPM	CSM	SPM
Bias voltage (V)	-440	-300	-700	-300
Pixel matrix	128 x 128	128 x 128	128 x 128	128 x 128
Pixel pitch (µm)	110	110	110	110
SDD (mm)	131.8	190	185	219
SOD (mm)	83.8	120	130	155
Magnification	1.57	1.58	1.42	1.41
Projections/rotation	720	720	980	720
Flatfields	500	720	720	720
Tube Voltage (kV)	50	120	118	120
Tube Current (µA)	120	300	30	300
Exposure (ms)	40	350	200	350
Filtration (mm) Al or brass	1.8 Al intrinsic	11.8 Al (1.8 intrinsic + 10 added)	13.8 Al (1.8 intrinsic + 12 added)	11.8 Al (1.8 intrinsic + 10 added)
Thresholds (keV)	15, 20, 25, 30	30, 35, 40, 45, 50, 60, 70, 80	30, 42, 49, 81	30, 35, 40, 45, 50, 60, 70, 80
Focal spot size (µm)	~33	~50	~50	~50
Reconstruction algorithm	MARS-algebraic reconstruction technique (mART)	mART	mART	mART
Voxel size (µm)	100	41	90	41

The chapter ends with a brief review of two summer student projects I supervised to begin preparing for live cell, tissue and animal scanning. The scan of plaque 90 was part of Hayley Schoch's summer project.

3.2 Lamb tissue: demonstrating CSM and MD at low kVp

Introduction

Aim

Charge summing mode was usable in the MARS system for the first time in 2014. We scanned a sample of lamb meat at a low kVp with three goals. First, demonstrate the functionality of CSM in producing a quality reconstruction and MD of biological material. Second, using optimal parameters for ST imaging, test MD separation of lipid, water and calcium components on a macroscopic scale relevant to current expectations of CT spatial resolution. Third, provide open access to a full MARS dataset from raw projections through the processing chain and finally the attenuation and material reconstructions.

Significance

Charge sharing is a significant source of noise and blurring in small pixel hybrid detectors [18]. This work demonstrates the functionality of CSM as a correction for charge sharing and is one of the first datasets made available utilizing CSM.

Soft tissue contrast is one of the weaknesses of CT imaging because the attenuation differences are so small between different tissue types [96]. As MARS scanners develop on a technological and algorithmic progression, it is important to demonstrate the accompanying progression in the quality of attenuation and MD reconstructions.

Publication

This work appears in the Journal of Instrumentation [97].

Contribution

As a member of the MARS clinical team, I was part of all discussions concerning scan protocols and priorities for demonstrating MARS functionality on a clinical level. I contributed to manuscript development and editing.

Methods

A fresh lamb chop with conspicuous meat, fat and bone (Figure 3.1) was scanned at 50 kVp (see Table 3.1 for full protocol). The material calibration phantom consisted of 0.2 µl PCR tubes (inside diameter of ~5 mm) filled with lipid, water and 320 mg $CaCl_2$/ml solution in water.

As with all MARS datasets, the raw data are flatfield corrected by dividing each projection by an open beam projection that is averaged over a large number of frames. This partially corrects for fixed pattern noise due to pixel variability. Ring filtration is then applied to the projections. The unstitched frames are input to mART for reconstruction followed by MD. The energy bins were not subtracted for the reconstruction, meaning the first energy bin is counts for all photons from 15 to 50 keV, the second bin is from 20 to 50 keV and so on.

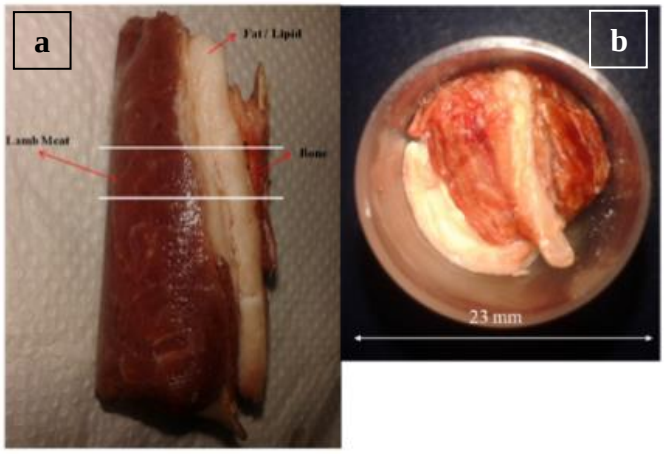

Figure 3.1: Lamb meat sample. a) White lines show the region scanned. b) Tissue in the sample holder for scanning. Used with permission [97]

Results

Figure 3.2 illustrates the MD results. All raw, processed and reconstructed data for the lamb meat scan and the calibration phantom scan are available at http://hdl.handle.net/10092/8531.

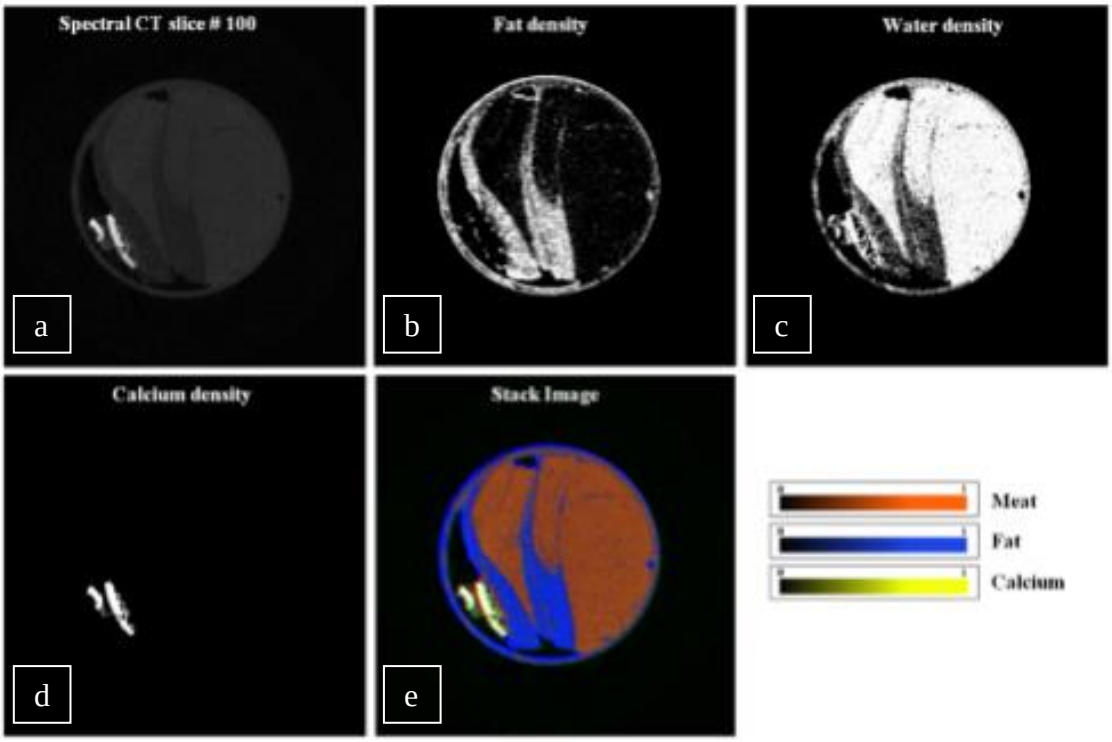

Figure 3.2: Transverse slice 100 which includes bone, fat and meat. Panel a) Attenuation based reconstruction of the 15 keV energy bin, b) fat component, c) water component, d) calcium component and e) a composite material image. The MD components in b, c and d are displayed as binary data, no concentration scaling is done. The colourscale for (e) is normalized relative to the calibration concentrations. Used with permission [97]

Discussion

The results clearly show the quality of the MD on a macroscopic scale. Lipid-rich and calcium-rich regions can be discerned at a voxel resolution of 100 μm. The attenuation reconstruction in Figure. 3.2 (a) and the composite MD in (e) are nearly identical to the eye. The large fat strips on the left and near the centre show very high lipid concentration while the meaty portions have some small marbling of fat, as might be expected. The spatial clarity and MD quality demonstrate the functionality of CSM.

This study demonstrates the potential for MARS material images in distinguishing intrinsic material arrangements with implications for medical imaging. Dual-energy CT can also provide material reconstruction [98] but requires two data acquisitions as opposed to the simultaneous four bin acquisition in this study. This is important in a range of clinical work done by the MARS team in atherosclerosis, fatty liver disease, breast imaging, and contrast enhanced imaging with functional nanoparticles. Beyond medical uses, quality ST imaging is also of interest to the meat industry for machine assisted butchering.

No effort was made to confirm the results with histology or material quantification as the macroscopic results match expectations of the familiar appearance of lamb chops.

3.3 Plaque 72: demonstrating intrinsic material MD in spectroscopic mode

Introduction

Aim

The scan was part of efforts to demonstrate successful MD at energies relevant to human scanning using eight SPM energy bins and gallium arsenide (GaAs) as the sensor layer for the detector [99]. Zainon et al. [100] have previously shown successful MD of lipid, water and calcium components of excised carotid plaque at low kVp with a silicon sensor layer. This study sought to mimic a true human scan by operating at 120 kVp and adding 10 mm of aluminium filtration to produce an x-ray spectrum simulating the filtration and attenuation of a human head and neck scan. Using the atherosclerotic plaque model for lipid rich and calcium rich regions on more microscopic scales than the meat sample in Section 3.2, we scanned a series of excised carotid plaques looking for a clear lipid core and microcalcifications. We then sought to confirm the MD with histological level examination of regions of interest that contained lipid and calcification.

Significance

By operating at 120 kVp and filtering the source this work demonstrated the feasibility of producing material reconstructions of vulnerable plaque that allow identification of a lipid core and spotty calcifications in a true clinical setting. This study demonstrates the use of

eight simultaneously acquired energy bins to produce high spatial resolution material images of vulnerable atherosclerotic plaque. It also demonstrates the value of GaAs as a sensor layer for medical imaging systems.

Publication

This work is featured in the New Zealand Medical Journal [101]

Contribution

I was involved in all aspects of this work as a co-investigator with Raj Panta. I am solely responsible for all sectioning, staining, photography and microscopy.

Methods

Human carotid endarterectomy samples are used for scanning and obtained under human ethics approval reference CTY/01/04/036/AM05. Carotid endarterectomy samples are obtained from surgical theatre and placed in a -80C freezer for future use. The samples are then thawed at room temperature in a moist environment and scanned in air inside a polypropylene tube.

Scanning was carried out using eight energy bins in SPM with a 600 µm GaAs sensor layer bump bonded to the Medipix3.1 chip. See Table 3.1 for protocol details. The phantom contained lipid, water, and $CaCl_2$ (100, 140 and 200 mg $CaCl_2$/ml solution).

At this time, the MARS scanners were fairly unstable in operation both mechanically and with respect to camera stability. Furthermore, developers were making frequent changes to software at many points in the imaging chain, from machine control to camera adjustment to reconstruction and MD algorithms, so it was difficult to know what changes lead to improvements in results. In order to maximize chances of a quality scan, we simply decided to repeat the same scan over and over in a single day, examining the results of one scan while the next was running. Also, in order to maximize the chances of successful material separation of high lipid regions, the plaque was scanned repeatedly at room temperature in a ventilated tube to allow the tissue to dry slowly. After a series of previous scans proved unsuccessful in producing a quality MD of high lipid regions (typically, noise was simply too prevalent or little to no lipid was reported despite the near certainty that lipid is present), it was hoped that allowing the tissue to dry might enhance the contrast between lipid and other regions that might contract as water was lost (becoming more dense). This approach was, admittedly, highly unscientific and we made no attempt to monitor changes in wet weight.

After the MD results showed a potential lipid core and spotty calcification we sectioned the plaque by hand using a scalpel blade at positions of interest. The sections were photographed and then stained for neutral lipids using oil-red O. Sections were submerged in a saturated solution of oil-red O in 60% isopropanol and water for 15 minutes with agitation on a rocker table. Sections were then rinsed three times in 60% isopropanol for five minutes each rinse. Sections were photographed again in white light; then photographed in an epifluorescence microscope (Leica M205 FA Stereomicroscope). The plaques were excited with green light

at 546 nm and emission was a 590 nm long pass filter. Calcifications autofluoresce (hydroxyapatite does not, but associated compounds, including cholesterol result in intense fluorescence) and oil-red O fluoresces weakly red under green excitation [102, 103] so fluorescence microscopy highlights the two MD materials of interest (lipids and calcifications).

Results

The fifth scan of plaque 72 was chosen for use in this study because of the quality of the MD. Scans 1-4 were deemed too noisy, with many high lipid voxels in the air regions surrounding the plaque and within the lumen (note the clean air regions in the MD in Figure 3.3 (d) despite the noise in the air in the reconstruction, Figure 3.3 (c)). Review of the MD showed a likely lipid core in the ICA and spotty, variably shaped calcifications around the bifurcation. Figure 3.3 shows the correlation between histology and reconstructions.

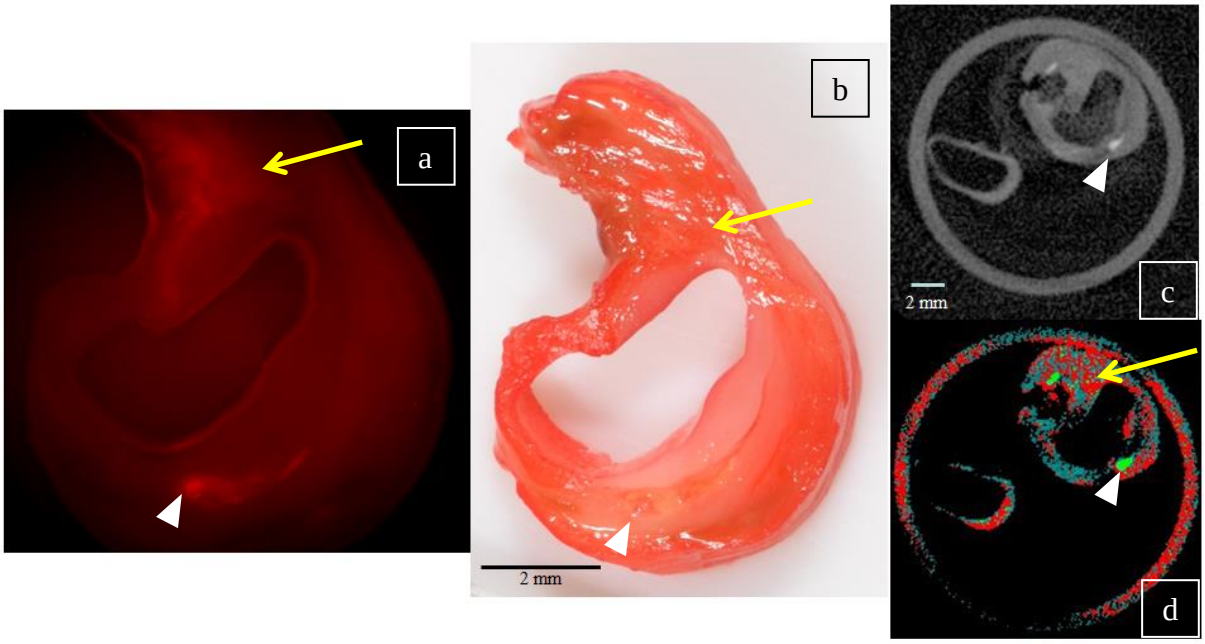

Figure 3.3: Lipid and calcium comparison of MD and histology. Yellow arrows point to a triangular lipid region that is apparent in the red fluorescence image (a) the oil-red O stained photo (b) and the MD (d), but is not obvious in the reconstruction of the first energy bin (c). White arrowheads point to a teardrop shaped calcification that is clear in all four images. The scale bar in (b) applies roughly to (a) as well and the same for the scale bar in (c) applying for (d).

Spotty calcifications are apparent in both the attenuation and MD reconstructions (Figure 3.4)

Figure 3.4: Spotty calcification at high resolution. Panels a and b show the high spatial resolution of calcifications in both the MD (a) and attenuation based reconstruction (b). Panel c is a MARS 3D image showing the spotty calcifications (white) in and around the bifurcation. The ECA is pointing down and in the back of the image. For the MD in (a): green = lipid-like, blue = water-like and red = calcium-like. The scale bar in (a) also applies to (b) but not (c). Used with permission [104]

Discussion

This study shows the feasibility of identifying lipid cores and spotty calcifications in carotid plaques using photon energies that are relevant to human CT scanning. MD of intrinsic biological materials using SPM with eight energy bins is possible. GaAs is a reasonable sensor material for higher energy CT scans though its low absorption efficiency at higher energies (~40% at 80 keV for 1mm GaAs) indicates patient doses could be higher than if more efficient materials were used such as CdTe[105–107].

The quality of the calcium component of the MD (Figure 3.4) indicated that more detailed analyses of microcalcifications were worthwhile in future carotid scanning. Figure 3.4 (a) clearly identifies calcifications that are smaller than 500 μm. Spotty calcification is

considered an indicator of vulnerable plaque and microcalcifications are a possible source of weakness in the thin fibrous cap that may be the site of cap failure [70, 75, 76, 108].

The excellent contrast of calcifications in the epifluorescence images and the ease of identifying oil-red O staining compared to white light illumination are apparent comparing Figure 3.3 (a) and (b). Thus, the technique was refined for use in future plaque imaging (see Section 3.4).

3.4 Plaque 108: MD using CSM and the human energy range

Introduction

Aim

The goal of this work was to demonstrate the potential of MARS spectral CT in CSM with a CdTe sensor to identify lipid and calcium components of plaques using a spectrum relevant to live human imaging. The plaque was scanned fully hydrated (unlike plaque 72 in Section 3.3) to better represent a true scan and better test the improved scanner which featured greater machine stability, improved pixel/camera stability, functional pixel masking on the camera and in raw data pre-processing (see Chapter 5), superior reconstruction and MD software and, importantly, functional CSM. Using the MARS spectral CT scanner, with 4 energy bins in CSM, we scanned excised carotid atherosclerotic plaques using the X-ray tube at ~120kVp. To mimic a true human head and neck scan, we added filtration, eliminating almost all photons below 30keV.

The work also presents a more detailed analysis of the quantitative aspects of the MD. The concentrations that might be expected inside a plaque were researched and thresholds for viewing the MD data were established based on this search.

This work also used histological examination to corroborate the presence of a lipid core and microcalcifications shown in the MD.

Significance

This work demonstrates the potential to find two hallmarks of vulnerable plaque, the lipid-rich necrotic core and spotty calcifications, in true human scans using future MARS human scanners. The value of CdTe as a sensor layer is also confirmed.

Publication

Parts of this work are published in the New Zealand Medical Journal [109]. A manuscript is in preparation for submission to European Radiology. Parts of this work have been shown in posters and talks at national and international conferences.

Contribution

I performed all of the work in this section.

Methods

Human carotid endarterectomy samples are used for scanning and obtained under human ethics approval reference CTY/01/04/036/AM05. Plaque 108 was received from a carotid endarterectomy and frozen in a -80C freezer. It was then thawed to room temperature and scanned in a tube with moist cotton to maintain 100 % humidity and prevent water loss. Scanning was done in CSM with a Medipix3RX camera with 2 mm CdTe sensor. The calibration phantom contained water, lipid and 50, 150 and 250 mg $CaCl_2$/ml solutions in polypropylene tubes with an inside diameter of ~3 mm. Filtration of 12 mm Al was added to produce a spectrum with essentially no photons below 30 keV (0.5%) according to a SpekCalc produced data set [110–112]. The mean photon energy was 65.5 keV. See Table 3.1 for the full protocol.

The phantom was included with the sample (see Fig 3.5) to provide a simultaneous material calibration under exactly the same scan conditions. This was done as a precaution due to some evidence of drift between scans from other MARS developers.

For the first time, thresholds were set specifically to maximize water/lipid differentiation. As stated in Section 2.6, most of the spectral information valuable in soft tissue MD is below 50 keV. Thresholds used for the CSM counters were 30, 42, 49 and 81 keV. For simplicity, energy bins will be referred to by the lowest photon energy of the subtracted bins. For graphing, however, the mean bin energy calculated from SpekCalc will be used, 37.5 keV (30 to 42 keV bin), 45.6 keV(42 to 49 keV bin), 63.0 keV (49 to 81 keV bin) and 94.1 keV(81 to 118 keV bin). Thresholds were set to maximize information below 50 keV; however, due to the threshold dispersion of the energy calibration (about 8 keV at 59.5 keV, which limits the narrowness of adjacent threshold settings) [16] and our interest in maintaining continuity with future studies using gold nanoparticles, the highest threshold was set to 81 keV (the k-edge of gold). The remaining thresholds were chosen to give roughly equal, open beam photon counts in the first two bins.

For assessing the traits of vulnerable plaque using the MD, the following criteria were established for lipid and calcium concentration assessments. No attempt was made to quantify the components by other techniques. The MD output values for both lipid and calcium concentrations vary from zero and up, but the practical significance of, for example, a $CaCl_2$ concentration of 5 mg/ml or a lipid content of 50 mg/ml is not clear. For perspective, an isotonic solution of pure $CaCl_2$ would have a concentration of about 11.4 mg $CaCl_2$/ml. With respect to lipid, the mass percent of lipid in human cells has been measured at about 12 %, so roughly 120 mg/ml. In this light, calcium and lipid data were examined both with all values included and excluding voxels valued lower than thresholds of 12 mg $CaCl_2$/ml and 120 mg lipid/ml. In composite material images, the calcium component is usually displayed as a replacement volume. This means that the Ca colour scheme is not mixed with the accompanying water value in red. This allows visualisation of voxels with low Ca concentrations which would otherwise be washed out by the associated high water concentration. For all colour MD images in this section, lipid is represented by yellow, water by red and calcium by grey.

MD results were compared to histology by visual analysis of selected cross sections of the plaque. Sections were cut with a scalpel roughly perpendicular to the axis of scan rotation at five points of interest and then examined with and without staining for neutral lipids. After sectioning, all cut surfaces were photographed unstained, then stained for neutral lipids with oil-red O and photographed again under white light. The staining procedure was the same as that in Section 3.3 except the rinse procedure was expanded. The plaque was rinsed for two hours total in 60% isopropanol with changes in the rinse solution at 5 minutes, 10 minutes, 15 minutes and 1 hour.

Stained sections were also photographed using an epifluorescence stereomicroscope (Leica M205 FA stereomicroscope) with a GFP plus filter (460 to 500 nm excitation, 510 nm long pass emission). The fluorescence images highlight calcifications and neutral lipids. Calcifications fluoresce intensely yellow due to incorporated or associated lipids such as unesterified cholesterol [103, 113] or ceroid [114]. Neutral lipids fluoresce red due to oil-red O staining (yellow/green autofluorescence of lipids such as cholesterol are quenched by the stain)[102, 115]. Other materials such as elastin and collagen also autofluoresce yellow/green, but the larger calcifications are obvious by shape and intensity. Photographs of the unstained sections were examined and labelled by a pathologist with experience in atherosclerosis but without access to the scan results. The plaque sections were correlated by eye with sections of the CT reconstruction and MD based on plaque outline and visible calcifications.

The MD was also compared to the 30 keV energy bin to assess agreement of the MD with traditional radiologic analyses of CT data. The attenuation data for the four energy bins were converted to bin specific CT numbers using spectral Hounsfield units within each bin according to the procedure proposed by Hurrell et al. [116]. A customized transfer function for the spectral Hounsfield unit (HU) data of the 30 keV bin, which should have the best tissue contrast, was used to examine the spatial agreement between attenuation and the material reconstruction. It should be noted that the values of spectral HU for spectral energy bins cannot be directly compared to those expected for integrating CT datasets.

Results

Spectral calibration data for material discrimination are shown in Figure 3.5 along with a transverse slice reconstruction from each energy bin displayed in HU with a constant window level. Attenuation is proportional to $CaCl_2$ concentration in each energy bin (Figure 3.5 b) and, relative to water, as energy increases, the attenuation of $CaCl_2$ decreases while the attenuation of lipid increases (Figure 3.5 c). This trend can be seen in the grey scale images (Figure 3.5 a) of the phantom tubes. The combination of the linear relationship of attenuation to density within a material in Figure 3.5 (b) and the different shapes for different materials of the trend lines in Figure 3.5 (c) allow the discrimination and quantification of materials in MARS images.

The MD algorithm is conservative in favour of soft tissue over calcium. To illustrate, sampling 36,000 voxels in each calibration phantom of the material reconstruction, 7% of Ca

50 voxels are misidentified as soft tissue, while 0.1% of water phantom voxels are misidentified as calcified.

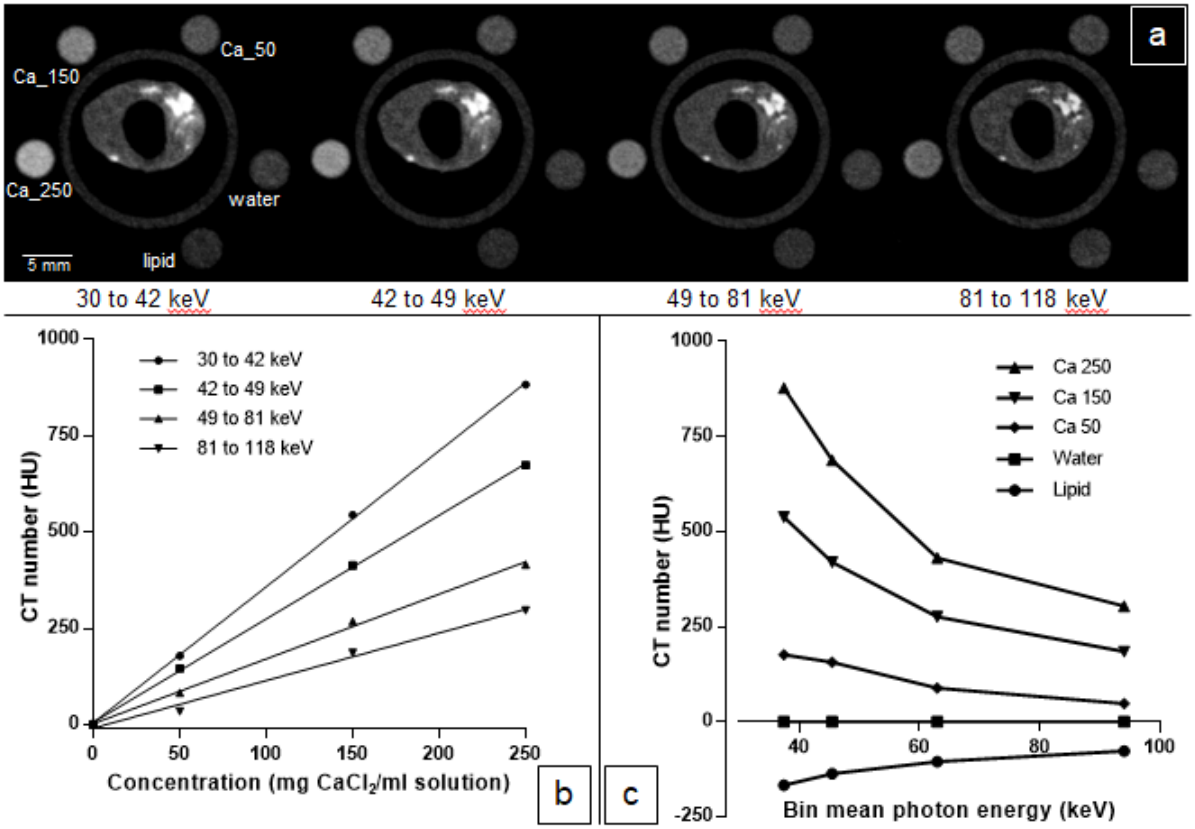

Figure 3.5: Calibration results: (**a**) CT attenuation grey scale images of each energy bin for a single transverse slice displayed in Hounsfield Units. Window level is -700 to 3300 HU. Voxel size is (90 µm)^3. (**b**) Attenuation in HU vs concentration of $CaCl_2$ for each energy bin. (**c**) Attenuation in HU vs energy for the calibration phantoms. Ca 50, Ca 150 and Ca 250 are 50, 150 and 250 mg $CaCl_2$/ml solution, respectively. Points are plotted on the energy axis at the estimated mean photon energy of the bin.

A longitudinal section of the reconstruction and MD through the carotid bifurcation is displayed in Figure 3.6. The MD displays two distinct regions of plaque surrounding the bifurcation of the common carotid artery (CCA): a heavily calcified region in the internal carotid artery (ICA) which extends down into the ICA side of the CCA and a proposed lipid core with spotty calcifications on the external carotid artery (ECA) side of the CCA. The presence of a lipid core with spotty calcifications made this the plaque of choice for further histological examination.

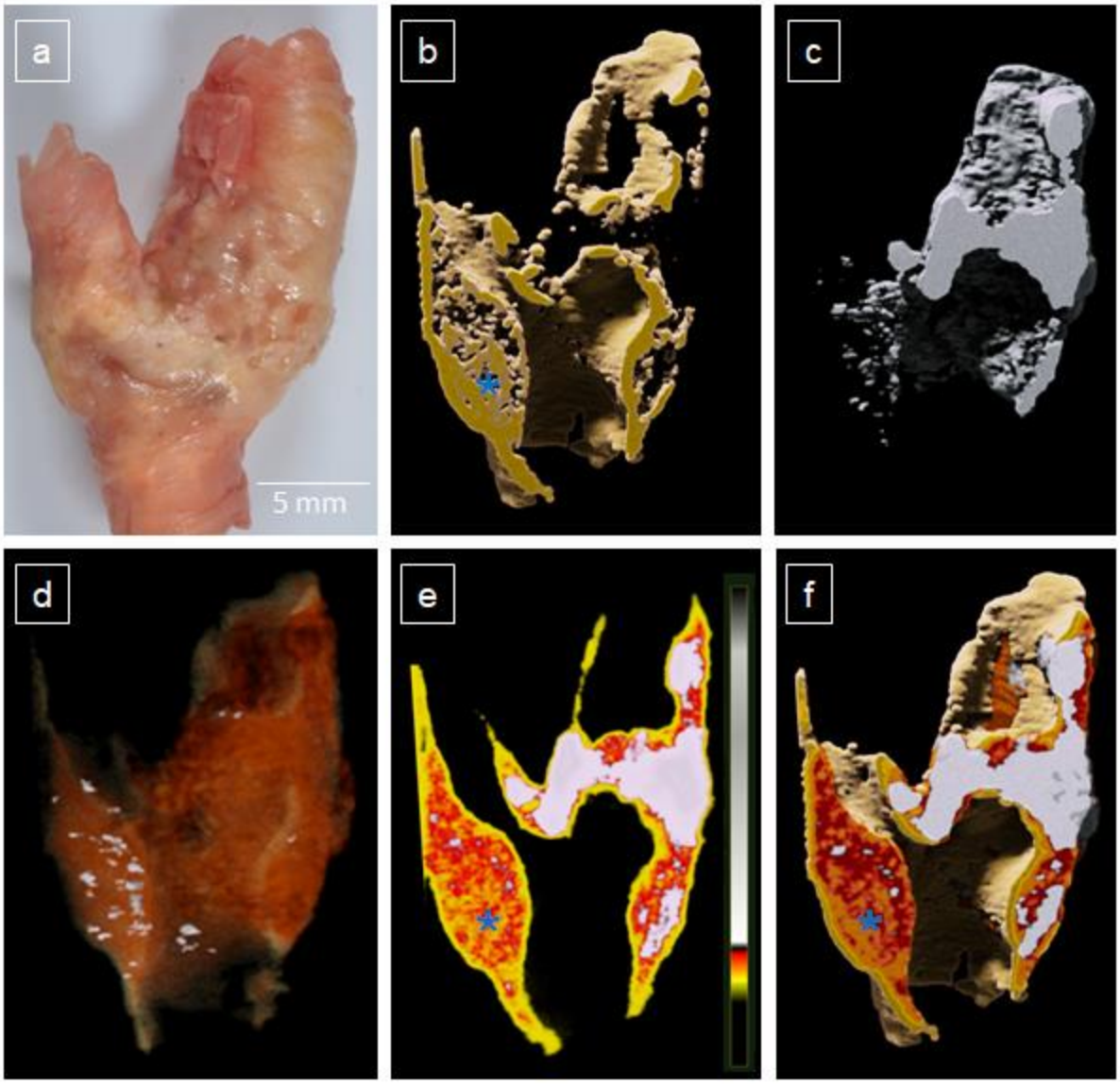

Figure 3.6: Various views showing the lipid core (blue ∗) and spotty calcification of the same longitudinal slice through the bifurcation of the plaque pictured in (**a)**. MARS images consist of material volumes. The lipid component in yellow (**b**) and calcium component in grey (**c**) are combined with the water component in red (not pictured) to form a composite (**d** and **f**). In **d**, the lipid and water opacity are reduced and the large calcification that dominates the right side of the image has been removed to highlight spotty calcium in the proposed lipid core. The MARS material composite in (**f)**, based on spectral data, corresponds well with the raw attenuation data from the 30 keV energy bin shown in (**e)**. In (f), calcium is shown as a replacement volume (see Methods).

Figure 3.7 visually compares a hand cut transverse slice (about 3 mm upstream from the internal beginning of the bifurcation) through the proposed lipid core to the corresponding slices of the reconstruction (30 keV bin) and the composite MD. Due to repeated rinsing, some material has been washed away between the unstained photo and the oil-red O stained fluorescence image (Figure 3 b and a, respectively) which is especially apparent in the region highlighted by Figure 3.8.

The intense green region of fluorescence in the proposed lipid core is magnified in Figure 3.8. Among other possibilities, the small granules visible within the tissue may be cholesterol crystals, ceroid deposits or HA crystals associated with cholesterol or ceroid (see Discussion). The lack of oil-red O staining may be due to a combination of material washing away during rinses, high concentrations of non-neutral lipids such as free cholesterol and cholesterol crystals or a lack of lipids altogether.

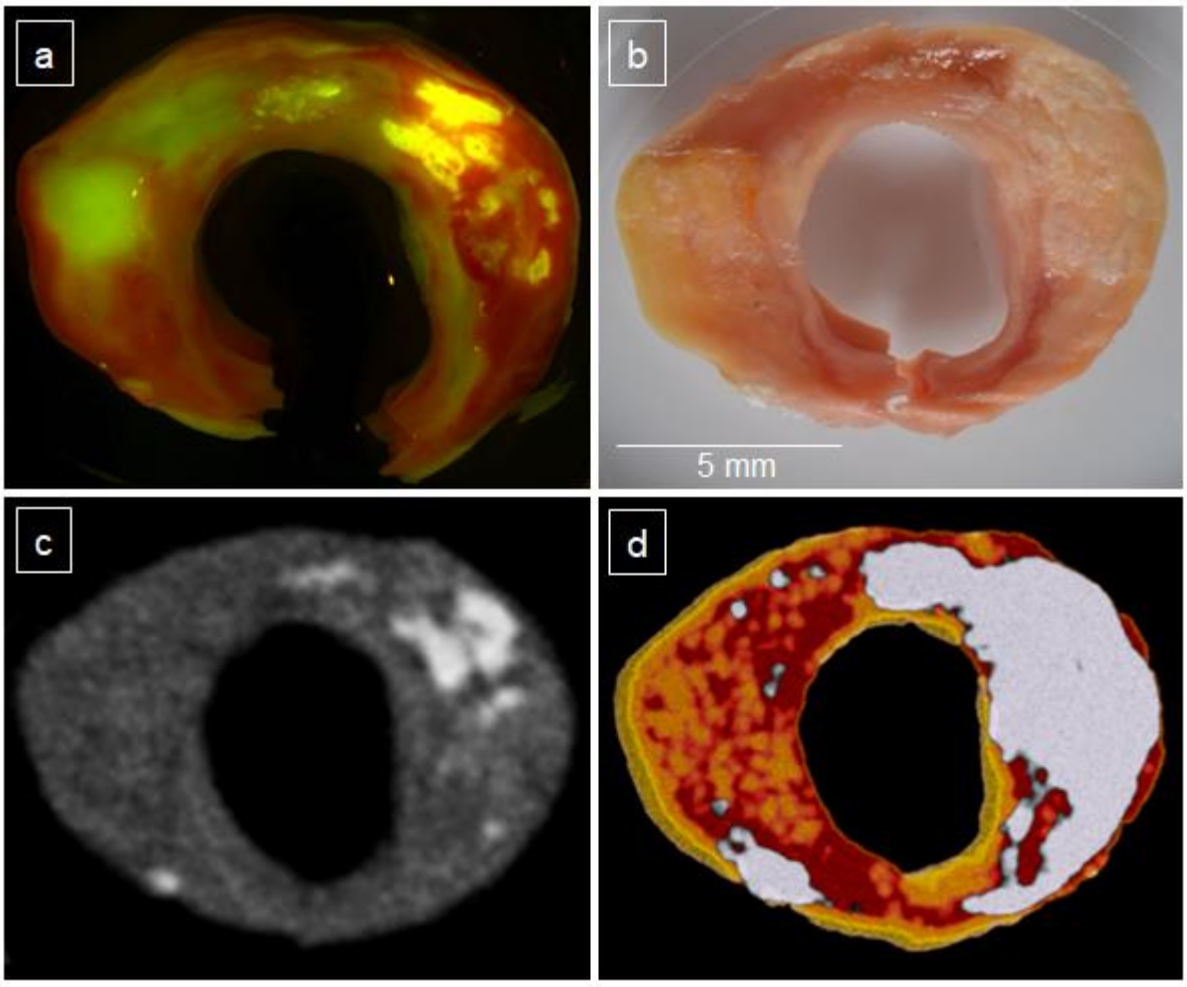

Figure 3.7: Lipid and calcium correspondence between histology and reconstruction. Histology(**a** and **b**) and attenuation (**c**) or material (**d**) reconstructions of a transverse slice located about 3 mm upstream from the internal beginning of the bifurcation. Panel (**a)** is an epifluorescence microscope image after oil-red O staining. Excitation 460 to 500 nm, emission 510 nm long pass filter. Panel (**b)** is a photo of the unstained section. Panel (**c)** is an attenuation based reconstruction of the 30 keV energy bin. Panel (**d)** is a MARS material image. The distinctly shaped lipid core without large calcifications on the left side of the plaque is clear in both the unstained photo (the yellow to brown region in (**a**) and the MARS material image (**d**), while it is present but less distinct in the attenuation image (**c**). In the MARS material image (**d**), materials are presented as follows: the calcium component has a lower threshold of 12 mg $CaCl_2$ /ml, and it is shown as a replacement volume (see Methods). The lipid component has a lower threshold of 120 mg lipid/ml.

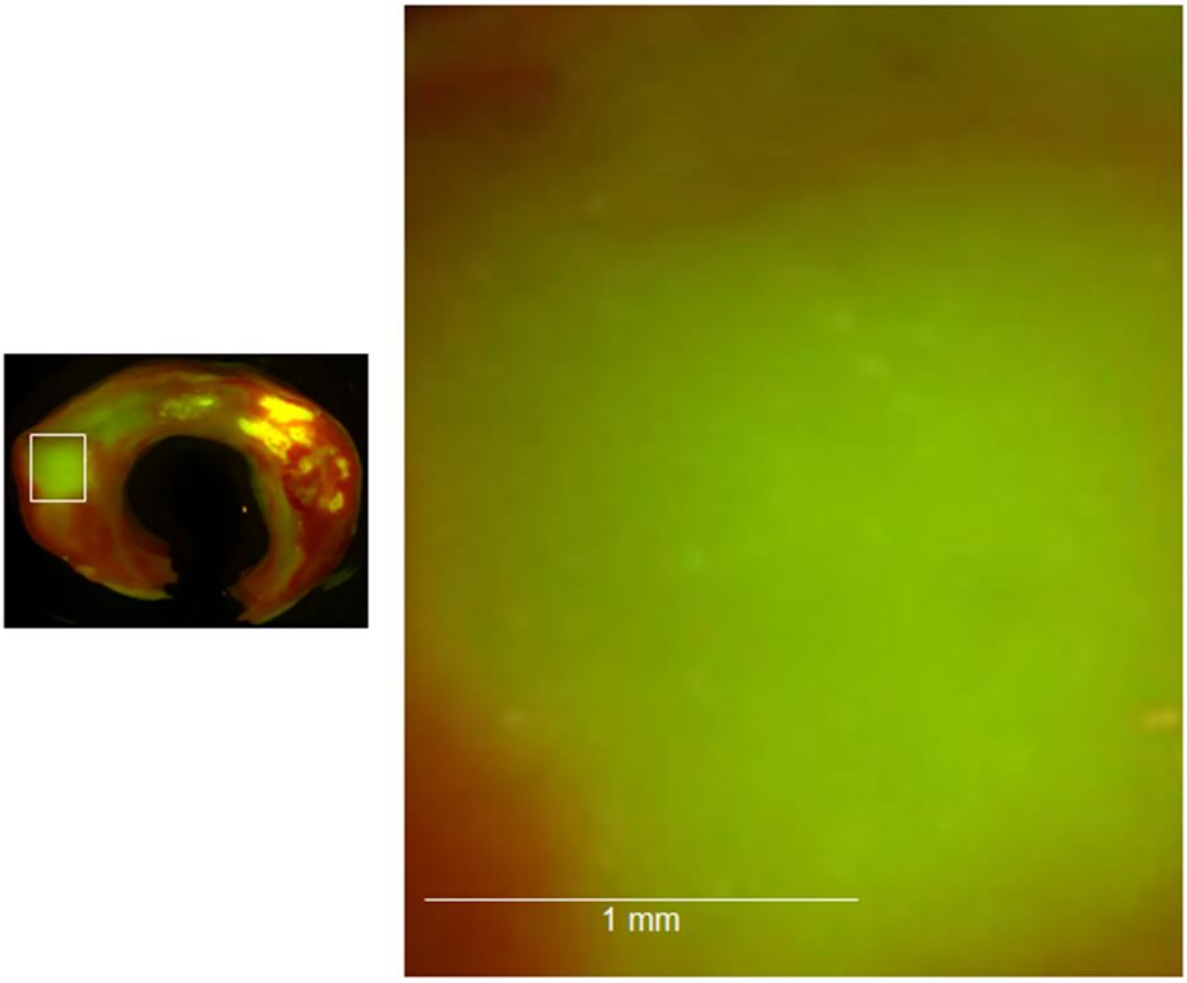

Figure 3.8: Granular appearance of autofluorescence in the non-staining region of the lipid core. A close-up of the region in the white box on the left from Figure 3.7 (a). It is possible that the brighter, granule-like shapes may be sub-voxel sized microcalcifications, ceroid-like deposits, cholesterol crystals or pockets of un-crystallized cholesterol, but their make-up has not been determined.

The composite MARS material images and a single energy bin's attenuation data (30 keV) show clear spatial agreement (Figure 3.6 e, f).

Quantitative comparison of the MD concentrations with HU values in the 30 keV energy bin are summarized in Table 3.2 for the lipid core ROI and, for reference, the calibration phantoms. For all ROI voxels with a positive lipid value, the mean concentration of 260 mg lipid / ml corresponds to ~27% lipid by weight, assuming approximately water density for the remaining material in the voxel. The lipid-containing voxels measure ~23 mm^3 while the entire ROI measures ~68 mm^3.

Of the 93810 voxels in the ROI, 3444 were calcified, with 1950 measuring above the 12 mg/ml limit. The 1494 voxels measuring below 12 mg/ml are not included in Table 3.1. Of

the 3444 calcified voxels, 83 are isolated single voxels surrounded by soft tissue. The 12 mg/ml threshold was chosen for a conservative approach to the data, but it should be noted that many of the voxels below that value probably represent true calcium detection and future testing and refining of the scanner may allow assessment of such low concentrations.

Table 3.2: Comparison of MD quantification to attenuation values for lipid and calcium

ROI	Lipid Core with Spotty Calcium			Calibration Phantoms			
Material	Soft Tissue Lipid > 0	All Soft Tissue	Calcium-like > 12 mg/ml	Lipid	Ca 50	Ca 150	Ca 250
# of Voxels	31954	90366	1950	42054	30798	33024	33024
Mean Concentration in mg/ml	260 lipid	92 lipid	41 $CaCl_2$	910 lipid	50 $CaCl_2$	150 $CaCl_2$	250 $CaCl_2$
Mean HU 37.5 keV bin	-22	30	123	-172	184	529	861

A pathologist reviewed the photo in Figure 3.7 (b) and identified the yellow to brown region on the left as a lipid core without obvious calcification, Figure 3.9. Areas of major calcification on the right and top of the MD were also noted.

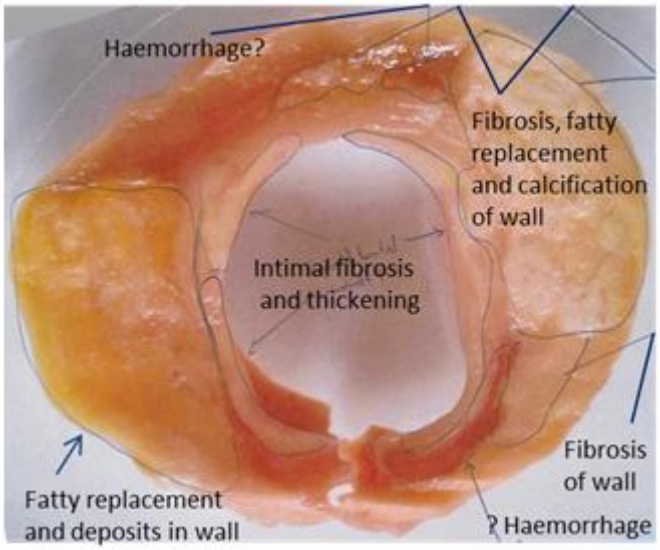

Figure 3.9: A pathologist's view of the plaque section in Figure 3.7 (b). The words are typed in by the author for easy reading, but are the exact words written by the pathologist.

Discussion

The MARS spectral CT system, using a CdTe sensor, can identify and quantify lipid rich and calcium rich regions in human atherosclerotic plaque tissue using x-ray energies (~30 to 118 keV) relevant to human scanning necessities. This feasibility study shows that a lipid core and spotty calcifications can be identified in material reconstructions. As these features are frequently present in both developing and vulnerable plaques, the information may be useful for assessing imminent and long term risks in cardiovascular disease. MARS material images are produced with automated software using the spectral data and so, offer an independent evaluation of plaque structure and composition that adds to the radiologist's toolbox. The voxel size of $(90\ \mu m)^3$ is smaller than current clinical CT and MRI [78] which may also allow detection of atherosclerotic burden at less advanced stages and smaller lesion sizes.

MARS material images match with traditional CT and histology analyses. In Figure 3.6 (e) (a customized transfer function using attenuation data from the 30 keV bin) and (f) (the composite material reconstruction) the lipid and calcium distributions follow closely with attenuation data, as would be expected in the lowest energy bin where tissue contrast is greatest. In Table 3.2, the average lipid and calcium concentrations in the lipid core ROI follow the same trends as the HU(30 keV) values. Review of tissue appearances by a pathologist also outlines macroscopic lipid rich and calcified regions in agreement with the MARS images (Figure 3.9). Fluorescence microscopy of oil-red-O stained transverse cuts of the plaque reveal extensive neutral lipid staining throughout much of the plaque (Figure 3.7 (a)). This highlights the agreement of lipid distributions in the MD for regions with little to no calcification (left hand side of Figure 3.7 (a) and (d)) but also demonstrates the limitations of the current MD, which does not allow a lipid measurement in voxels that are determined to be calcified (right hand side of the same figure panels).

Lipid measurements

The external carotid artery side of the common carotid artery contains a clear lipid core based on pathologist review of tissue photos and the fluorescence microscopy, Figure 3.9 and Figure 3.7 (a), respectively. The MARS material images have a clear lipid signal with similar shape in the same region, Figure 3.7 (d). In the voxels with lipid values greater than zero, the lipid measurement corresponds to a tissue lipid content of about 27% by wet weight (Table 3.2). By comparison, healthy aorta is only 1.8% lipid wet weight [117] and only fatty tissues such as adipose, adrenal gland and bone marrow have similar or higher lipid content. This extreme fatty content, based on the MD, and the similar shape seen in MD and photography are strong indicators that the MD can provide an image of atherosclerotic lipid core.

The large unstained region of the lipid core highlighted in Figure 3.8 may be made up of non-neutral lipids such as free cholesterol which do not stain with oil-red O, but this was not confirmed. Staining future plaques with Nile red or filipin, which both stain non-neutral lipids, might provide a more complete assessment of the lipid core [115, 118]. Another possibility is that stained material was washed away in the rinse process. However, the possibility exists that the region is low in lipid and the MD is in error. The MD does classify

some voxels that are most likely calcified as soft tissue (see Section 5.4) and these voxels usually have relatively high HU values. These voxels would likely receive lipid values of near zero and be excluded from the images shown.

Calcium measurements

Distributions of larger calcifications showed strong agreement between attenuation, MD and histology (Figure 3.7). Smaller and microcalcifications in the MD are not obvious in the attenuation and histology images; however, the correspondence between the HU based image in Figure 3.6 (e) and the MD in Figure 3.6 (f) is strong evidence that the smaller and microcalcifications are real. Sub-voxel sized HA deposits should be detectable to the MARS MD. Figure 3.10 is a plot of the expected attenuation in the 30 keV bin of hydroxyapatite in three different arrangements and compared to $CaCl_2$ which was the calibration material for calcifications in this study. The HA attenuation is graphed for, one, HA evenly distributed in water (circles), two, HA exists as a cubic particle in water (triangle pointing up) and three, HA exists as a cubic particle in adipose tissue (triangle pointing down). The values are based on attenuation data derived from the National Institute of Standards and Technology (NIST) database [119]. Three traits of this plot are important for MARS material imaging.

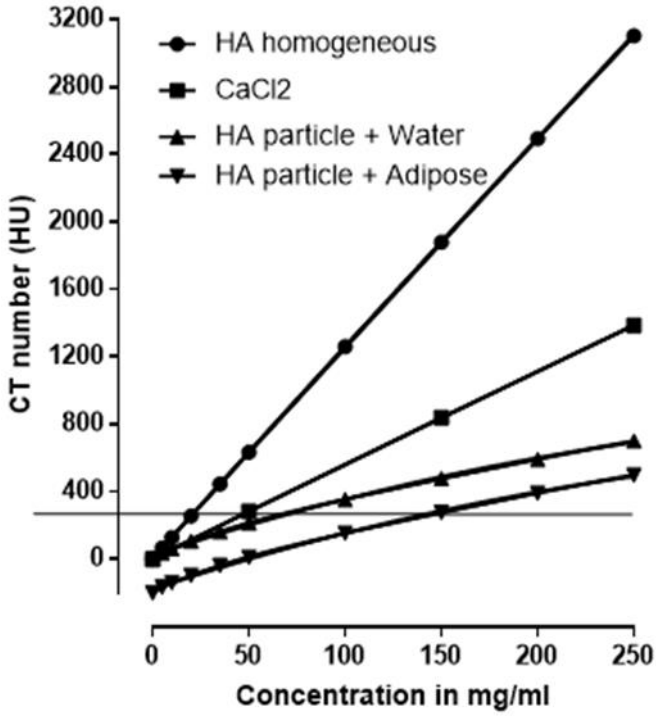

Figure 3.10: Comparison of attenuation of hydroxyapatite in three different arrangements in a 100 µm voxel. The attenuation values correspond to expected values in the 30 keV bin. Circle is HA homogeneously distributed in water, triangle pointing up is an HA particle in water and triangle pointing down is an HA particle in adipose tissue. Square is a $CaCl_2$ solution in water for comparison to the phantom standards used in this scan. The horizontal line passes through $CaCl_2$ at 50 mg/ml and highlights the broad range of actual HA concentrations that could be associated with a single $CaCl_2$ concentration at the same attenuation.

First, sub-voxel sized HA particles should be detectable. In a $(100\ \mu m)^3$ voxel, a 50 mg/ml HA cube in water has a HU (30 keV) value of 211 and is just 25.1 µm on a side.

Second, the attenuation of the same concentration of HA is highly dependent on how it is distributed. For example, 50 mg HA/ml as a single, cubic particle in adipose would have HU = 9, as a particle in water the attenuation would be HU = 211, while the same quantity of HA in water but evenly distributed throughout the voxel would have HU = 632. On the other hand, at the same attenuation, the potential HA concentration can vary widely (see horizontal line at HU = 281 for 50 mg $CaCl_2$/ml). It might be hoped that the spectral data could correct for some of this dispersion, but that issue has not been investigated yet.

Third, the MD does not account for the presence of lipid near calcifications, but there is clearly an impact on the attenuation. HA is commonly associated with lipid in atherosclerotic plaques [103]. The presence of lipid changes the attenuation and the spectral pattern. This may result in MD concentrations of calcium that are too low or, even more important with respect to detecting microcalcifications, the voxel may be classified at ST when, in fact, HA is present.

The definition of spotty calcification varies. Kataoka et al. (2012) and Ehara et al. (2004) make the key distinction that the calcification not occupy more than 90º of the vessel circumference [72, 74]. Ferencik et al. (2012) define it as isolated nodules less than 3 mm in diameter [120]. By these standards, spotty calcification is clearly detectable with the MARS MD. Some researchers would include much smaller calcifications as a sign of vulnerability to rupture. Microcalcifications are now understood to form in and around the necrotic lipid core and even in the fibrous cap, where they may form regions of stress in the cap that could lead to rupture [70, 75, 76, 108]. The MARS MD contains many calcified regions that are smaller than 1 mm^3, including isolated voxels that are surrounded by soft tissue (83 in the lipid core ROI of plaque 108). An important goal for future research with MARS will be to establish a confidence level in the reality of such small calcifications. If MARS can indeed reliably detect sub-voxel sized calcifications it could play an important role in assessing risk of plaque rupture due to microcalcifications near the fibrous cap.

When MARS scanners are more prevalent in pre-clinical and clinical research, it will be important to establish guidelines for how to interpret the concentrations of material reconstructions. As discussed in the methods, the meaning of low concentrations of lipid or calcium is difficult to assess and lower thresholds with more relevant meaning than the ones used in this study (12 mg Ca/ml and 120 mg lipid /ml, see Section 3.4 Methods) should be established.

Other limitations of this study

The material decomposition algorithm does not allow lipid assessment in voxels deemed to have calcification. This means that calcified plaque regions cannot be classified as fatty or fibrous, which could have an impact on risk assessment [53]. The next generation of MARS reconstruction which will include simultaneous reconstruction and MD, may allow three component MD of individual voxels (internal MARS communication).

The histology technique is rough. We are pursuing traditional thin section histology for future plaques but it was unavailable for this study. The presence of calcifications causes the tissues to tear during sectioning and is a major problem. The fluorescence microscopy offers excellent visualization of larger calcifications, but smaller yellow/green granules such as those seen in Figure 3.8 cannot be positively identified. Staining of our thick sections or traditional thin sections with stains for calcium (Alizarin red) or phosphate (von Kossa) might confirm the presence of microcalcifications appearing in the MD [70, 121].

Several traits of vulnerable plaque that might be identified by MARS images were not assessed. Iron differentiation from calcium was not deemed important at this time, but MARS team members are beginning work in that area of plaque imaging. Zainon et al. showed that calcifications and iron deposits could be visualized with MARS but the MD for iron separation was not reliable [100]. Wang et al. were able to quantify iron in the presence of calcium using dual energy CT [121]. Fibrous cap thickness has a strong correlation with rupture [57, 122]. Detection of the fibrous cap thickness might be assessed with MARS if appropriate thresholds for lipid content were established and effective blood pool contrast agents that do not diffuse into the cap were used, but this is speculation. Positive remodelling might also be assessed with MARS images, again, probably with the use of contrast agents. Inflammation and macrophage content could also be imaged with properly targeted contrasts (see Section 2.7 and Chapter 4).

3.5 Scanning and monitoring live samples

3.5.1 Live excised plaque

Introduction

Aim

As a developmental technology, the MARS scanners capabilities are modified and upgraded on a regular basis. Hardware and software changes were expected (and have since) to bring scan times from hours to minutes. In anticipation of this we began some simple tests to confirm that living tissues could be scanned without severe impacts to viability. This project was designed as a simple introduction to MARS scanners for an undergraduate summer student, Hayley Schoch.

Our lab cultures freshly excised carotid plaques for up to four days [123]. We wanted to test if plaque sections could be cultured after scanning with minimal impact on the plaque responses. As with any summer student project we wanted to expose an undergraduate to new procedures and technologies.

Significance

Showing that live carotid plaque samples could be scanned with minimal impact on plaque physiology is a first step in developing a whole new line of research where plaque traits such as lipid and calcification content can be measured and correlated with biochemical research done in a tissue culture model [124]

Contribution

I worked closely with Hayley on all aspects of her work, from tissue culture, to lactate measurements, to scanning and visualization.

Methods

Scan parameters appear in Table 3.1 for plaque 90.

Human carotid endarterectomy samples are used for scanning and obtained under human ethics approval reference CTY/01/04/036/AM05. A freshly excised carotid endarterectomy sample was acquired from surgical theatre. It was transported on ice to a PC2 lab where it was rinsed for five minutes in PBS, then cut into six transverse sections of about 4 mm thick with a scalpel. Three sections were randomly assigned to be scanned, while three were placed in an adjacent scanner but without scanning. The scanned sections were exposed to x-rays for 20 minutes in a pseudo-scan, as this was expected to be longer than any upcoming scans with new faster hardware.

After treatment, the six sections were returned to a PC2 lab, weighed and cultured in Gibco™ RPMI 1640 media with 10% human serum. At 24 and 48 hours the culture media was pipetted off and placed in a sterile, polypropylene centrifuge tube. Fresh media was then added. Used media was analysed for lactate production using a colourimetric lactate assay kit. The lactate assay is used as a measure of overall metabolic activity. Lower lactate production indicates less activity. After two days of culture the sections were returned to the MARS scanner for a true scan and then stored in a -80C freezer.

Results

Lactate production over 24 and 48 hours is shown in Figure 3.11 (a). Data are reported as mg Lactate/ g wet tissue weight. There was no significant difference in lactate production between the X-ray exposed sections and the controls at either 24 or 48 hours.

Discussion

X-ray treated plaque tissue was unaffected metabolically compared to controls according to lactate production on a per gram wet weight basis. This result was a strong initial indicator for the MARS team that tissue culture experiments could be performed on plaque samples after CT scanning with minimal impact on plaque behaviour.

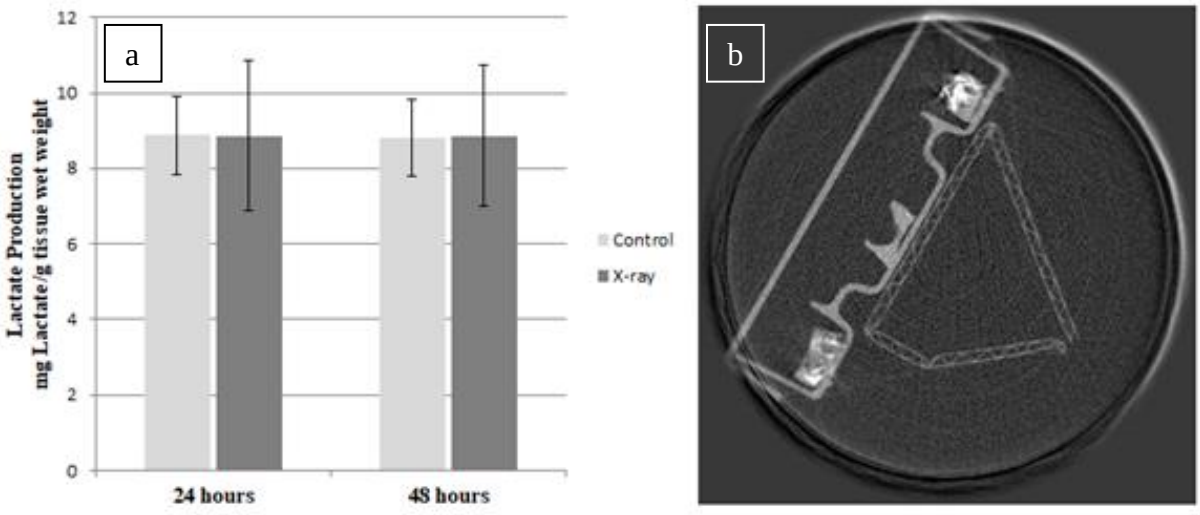

Figure 3.11: (a) Lactate production over 48 hours with and without 20 minutes of X-ray exposure. Bars are standard error of the mean. (b) Reconstructed slice of the three plaque sections exposed to X-rays. The actual scan was performed after completion of the experiment since scan times were still in the 2 hour range.

3.5.2 Monitoring Mice

Introduction

Aim

The MARS small animal scanner is designed to be used on living laboratory animals such as mice and rats. In preparation for faster scan times that would allow live animal scanning, we began testing animal monitoring equipment for ease of use and to strategize techniques inside the scanner. Monitoring provides data concerning the animal's status, as well as physiological measurements that can be correlated with MARS scan data.

We sponsored a summer undergraduate student project to set up the equipment and test it on live animals outside the machine. UC undergraduate Dylan Paterson carried out this work.

Significance

This work helped move the MARS team closer to live animal scanning. It also revealed some of the difficulties associated with using the animal monitoring equipment. It also provided experience to Dylan in using scientific equipment and dealing with live animals.

Contribution

I worked with Dylan in all aspects of this work except the retrospective gating program and performed all animal handling.

Methods

Live mice were anaesthetized with inhalation of isoflurane. After mice were unresponsive to a toe pinch, the monitoring equipment was applied. Respiration was monitored with a pressure sensitive pillow placed under the rib cage. Temperature was monitored by rectal fibre optic probe. Transmissive pulse oximetry was attempted on the tail and the ankle with a general purpose clip and special purpose ankle/tail holder.

Six mice were monitored with all equipment simultaneously. Six more mice were monitored for temperature only over a ten minute period to assess temperature changes in the mice during anaesthesia with and without a heating pad set to 37C.

Results

Mice were successfully monitored for respiration rate, temperature and pulse oximetry. However, the pulse oximeter was problematic. The general pulse-ox clip could not be made to acquire data. The specialized clip was very difficult to use. It could not be made to acquire data on the tail. It was very difficult to apply to the ankle, requiring a customized technique in which the ankle was pulled though the clips ring with a thread taped to the mouse's foot. Only 1 mouse of the six was successfully monitored with pulse-ox.

Breathing rate data was used to develop a retrospective gating program that could choose time correlated CT images with the same point in the breath cycle and reject projections taken during breath movements. The program was tested on an old CT and respiration dataset from a live mouse scan (source unknown) and found 55% to 60% of projections were retained.

Mice placed on a heating pad had better temperature stability. Heated mice dropped in rectal temperature by an average of 0.63C in 10 minutes while unheated mice cooled by an average of 2.8C in ten minutes

Discussion

The work revealed some of the difficulties that will be encountered in live animal scanning. The Pulse oximeter is difficult enough to use that we recommended looking for other designs. The layout of the measuring devices will require a mouse bed in the scanner that holds the animal in place because mice had a tendency to slip off the respiration pillow. The temperature probe on the other hand was easy to use and could be taped in place.

3.6 Conclusion

Material reconstruction of the spatial arrangement of lipid and calcium-rich regions in atherosclerotic plaque was successful using photon energies relevant to human imaging (30 to 120 keV).

A series of studies demonstrated the potential to identify lipid-rich and calcium-rich components in tissue samples using the MARS spectral CT scanner to generate material

volumes. Lipid and calcium components were identified on a macroscopic scale in a lamb tissue sample and on a smaller, microscopic scale in excised carotid plaque samples that demonstrates the superior spatial resolution of MARS scanners compared to current clinical CT.

GaAs and CdTe are suitable sensor materials for obtaining accurate MD of lipid and calcium components of atherosclerotic plaque. Both SPM and CSM generate quality spectral data sets that allow MARS MD software to discriminate intrinsic material arrangements.

Lipid and calcium MD separation from surrounding tissues mean that two intrinsic markers of atherosclerotic plaques that are at risk for rupture can be identified in material reconstructions: the necrotic lipid core and spotty calcifications. Histologic examination confirmed the macroscopic arrangement of a lipid core and spotty calcifications with good spatial agreement between photography, attenuation data and MD results.

In future, human versions of the MARS scanner, atherosclerotic burden may be assessable with detection of lipid cores and spotty calcifications in plaques of various stages of development, not just vulnerable advanced plaques.

Live tissue scanning was shown to be feasible in a twenty minute scan.

The first steps toward live animal monitoring in a MARS scanner were taken.

4 Contrast Enhanced Imaging with MARS

4.1 Introduction

MARS scanners use spectral patterns to identify materials of interest to the researcher or clinician. In combination with contrast agents, a powerful new tool will be developed in diagnosing, treating and assessing treatment of disease and injury. With four to eight energy bins, MARS scanners can be used for K-edge imaging to identify multiple contrast agents simultaneously while maintaining the ability to discern intrinsic material arrangements of lipid and calcium that are also important in disease and injury assessment (see Chapter 2). Current clinical CT can only discern contrast agents from body structures because of known spatial arrangements in the body and very high attenuations from high contrast concentration. Dual energy CT can identify materials by a spectral signature, but is limited to two materials [22, 125].

Material identification in contrast enhanced CT has many potential benefits. The ability to reliably differentiate contrast agents from calcifications is one area where MD with spectral CT will aid clinicians. Atherosclerosis is characterized by calcifications, usually hydroxyapatite, varying in size from nanometres to millimetres. With neovascularization and diffusion, contrast agents move into the plaque from the adventitia and the lumen, requiring rapid CT acquisition to avoid contrast blurring of the lumen and intraplaque features [68]. Accurate MD separation of contrast and intrinsic materials may relax the need for rapid acquisition and enable positive identification of small, spotty calcifications (especially ones in the fibrous cap) even in a background of contrast agent.

Another example of a possible benefit of MD over attenuation based CT is in repeat scans of patients with subdural effusions. An initial iodine enhanced scan reveals a hyperdense subdural effusion due to extravasation of contrast. On subsequent noncontrast scans, residual iodine can lead to misidentification of the effusion as a subdural hematoma (which is hyperdense in noncontrast scans) [126]. Accurate MD would identify the residual iodine in the second scan, preventing misidentification.

Energy threshold settings establish the spectral pattern used in MD so it is important to consider the best values for identifying the high-Z materials of interest. K-edges of high-Z contrasts largely dictate the placement of thresholds and this chapter includes two phantom studies that address threshold placement and the resulting MD of three contrasts, calcium, lipid and water components. Iodine, gadolinium and gold are used for these studies because of their prevalence in approved human medical imaging (iodine [127–129]and gadolinium [130, 131]) and current pre-clinical research (gold [132–134]).

Four scans of biological tissue are presented which highlight different aspects of contrast enhanced imaging. Plaque 82 tests the ability to discern tissue and maintain lipid and calcium MD in a background of gadolinium contrast. The tumour mouse examines the

potential for MD measurement of passive accumulation of gold nanoparticles in a tumour via the enhanced permeability and retention (EPR) effect [135]. The multi-contrast mouse demonstrates MD of six materials simultaneously in a biologic system. Finally, the macrophage scan tests the uptake of untargeted gold nanoparticles by cultured human monocyte derived macrophages (HMDMs) as a feasibility study for research using macrophage targeted gold nanoparticles. The scan parameters for all six studies are listed in Table 4.1.

Table 4.1: Scan parameters for the samples in this chapter

Sample	K-factor phantom	JSM Data paper phantom	Plaque 82	Tumour mouse	Multi-contrast mouse	Macrophages
Detector	Medipix3 RX	Medipix3 RX	Medipix3 RX	Medipix3 RX	Medipix3 RX	Medipix3RX
Sensor	2 mm CdTe	2 mm CdTe	2 mm CdTe	2 mm CdTe	2 mm CZT	2 mm CZT
Camera mode	CSM	CSM	CSM	CSM	CSM	CSM
Bias voltage (V)	-600	-600	-600	-600	-600	-600
Pixel matrix	128 x 128	128 x 128	128 x 128	128 x 128	128 x 128	128 x 128
Pixel pitch (µm)	110	110	110	110	110	110
SDD (mm)	201	250	250	170	250	250
SOD (mm)	150	200	200	115	200	200
Magnification	1.34	1.25	1.25	1.48	1.25	1.25
Projections/ rotation	720	720	720	720	720	720
Flatfields	720	720	720	720	720	720
Tube Voltage (kV)	118	118	118	118	118	118
Tube Current (µA)	27	13	24	18	24	13
Exposure (ms)	120	300	220	200	220	300
Filtration (mm) Al or brass	3.8 Al (1.8 intrinsic + 2 added)	1.8 Al intrinsic	1.8 Al intrinsic + 0.375 brass	3.8 Al (1.8 intrinsic + 2 added)	1.8 Al intrinsic + 0.375 brass	3.8 Al (1.8 intrinsic + 2 added)
Thresholds (keV)	See Table 4.3, schemes B	18, 30, 45, 78	30, 40, 50, 60	28, 48, 68, 81	27, 36, 52, 79	18, 30, 45, 75

	and D					
Focal spot (μm)	~50	~50	~50	~50	~50	~50
Reconstruction algorithm	mART	mART	mART	mART	mART	mART
Voxel size $(\mu m)^3$	180	90	90	100	100	100

4.2 The K-factor: Choosing thresholds for multiple k-edge contrast materials

Introduction

Aim

This work developed and tested a scheme for calculating the optimal energy threshold settings to be used in multiple K-edge imaging with spectral CT. It accounts for the trade-off between maximizing the difference in signal between adjacent energy bins and maintaining a strong signal to noise ratio for all bins.

Within the limits of the noise floor at the low energy end and the maximum photon energy in a scan protocol, the energy threshold choices for the MARS camera energy bins are entirely arbitrary. He et al. developed the signal difference to noise ratio (SDNR) to determine the optimal energy bins for discrimination of a single K-edge but provided no procedure for imaging with multiple K-edges simultaneously [136, 137]. The SDNR combines differences in attenuation above and below the K-edge with values for the noise in each bin to obtain a single value that is maximized to optimize bin selection. Our study separates the attenuation and noise components and develops a simple ranking system for choosing the optimal thresholds for the four CSM counters given a particular scan protocol and set of K-edge contrast agents. The technique is based on two simple measures of information quality. First, the K-factor is introduced to quantify the spectral difference between adjacent energy bins on either side of the K-edge of each contrast agent. Second, the percentage of the total spectrum contained in the energy bin that lies just above the K-edge for each material is used as a theoretical measure of the signal to noise ratio (SNR).

The results of the ranking system are tested with real data sets using two threshold schemes and comparing the measured values of the K-factor and the signal to noise ratio (SNR).

Significance

The technique provides a simple way of assessing threshold schemes for identification of multiple contrast agents.

Publication

This work is featured in the Journal of Instrumentation [138]

Contribution

I produced the phantoms used and was involved in concept and manuscript development.

Methods

In K-edge imaging, there is a trade-off between spectral information, which is maximized by the difference between attenuation of adjacent energy bins, and SNR within an energy range. Narrow energy bins maximize energy information by maximizing the difference between the effective energy of adjacent energy bins. Wide bins maximize SNR, which is approximately equal to the square root of the X-ray intensity, simply by containing more counts.

The K-factor is introduced to provide a quantitative measure of the quality of the energy information between two energy bins on either side of a material's K-edge.

$$K - factor = \frac{(X\text{-}ray\ attenuation\ of\ the\ energy\ bin\ above\ the\ K\text{-}edge)100\%}{(X\text{-}ray\ attenuation\ of\ the\ energy\ bin\ below\ the\ K\text{-}edge)} \quad (4.1)$$

It is simply the ratio of the theoretical mass attenuation of a material for two adjacent energy bins on either side of its K-edge multiplied by 100 to create a convenient number. A higher K-factor implies better energy information. A particular threshold protocol gives a K-factor for each material. To compare different protocols the K-factors are ranked within each material and the ranks for each protocol are summed. The lower the sum, the better the protocol with respect to overall energy information

For the theoretical assessment of SNR, the technique simply uses the percentage of the X-ray spectrum contained within the above K-edge energy bin for each element. Protocols are again ranked within each material based on the percentage, with a larger percentage ranking higher. The X-ray intensity ranks are summed within each protocol and the lower the sum the better the overall noise ranking.

Finally, the two summed values for each protocol, K-factor and intensity, are added together and the protocols ranked from lowest total to highest. Ties are broken by opting for the protocol with a better theoretical K-factor sum.

Theoretical protocol ranking was performed for five possible threshold schemes for distinguishing iodine, gadolinium and gold. The top two protocols were used to scan a multi-contrast phantom with identical settings other than thresholds. Then, the reconstructed data were used to calculate measured K-factor and SNR values and assess the results of the theoretical technique. Measured K-factor is based on mass attenuation coefficients calculated for the highest concentration of each contrast. SNR is calculated from the mean of 720 flatfields for each energy bin of interest divided by its standard deviation.

The scan protocol is described in Table 4.1.

Results

The threshold schemes and resulting theoretical K-factor and X-ray intensity ranks are shown in Table 4.2. Scheme D scores the lowest with a total of 9, followed by schemes A and B with 15. Scheme B is chosen for measured comparison to scheme D based on a lower K-factor sum (8 for B, 9 for A). The final rankings are shown in Table 4.3.

Table 4.2: Comparison of five different threshold schemes for K-factor and estimated percentage of spectrum photons in the over K-edge energy bin (i.e. the bin which will show an increase in attenuation relative to the adjacent lower energy bin). Used with permission [138]

			K-factor		X-ray intensity	
Element	Scheme	Energy range (keV)	Value (%)	Rank	Value (%)	Rank
iodine	A	19-32, 32-52	204	3	35	2
	B	25-35, 35-55	248	2	35	2
	C	21-35, 35-54	161	5	33	3
	D	27-33, 33-49	668	1	29	4
	E	20-35, 35-60	167	4	49	1
gadolinium	A	32-52, 52-83	185	2	42	2
	B	35-55, 55-82	139	4	37	4
	C	35-54, 54-85	172	3	40	3
	D	33-49, 49-81	287	1	46	1
	E	35-60, 60-85	79	5	23	5
gold	A	52-83, 83-118	146	4	11	2
	B	55-82, 82-118	193	2	12	1
	C	54-85, 85-118	130	5	10	3
	D	49-81, 81-118	204	1	12	1
	E	60-85, 85-118	170	3	10	3

Table 4.3: Ranking the five sample threshold protocols. Used with permission [138]

Scheme	Energy range (keV)	Overall rank
A	19-32, 32-52, 52-83, 83-118	2
B	**25-35, 35-55, 55-82, 82-118**	**2**
C	21-35, 35-54, 54-85, 85-118	4
D	**27-33, 33-49, 49-81, 81-118**	**1**
E	20-35, 35-60, 60-85, 85-118	3

The measured K-factor and signal to noise ratio (SNR) data for the two schemes are compared in Figure 4.1. Scheme D outperforms scheme B in all measures except the SNR for iodine.

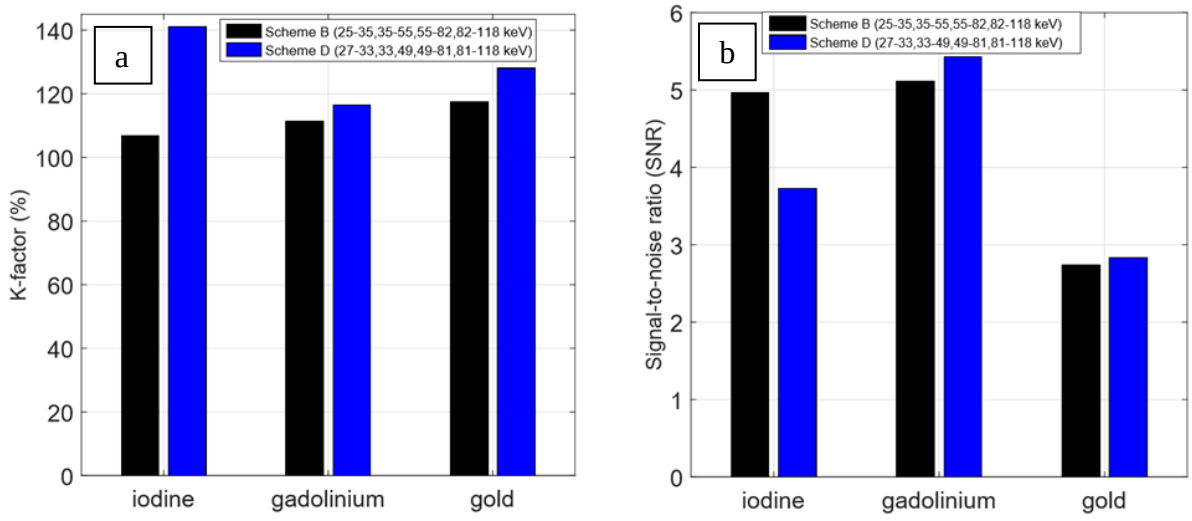

Figure 4.1: Comparison of measured K-factors and SNRs between schemes B and D. (a) measured K-factor for the highest concentration of iodine, gadolinium and gold phantoms and (b) measured SNR for the above K-edge energy bin for each material and protocol. Used with permission [138]

Scheme D proves to be more informative overall than scheme B. All following analyses are for scheme D only.

Figure 4.2 illustrates the quality of the scheme D data. The K-edge is clearly visible for even the lowest concentrations of each high-Z contrast. The MD image in Figure 4.2 (d) shows excellent separation of materials, with little to no visible crosstalk.

Discussion

The theoretical calculations of K-factor and X-ray intensity showed scheme D was clearly superior to the other four threshold schemes. In testing vs scheme B, scheme D proved superior in K-factor for all three elements and in SNR for gadolinium and gold. Only the iodine SNR was inferior for scheme D and that is in keeping with its poor theoretical score for iodine's above K-edge X-ray intensity percentage (Table 4.2). The measured K-factors for scheme D (all below 140% or lower) are below the theoretical values (all above 204%). This is an indicator of the noise in the system and probably represents the strong effect of threshold dispersion in the energy calibration (see Chapter 6), which blurs the spectral distinction between adjacent energy bins [11].

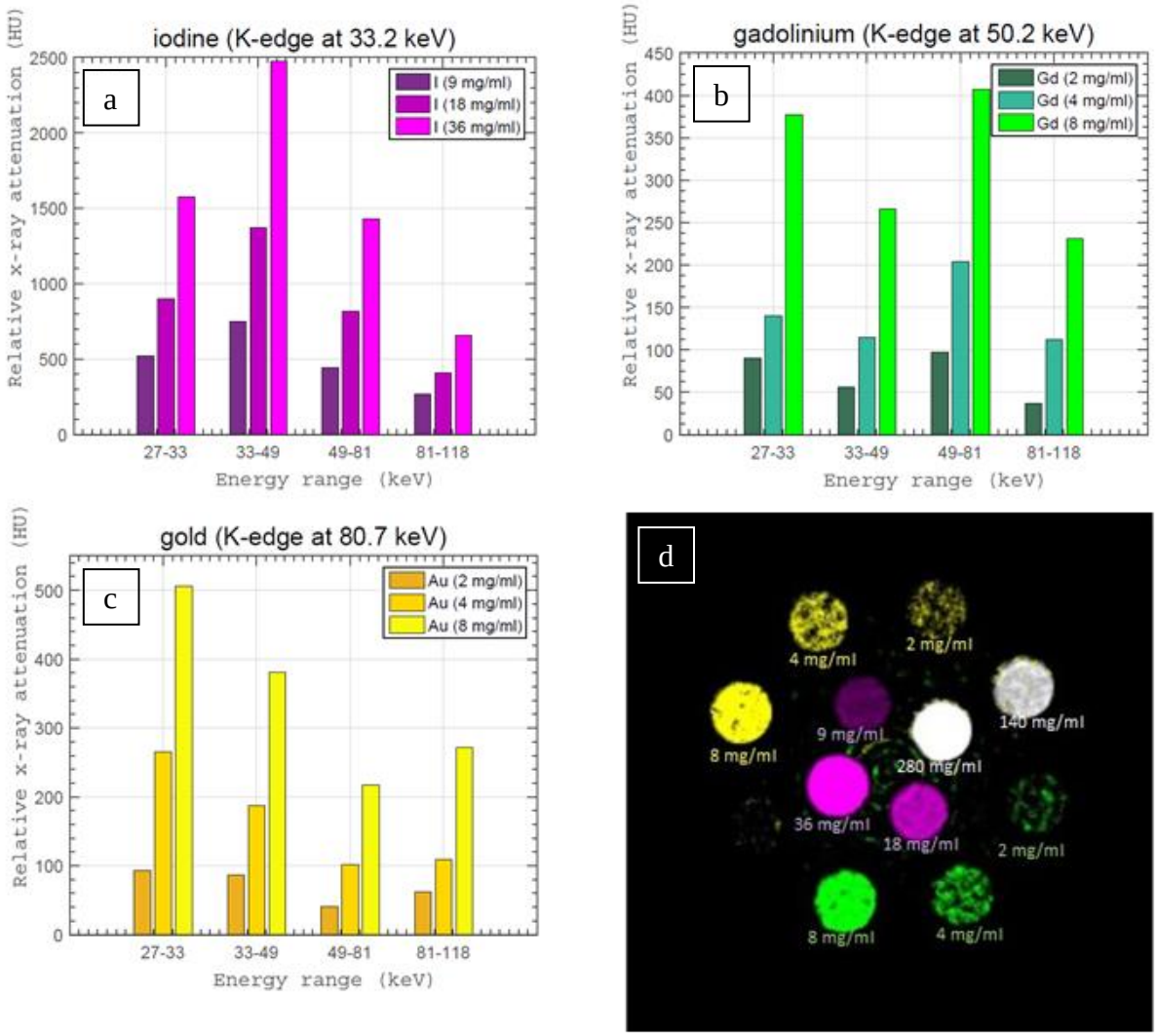

Figure 4.2: K-edge detection and resulting MD for scheme D. The increase in attenuation (Hounsfield units) relative to water is apparent from the below to above K-edge energy bins at all concentrations for (a) iodine, K-edge = 33.2 keV, (b) gadolinium, K-edge = 50.2 keV, and (c) gold, K-edge = 80.7 keV. The MD of the phantom (d) with purple for iodine, green for gadolinium, yellow for gold and white for calcium. Concentrations are in mg element/ml solution except for calcium which is mg $CaCl_2$/ml solution. Used with permission [138]

The two part ranking technique using the K-factor to evaluate energy information and X-ray intensity to evaluate SNR provides a simple, objective format for choosing optimal energy threshold schemes. The five component MD of a multi-contrast phantom shows the quality of the scheme "chosen" by the technique. The technique is easily applied to any contrast agents with K-edges in the X-ray spectrum used. Libraries of K-factor and SNR values could be developed for a range of contrasts and scan protocols (i.e. different X-ray spectrum and threshold combinations).

This study did not examine a technique for optimizing thresholds by calculating K-factor/SNR scores across the continuum of possible combinations. While this would require significant computing effort, all of the math is simplistic and could be automated with software.

4.3 Six material MD of a multi-contrast phantom

Introduction

Aim

This phantom study was formulated with the idea of demonstrating the MARS scanner's ability to distinguish six materials, four of which are high-Z, using photon energies relevant to human imaging. Only intrinsic source filtration is used, so low energy photons (below 30 keV) are still present in significant quantity. Lipid and water components are distinguished as well as calcium, iodine, gadolinium and gold. Like the lamb tissue data set (Section 3.2), the raw, partially processed and fully processed data is made available to the public for examination.

Significance

This phantom study demonstrates six material MD using CSM and four energy bins with an X-ray spectrum spanning 18 keV to 118 keV. It also introduces the identification chart which provides a simple display of the sensitivity and crosstalk in the MD. As the MARS scanner and software packages mature and stabilize, the team is moving into more stringent analysis of correct MD identification and quantification.

Publication

This work is published in JSM Biomedical Imaging Data Papers, [139]

Contribution

I produced all the phantoms used in this study. I was part of the protocol development team and participated in manuscript editing.

Methods

The phantom layout is shown in the left side of Figure 4.3. Gold is gold chloride (Salt Lake Metal, Salt Lake City, UT, USA). Gadolinium is MultiHance (Bracco Diagnostics Inc., Milan, Italy). Iodine is Omnipaque 300 (GE Healthcare, Chicago, IL, USA) and calcium is calcium chloride (BDH Laboratory Supplies, Poole, UK). The phantom holder is Polymethyl methacrylate (PMMA).

The scan protocol is listed in Table 4.1. The energy bins are set so that each of the three highest bins encompasses one K-edge (iodine (30 to 45 keV, K-edge = 33.2 keV), gadolinium (45 to 78 keV, K-edge = 50.2 keV) and gold (78 to 118 keV, K-edge = 80.7 keV)).

A 900 voxel ROI in each phantom was used to generate the identification chart. Voxels are assessed for which materials are present (water is ignored unless the voxel concentration of the other material present is zero).

Results

The attenuation reconstruction of a transverse slice is shown in Figure 4.3. The K-edge effect is visible for the highest concentration of iodine, gadolinium and gold. In the lower concentrations it is more difficult to discern, except for iodine where it is still obvious at 18 mg I/ml. However, the data for the lower concentrations still shows the K-edge effect for Gd and Au (data not shown).

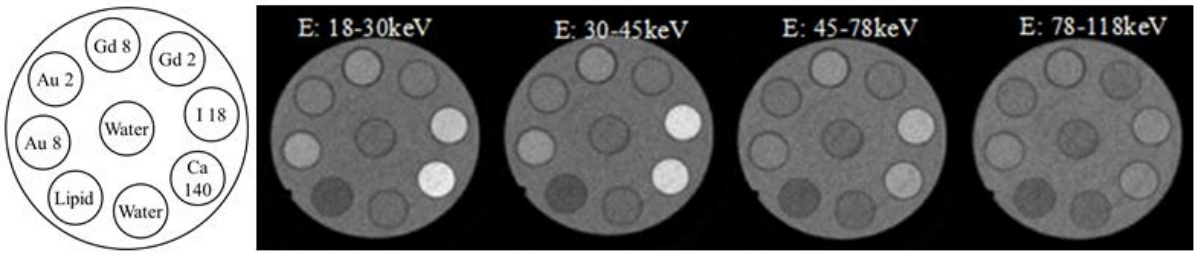

Figure 4.3: Attenuation of the six material phantom in four energy bins. In the schematic, for gold, gadolinium and iodine the numbers represent mg of element/ml of solution while for calcium the concentration is 140 mg $CaCl_2$/ml solution. The grayscale is in HU with a window of -1000 to 1500. Used with permission [139]

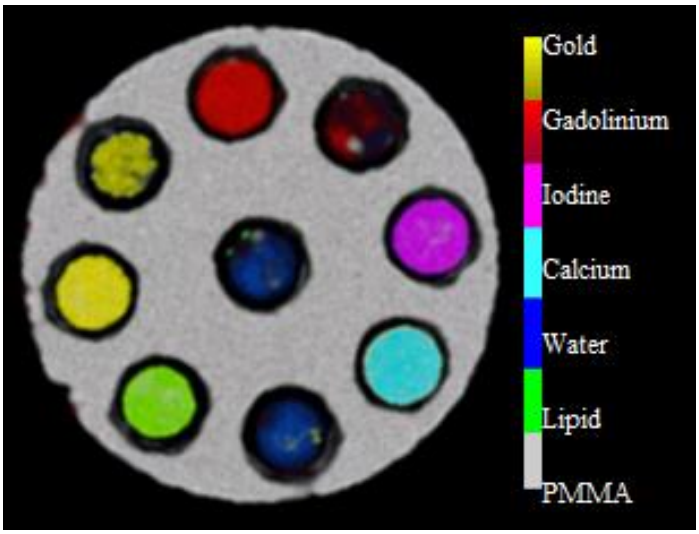

Figure 4.4: MD of the six material phantom. Materials are in the same arrangement as the schematic in Figure 4.3. The PMMA spectral signal was added to the MD as a seventh material to separate it in the images for a clean look but the technique would not be applicable in MD of unknown samples. Used with permission [139]

The MD distinguished all materials but significant crosstalk occurs for 2 mg Gd/ml (Figure 4.4). All other phantoms are correctly identified in over 80% of voxels (Figure 4.5).

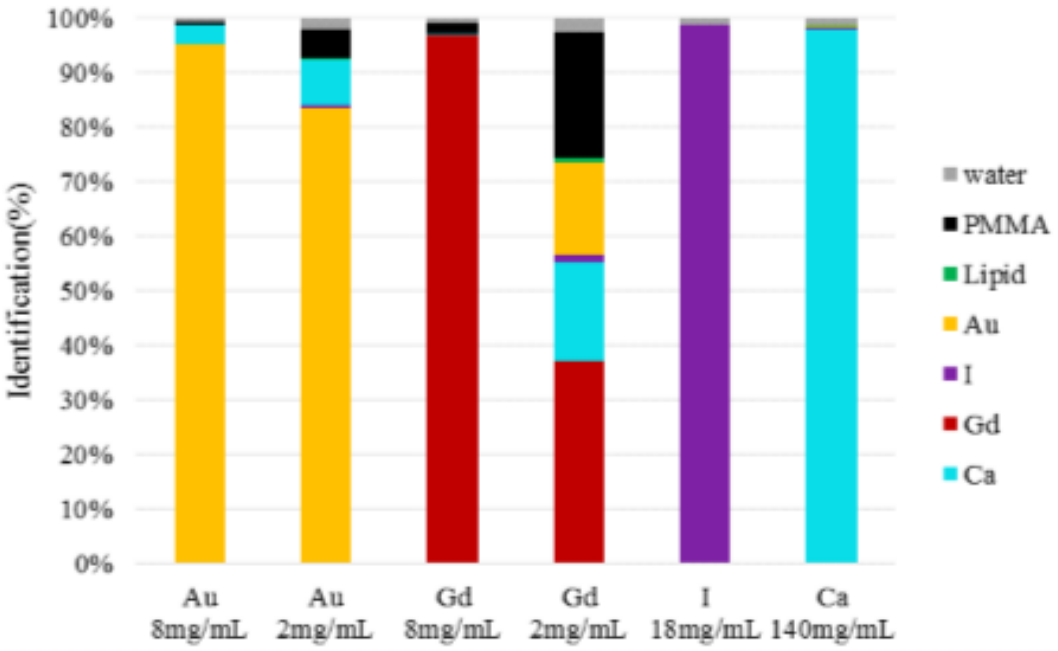

Figure 4.5: Identification chart. Each bar represents the calibration vial listed at the bottom of the chart. The colour bands represent the percentage of each vial identified as containing the corresponding material, i.e. yellow is the percentage of voxels identified as gold, red as gadolinium etc. as shown in the legend on the right. Since all voxels have a water value, the water percentage is only voxels that have a concentration of zero for the other materials. Alternatively, a lipid voxel is any voxel with a lipid concentration above zero. Used with permission [139]

Discussion

A six material phantom was successfully decomposed. The identification chart (Figure 4.5) shows the high quality of the sensitivity at higher concentrations for all materials. The gradual decay in sensitivity as concentrations decrease is seen in the 2 mg Au/ml and especially the 2 mg Gd/ml phantoms. The MD might be improved by using alternative thresholds, perhaps by using the K-factor technique described in Section 4.2, but this was not attempted. Making the data set available to the public marks the first full MARS dataset that includes high-Z contrasts that can be analysed by independent parties.

4.4 Plaque 82: MD of submersion in gadolinium contrast

Introduction

Aim

This study tested the ability to visualize an excised carotid plaque when submerged in a water based gadolinium contrast solution and to distinguish lipid, calcium and gadolinium components. Visualization in air provides excellent contrast for the tissue outline, but does not resemble the reality of *in vivo* scanning. Submerging a plaque in contrast agent provides

a middle ground between air and unenhanced CT imaging in water or *in vivo* while roughly simulating a contrast enhanced CT scan. The study sought to observe the diffusion of contrast into the plaque. Would a hydrophilic contrast agent diffuse throughout the plaque, or would it be excluded from the more hydrophobic lipid core? Would the lipid and calcium signals be maintained in a background of high-Z material? Both the air and gadolinium scans were performed at 118 peak kilovoltage (kVp) with filtration to eliminate photons below ~30 keV. Like plaque 108 (Section 3.4), this simulates a true human scan.

Significance

Again, all results are accomplished while scanning in the human diagnostic energy range above ~30 keV. This study shows that the MARS MD quantitative data allows concentration gradients in high-Z materials to be used in conjunction with a customized transfer function to visualize tissue details. It also demonstrates that the lipid and calcium MD are relatively stable between scans in air and submerged in contrast solution. Scan results indicate that hydrophilic contrast agents may not significantly diffuse into high lipid regions which may translate to more reliable identification of lipid core atheromas in clinical enhanced CT.

Publication

A manuscript is in development for submission to European Radiology

Contribution

I carried out all aspects of this work.

Methods

A calibration phantom was assembled as shown in the left side of Figure 4.6. Hydroxyapatite nanoparticle in resin phantoms were used in place of the $CaCl_2$ solutions of the past. For material calibration, the phantom was scanned in air prior to plaque scanning.

Human carotid endarterectomy samples are used for scanning and obtained under human ethics approval reference CTY/01/04/036/AM05. A carotid endarterectomy sample was acquired from surgical theatre and frozen in a -80C freezer. The calibration phantom and both plaque scans were performed in the same day following the protocol listed in Table 4.1 for plaque 82. The plaque was removed from the freezer and allowed to thaw at room temperature in a sealed tube with moist cotton to maintain 100% humidity. The plaque was scanned in the tube. Immediately following the air scan, the plaque was transferred to another polypropylene tube filled with Gadovist® 1.0 Contrast (Bayer, Inc., Leverkusen, Germany) diluted to 6 mg Gd/ml solution. Air bubbles were gently separated from the plaque and then the tube was sealed and allowed to stand at room temperature for two hours to allow the gadolinium contrast time to diffuse into the tissue. The plaque was then scanned again.

The MD follows the criteria for plaque 108. The lipid component is displayed only above 120 mg/ml and the calcium component is displayed above 12 mg HA/ml, although this may

have a different meaning with the change from a $CaCl_2$ water solution phantom to an HA nanoparticle in resin phantom (see Figure 3.10). Calcium is shown as a replacement volume in both plaque scans but not in the phantom images.

Results

The MD of the phantom is shown in Figure 4.6. The gadolinium signal is strong at 2 mg Gd/ml and present even at 1 mg Gd/ ml. The HA MD is still strong at 50mg HA/ml.

The identification chart in Figure 4.7 shows the percentage of voxels in each calibration vial that are identified as one of the four MD materials. Gadolinium is misidentified as calcium at lower concentrations, especially at 1 mg Gd/ml where just over 21% of voxels were mistakenly assigned to the HA component. On the other hand, HA is rarely misidentified as gadolinium, even at 50 mg HA/ml.

Figure 4.8 displays, roughly, the same transverse slice through the plaque for both the air and gadolinium scans. The plaque outline and lumen are visible at a transition between a strong gadolinium signal and a signal dominated by intrinsic plaque materials. The calcium and lipid components are present in similar distributions in both scans.

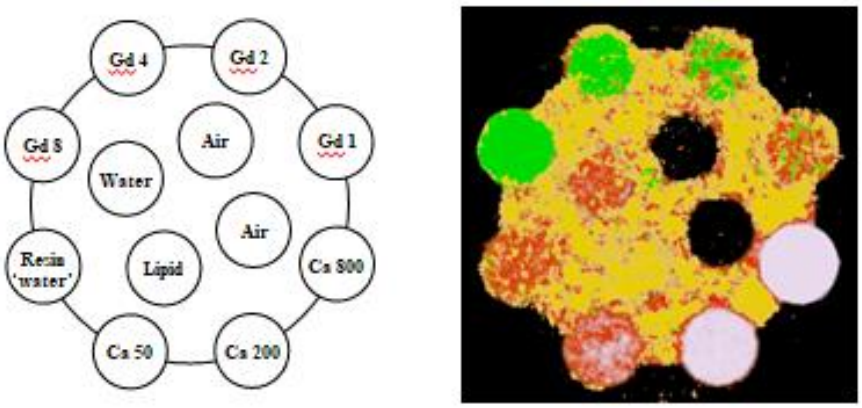

Figure 4.6: The phantom layout on the left and MD on the right. Gd # = mg of gadolinium/ml solution using Gadovist® 1.0 Contrast (Bayer, Inc., Auckland, New Zealand). Ca # = mg $Ca_5(PO_4)_3(OH)$/ml using calcium hydroxyapatite nanoparticles in resin 'water' (QRM GmbH, Moehrendorf, Germany). The MD colourmap is Gd = green, Ca = grey, Lipid = yellow, Water = red.

The three dimensional appearance of the plaque is obvious in air (Figure 4.9 (a)) and the same basic outline is present in the gadolinium scan (Figure 4.9 (b)). Without the obvious contrast of the air/tissue interface, the plaque shape in panel 4.9 (b) is revealed by the combined appearance of the microcalcifications near the plaque's outer surface and gadolinium contrast that has diffused into the tissue and been diluted in the process.

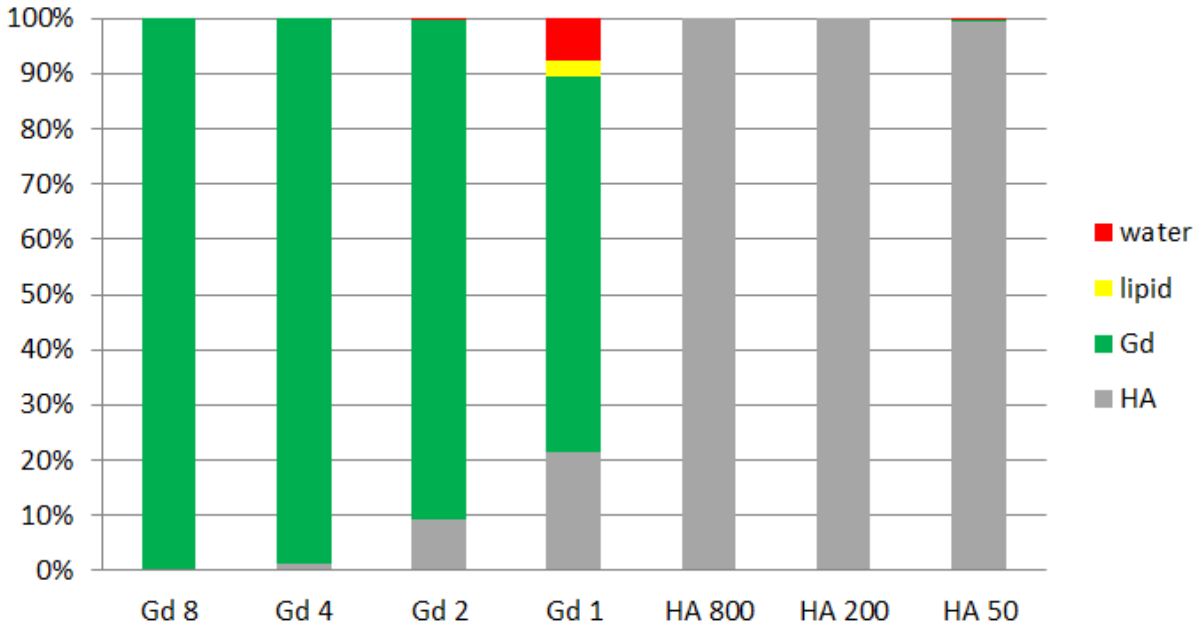

Figure 4.7: Identification chart for the four material phantom in Figure 4.6. Each column represents a vial from the phantom. Each colour represents the percentage of voxels in that vial that were identified as containing the corresponding material from the legend on the right. Since all voxels have a water value, the water percentage is only voxels that have a concentration of zero for the other materials. Alternatively, a lipid voxel is any voxel with a lipid concentration above zero.

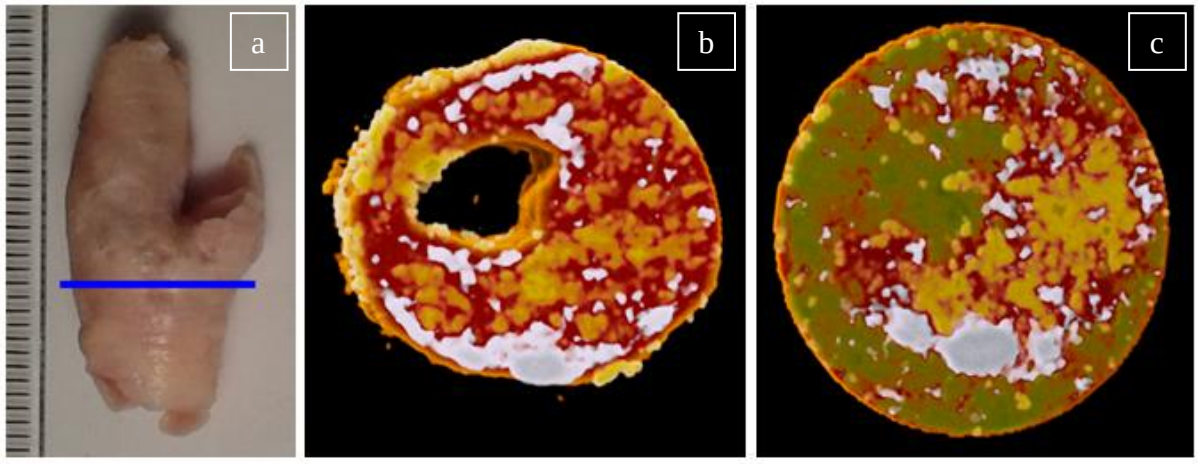

Figure 4.8: MD of a transverse slice. (a) photo of the whole plaque. The blue line shows the approximate position of the slice. The MD of roughly the same slice from scans in air (b) and in 6 mg Gd/ml (c). The lipid and calcium signals are similar in both. The colourmap follows that of Figure 4.6 but Ca is shown as a replacement volume (the water signal is ignored).

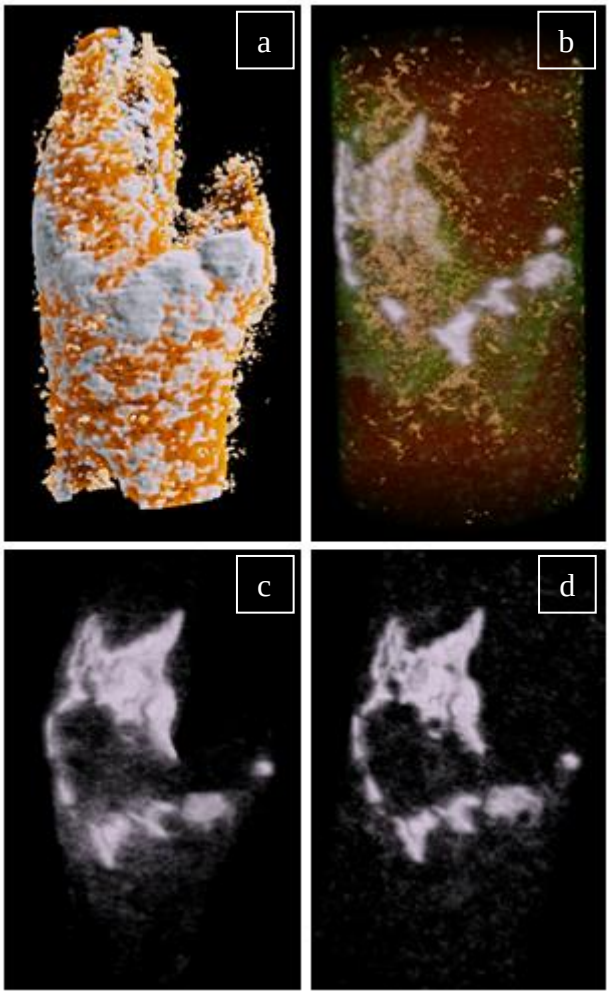

Figure 4.9: Comparison of the whole plaque in air and in 6mg Gd/ml gadolinium solution. The general shape of the plaque is seen in air (a) and the same outline is revealed by diluted gadolinium contrast that has diffused into the plaque (b). In (b) Gd is shown only between 0 and 3 mg Gd/ml solution which has eliminated the Gd from the surrounding solution but shows the diluted Gd contrast in the outer layers of the plaque. The calcium signal is virtually unchanged between the air scan (c) and the Gd scan (d). Most of the microcalcifications forming the "mesh" near the bifurcation in (c) were still detected in the Gd scan but are not shown because crosstalk from the Gd resulted in many low calcium concentration voxels in the surrounding solution and plaque periphery (see Figure 4.7). Thus, the Ca windows are > 12 mg/ml in (c) and > 25 mg/ml in (d).

Discussion

Scanning in the human CT energy range from ~30 keV to ~118 keV, lipid, calcium and gadolinium components have been differentiated in an excised carotid plaque submerged in gadolinium contrast. The key results of this study are the fidelity of the lipid and calcium signals between the air and Gd scans, the apparent exclusion of the hydrophilic Gd contrast from the lipid core and the ability to use concentration gradients in the MD to enhance the view of spatial features.

The air scan of this plaque revealed a prominent lipid core upstream from the bifurcation of the common carotid, as seen in Figure 4.8 (b), and a 'mesh' of diffuse, spotty calcifications

around the outer surface of the plaque sample, as seen in Figure 4.8 (b) and Figure 4.9 (c). Both the lipid core and the spotty calcium are also prominent in the Gd scans (Figure 4.8 (c) and Figure 4.9 (d)). This important result indicates that intrinsic material spatial arrangements that are important in assessing disease may be identified in contrast enhanced spectral scans. In particular, the mesh of calcifications near the outer surface of the plaque is present in the Gd scan. To highlight this, the thinner soft tissue of the CCA at the bottom of the plaque is not prominent in the Gd scan (compare the bottom of the plaque in Figure 4.9 (a) and (b)) but the calcium component of the Gd scan shows the plaque outline even in this area where the submersion in water-based Gd solution prevented detailed soft tissue imaging. Possibly, Gd contrast has diffused throughout this thinner region of tissue (the walls are ~0.5 mm thick), but the calcium signal is maintained. Identifying microcalcifications like these in thin fibrous caps even in the presence of diffused contrast agent could have significant benefits in clinical identification of vulnerable plaque. Furthermore, it may reduce the need for multiple scans with and without contrast, reducing patient costs, inconvenience and dose.

There is little Gd signal in the lipid core regions of the plaque (Figure 4.8 (c)), even after two hours of diffusion. This may indicate that the more hydrophobic lipid core will exclude water soluble contrast agents and lead to enhanced contrast in attenuation data of lipid cores adjacent to other soft tissue that does not exclude contrast. Previous studies have shown enhanced contrast of lipid cores in contrast enhanced carotid scans using iodine with CT [68] and gadolinium with MRI [140]. However, the differentiation of lipid-rich regions from other soft tissue components is still problematic, especially with smaller sized lipid cores or smaller vessels such as coronary arteries [68, 141]. Furthermore, attenuation increases are seen in lipid cores in MRI between noncontrast and Gd enhanced scans [142], so contrast most likely does enter the lipid core. With the MARS scanner, the smaller voxel size and the MD resulting from multiple energy bins should allow more reliable identification of lipid cores even if the attenuation is altered by the penetration of contrast. However, this will require the development of new reconstruction and MD procedures that can provide a high Z component and a lipid component in the same voxel (currently only water is allowed as a second material), which the MARS team are currently working on.

In Figure 4.9 (b), the plaque is submerged in 6 mg Gd/ml, but the plaque outline is made visible in the MD by windowing the Gd component so that only concentrations below 3 mg Gd/ml are shown. This demonstrates the diverse benefits that quantitative material identification may have. By using concentration-based windowing in the material reconstructions, different aspects of anatomy can be highlighted at different concentration zones.

The potential for quantitative contrast measurements in improving spatial contrast have been demonstrated in human abdominal scans by Pourmorteza et al. [143]. They compared iodine enhanced scans with a traditional energy integrating detector and with a two energy bin photon counting detector. Using the summed count data for both energy bins in the photon counting detector to make a single reconstruction, they compared the attenuation data and found no differences in image quality, noise, artefacts, Hounsfield units (except in the spinal canal where the energy integrating system had beam hardening that lead to higher HU

values), noise power spectrum or spatial resolution. However, when they used the two energy bins to make an iodine concentration map, they found the contrast to noise ratio between the kidney and paraspinal muscle was 32% greater for the concentration map over the energy integrating reconstruction.

Concentration gradients in iodine or gadolinium staining of animal organs or whole bodies is well established in CT based morphology studies and Silva et al. [144] have demonstrated the use of dual-energy micro-CT to add quantitative contrast measurements to the detailed reconstructions. MARS scanners have demonstrated the same potential and add the possibility of using multiple contrasts simultaneously.

Concentration gradients may also improve injury or disease assessment if contrast agents have different diffusion or adhesion properties in healthy versus damaged or altered tissues. Abraham et al. showed that iodine contrast enhancement of damaged myocardium over normal myocardium was due to loss of membrane integrity in damaged cells, allowing diffusion of contrast agent into the damaged cells [127]. Possibly, gradients in iodine concentration measured by spectral CT could be used to assess the extent of damage to myocardium after heart attacks. Recent reviews by Sun [145] and Michel et al. [146] discuss the possible role of vasa vasorum in the development and progression of atherosclerotic p1aques. Contrast enhancement of both ultrasound and MRI have been useful in assessing neovascularization and intraplaque haemorrhage of plaque tissue, largely due to the more leaky, less mature nature of these vessels that grow into the thickening plaque wall. Again, contrast enhanced spectral imaging with MARS scanners may allow CT assessment of neovascularization through concentration gradients of contrast.

The misidentification of gadolinium as calcification is 21% at 1 mg Gd/ml and 9% at 2 mg Gd/ml (Figure 4.7). This error necessitated the raising of the calcium window lower threshold in Figure 4.9 (d) to 25 mg HA/ml to exclude (presumably) erroneous Ca voxels in the surrounding solution. This indicates that measures of intrinsic Ca may be less reliable in Gd enhanced scans. Similar misidentification in the opposite direction is not seen in the HA 50 phantom, but lower concentrations of HA should be included in future phantoms to assess the MD at lower Ca concentrations that may represent microcalcifications (see Section 3.4).

Several factors limit the scope of interpretations from this work. The excised plaque has been frozen and thawed which may change the potential diffusion of contrast into the tissue. Furthermore, the plaque segment is not under normal hydraulic stresses associated with an artery *in vivo* and does not include the entire artery wall which also may affect contrast diffusion. As with the intrinsic material scans of Chapter 3, iron is not included in the MD. Lastly, results were not checked against alternative methods such as histology, although Chapter 3 provides evidence that the lipid core and spotty calcifications are reliable measurements in the air scan.

The results presented provide strong initial evidence that spectral CT with MARS can produce high resolution quantitative material reconstructions of lipid, calcium and gadolinium contrast components. This may translate to human imaging that reveals several

markers of atherosclerotic plaque including the lipid core, spotty calcifications and any plaque traits such as leaky neovascularization that could be revealed by concentration gradients of contrast.

4.5 Mouse cancer model: measuring gold nanoparticles in implanted tumours

Introduction

Aim

Cancers are frequently characterized by abnormal neovascular growth into the tumour [80, 147, 148]. The resulting larger vessels and capillaries are termed ‘leaky’ due to fenestrae and gaps in the endothelium that are much larger, on the order of micrometers [149], than in normal capillaries where particles over about 8 nm cannot easily exit [150]. This trait can be exploited through the passive accumulation of particles, which can be contrast agents or treatments or both, over 8 nm from the bloodstream into tumours via the enhanced permeability and retention effect (EPR) [33, 135, 151, 152]. Nanoparticles utilizing the EPR effect to concentrate in cancerous tumours have already been approved for clinical use and many are in testing phases [153].

This study sought to image and quantify the passive accumulation of intravenously injected 15 nm gold nanoparticles in subcutaneous Lewis Lung carcinoma tumours in live mice. Aluminium filtration of 3.8 mm reduced low energy photons to demonstrate gold identification using photons energies similar to human scanning. While utilizing the EPR effect can involve active manipulations of tumour and animal physiology [152], this preliminary study is completely passive and relies only on the interaction of the 15 nm gold nanoparticles with the tumour vasculature.

Significance

Several MARS team members and collaborators are attempting to produce gold nanoparticles that target cancers for the purposes of tumour identification, drug delivery and monitoring of tumour progression or regression after treatment. This study demonstrates that gold nanoparticles accumulated in a tumour can be viewed in detail and that MARS MD allows the quantification of gold in the tumour and other organs. This will enable researchers to estimate efficiency in contrast uptake by the targeted region as well as delivery of any drugs loaded onto the nanoparticles. It will also allow measurements of tumour dimensions and changes over time. Furthermore, the temporal fate of nanoparticles in tumours and various organs could be monitored for short- and long-term toxicity studies [134, 154–156].

Publication

A manuscript is in preparation for submission to Radiology in 2018

Contribution

I was primarily responsible for the experimental design. I prepared the purchased nanoparticles for injection and performed all mouse manipulations. I participated in data collection and assessment. I am involved in document editing for journal submission.

Methods

Work was conducted under AEC protocol C04/14. Two C57BL mice were implanted subcutaneously with Lewis Lung carcinoma (LL/2) cells while under anaesthesia at 8-10 weeks of age. 13 days later, tumours were ~75 mm3 for mouse #1 and ~87.5 mm3 for mouse #2. On that day, they were injected using a 31 gauge needle via tail vein, under isoflurane anaesthesia, with 20 mg Au as 200 µl of 100 mg Au/ml solution. Gold nanoparticles were Aurovist^{TM} – 15 nm Gold Nanoparticle X-ray Contrast Agent (Nanoprobes, Inc., Yaphank, NY, USA) suspended in buffered saline solution. Mice were euthanized at 24 hours after injection to allow accumulation in the tumour and a decrease in vascular concentration (~15 hour blood half-life) [157].

Euthanized mice were X-rayed to assess gold accumulation in the tumour, placed in polypropylene tubes for scanning and refrigerated for twelve hours to allow rigor mortis to set in. Mice were scanned at room temperature according to the tumour mouse protocol in Table 4.1. A phantom for material calibration was scanned first, on the same day. The phantom consisted of Aurovist^{TM} 15 nm gold nanoparticles in saline at 20, 10, 8, 6, 4, 2 and 1 mg Au/ml, hydroxyapatite in resin rods (QRM GmbH, Moehrendorf, Germany) at 1200, 800 and 200 mg HA/ml, lipid and water.

The MARS Vision software was used to quantify the gold present in the tumour as well as the renal blood pool of the kidneys. Because of poor results for the 4, 2 and 1 mg Au/ml phantoms a lower threshold of 4 mg Au/ml was used for all imaging and measurements. This means that all gold quantification is most-likely underestimated due to exclusion of regions of lower concentration.

Results

Gold concentrated in the tumour and is apparent in the MD (Figure 4.10). Gold, lipid and calcium components were separated allowing for measurements of gold quantities in various regions of interest, including the tumour and kidneys. All images and measurements include only gold over 4 mg Au/ml as explained in the methods.

The measured concentration of gold in the phantoms in mg Au/ml were 8 ± 2, 10 ± 1 and 20 ± 1 for the 8, 10 and 20 mg Au/ml phantoms respectively. This indicates the reliability of measurements of higher concentrations of gold in the mouse scans. Furthermore, ~100% of voxels in the 6, 8, 10 and 20 mg Au/ml phantoms were correctly identified as gold. For 4, 2 and 1 mg Au/ml identification was below 30% which prompted the 4 mg Au/ml threshold in data analysis.

Measurements of gold in the mice were as follows. Mouse #1 had 0.497 mg Au in the tumour, 0.481 mg Au in the right kidney and 0.374 mg Au in the left kidney. Mouse #2 had 0.281 mg Au in the tumour, 0.147 mg Au in the right kidney and 0.414 mg Au in the left kidney.

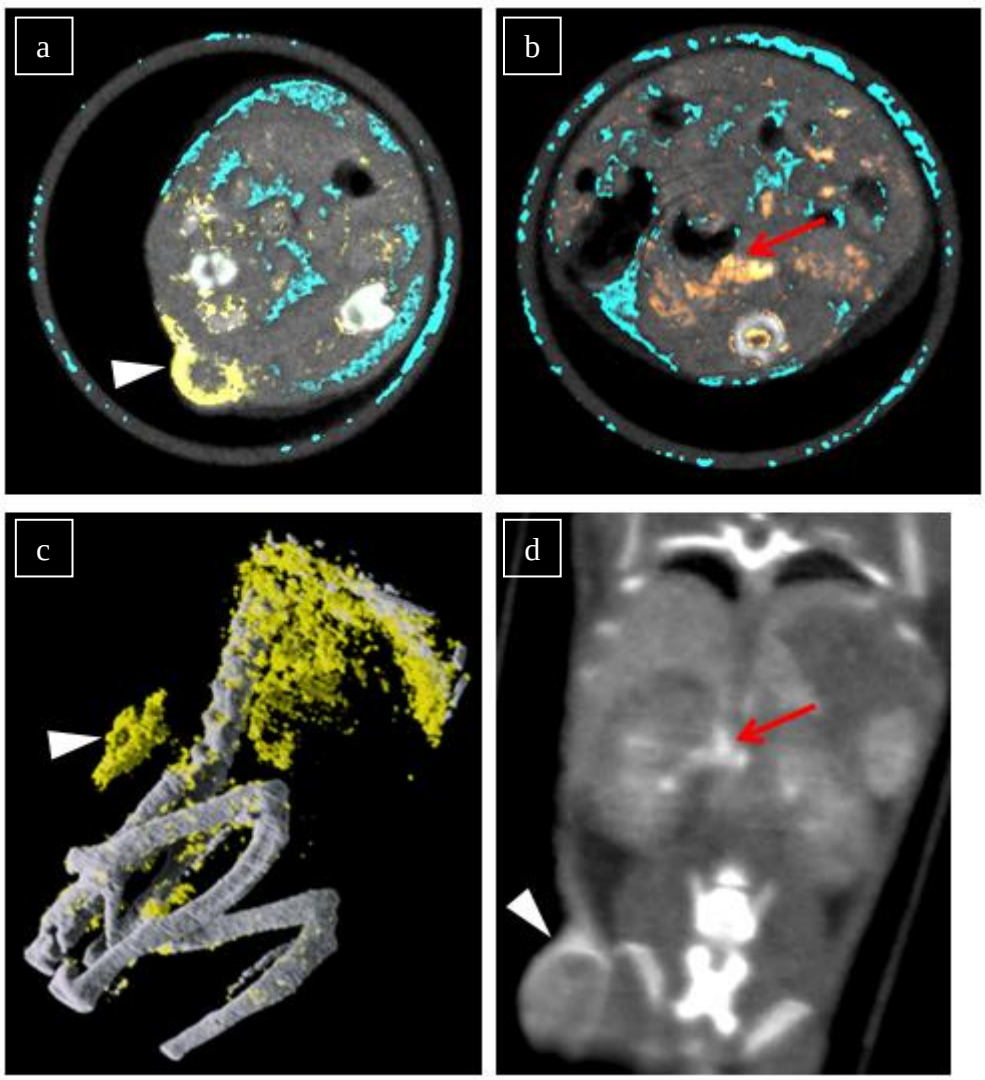

Figure 4.10: Gold nanoparticle accumulation in a tumour for mouse #1. 15 nm gold nanoparticles are clearly visible in the periphery of a Lewis Lung carcinoma (LL/2) tumour implanted in a C57BL mouse (white arrowhead in a, c and d) and in larger blood vessels (red arrow in b and d). Panels a and b are an MD overlay onto transverse slices of the attenuation reconstruction. Panel c is a 3D image of the calcium and gold components of the MD. Panel d is a coronal slice reconstruction through the tumour. For the MD, gold = yellow, grey = calcium, blue = lipid. The liver, kidneys and spleen are also discernible in d. Images used with permission [158]

Discussion

At concentrations over 4 mg Au/ml, gold was successfully differentiated from bone (calcium) and lipid in the MD (Figure 4.10) and identified within the tumour. Furthermore, the concentrations in the phantom MD were very accurate. These two results indicate that quantification of gold contrast used in medical and research procedures may be possible using spectral CT with the MARS scanner.

The differentiation of bone and gold means that gold could be used in detection of disease or injury in bony regions. Tumours in bones may be identifiable and their shape elucidated with a noninvasive technique. Furthermore, the calcifications associated with some cancerous tumours (see Section 2.9) may be discernible even in a gold targeted tumour scan. Zhang et al. developed a targeted gold nanoparticle for damaged bone tissue and MARS scanners might be able to measure this nanoparticle *in vivo* [159].

The results were not confirmed with other techniques but the samples are preserved and that measurement may be possible in the future or in future experiments. Confirmation of MD measurements with other techniques will be an important step for the integration of spectral CT material reconstructions into research and clinical practice.

Gold concentrations can be determined with CT, as shown by Hainfeld et al. [160] using micro-CT for a breast cancer mouse model, but this technique is not suitable for live imaging. Furthermore, the measurement depends on subtracting the signal of a known background tissue and therefore the measurement would be affected by other anomalies common in some cancers, such as calcifications. The ability of MARS material imaging to distinguish intrinsic materials from high-Z contrasts and to, in the future, image live animals could make contrast quantification with spectral x-ray CT a reality [138, 139, 161].

A 15 nm particle should not be filtered by the kidneys and the bladder was not highlighted by gold accumulation. Therefore, the measured gold in the kidneys is most likely in the blood pool. The injected quantity of 20 mg of gold is quite large, meaning at injection the concentration of gold in the blood would be approximately 10 mg Au/ml, assuming a ~2 ml blood volume which is conservatively large [162].

Gold was identified in the vasculature and various organs. Thus, whole body scans would allow quantitative assessment of the distribution of gold in test subjects. This measurement would be important in trials of any clinical or research contrast agent. As stated in the significance section for this study, viewing and quantifying the whole body distribution of any contrast agent has value in assessing targeting efficiency and the temporal fate of contrast agents for toxicity analysis. For example, while some studies indicate that gold formulations have low toxicity in the short term [154, 163], long term studies show that gold can persist in some organs, especially the liver. Sadauskas et al. [134] found that 40 nm gold nanoparticles injected intravenously into mice accumulated in the Kupffer cells of the liver and persisted for the six months of the study while slowly aggregating into fewer and fewer total cells. MARS spectral CT might prove useful in studying the long-term distribution of gold in studies like this and results could be correlated with animal health responses.

The poor results at gold concentrations of 4 mg Au/ml and below indicate that quantification of total gold content would be underestimated. Gold identification was much better in the phantom experiment described in Section 4.3, but that study had less aluminium filtration and different energy thresholds for the charge summing counters which could partially explain the better result. MARS developers continue to improve machine and software performance to address poor detection at lower concentrations.

This study demonstrates the ability to quantify 15 nm gold nanoparticle accumulation in a tumour via the EPR effect. When live animal scanning is feasible in MARS scanners in the future, longitudinal studies may be possible that include assessment of gold distributions, from single or repeated applications, and thus measurements of and correlations with treatment and disease progression or regression.

4.6 Multi-contrast mouse: simultaneous MD of three high-Z contrast agents in a sample

Introduction

Aim

This study sought to extend multi-contrast identification from the phantom studies of Sections 4.2 and 4.3 into a biological sample. Iodine, gadolinium and gold were administered internally to a mouse so that each would dominate a different region in the body. MD of the scans included all three contrasts plus lipid, water and calcium components. The scan was performed using 0.375 mm of brass to again eliminate photons below ~30 keV and simulate a scan relevant to human imaging.

By imaging three contrasts in a biologic system, this feasibility study also sought to highlight the kinds of images and analyses attainable with the MARS vision software. Thus, the results presented largely show various capabilities of the visualization system.

Significance

The rapid development of nanotechnologies and their potential uses in medical imaging and treatments represent a natural fit for the development of spectral CT and material reconstruction described in this thesis (see Chapter 2). The ability to target contrasts (possibly with treatment capabilities) to very specific sites in the body with attached antibodies [34, 42, 88, 160, 164] or ligands [41, 165] lends itself to the idea of using multiple targets in one scan. By demonstrating the simultaneous separation of three high-Z contrast agents along with intrinsic high lipid and high calcium regions in a biologic sample while using only photons above 27 keV, this study helps illustrate the parallel progression in material imaging that will help maximize the information available from ongoing advances in contrast agents.

The scan was performed using cadmium/zinc/tellurium (CZT) as the sensor layer in the camera. This study demonstrates the feasibility of CZT as a sensor layer for high energy spectral CT scanning.

Publication

A manuscript is in preparation for submission to Radiology in 2018

Contribution

I was primarily responsible for the experimental design. I prepared all contrast agent dilutions and performed the tail vein injections. I participated in protocol development for the scanner. I was involved in data analysis. I am involved in document preparation for journal submission.

Methods

The administration strategy to attain high contrast concentrations in separate regions of the mouse was as follows. Intravascularly injected commercial iodine contrast agent would concentrate in the kidneys and then the bladder for about 20 minutes while simultaneously depleting in the blood vessels [166]. Gold nanoparticles of 15 nm would remain in the vasculature since the kidneys do not filter particles of this size and the mouse would be euthanized before significant filtration by the liver and spleen. Gadolinium would be isolated to the digestive tract by gavage.

Work was conducted under AEC protocol C19/13. Three C57BL mice were prepared for scanning. The mice were brought to a nonresponsive state assessed via toe pinch using isoflurane anaesthesia. Mice were then injected with 16 mg of iodine in the form of 100 µL of iodixanol (Visipaque 270 (Ge Healthcare, Princeton, USA)) diluted to 160 mg I/ml. Iodine was allowed to concentrate in the bladder and kidneys while simultaneously reducing in the blood stream for 15 minutes. At this point, 16 mg of 15 nm Aurovist^{TM} (Nanoprobes, Inc., Yaphank, NY, USA) was injected as 150 µL of 107 mg Au/ml. The mice then received 0.4 ml of gadobutrol (Gadovist, (Bayer AG, Leverkusen, Germany)) diluted to 8 mg Gd/ml by oral gavage. Immediately after oral gavage, mice were euthanized by CO_2 at roughly 21 minutes post iodine injection. An additional 0.4 ml of the same Gd solution was then administered by rectal gavage. Quantities of contrast agents were chosen to achieve expected concentrations in the intended regions of the mouse that would give high identification accuracy, based on previous phantom studies.

Mice were placed in a polypropylene tube (Figure 4.11) and allowed to sit in a refrigerator for ~12 hours to allow rigor mortis to set. Mice were then scanned at room temperature following the protocol in Table 4.1 for multi-contrast mouse. A 0.375 mm brass filter was used to eliminate low energy photons (< ~ 30 keV) and simulate a human scan.

The phantom scan was performed just prior to mouse scanning using the same protocol. The phantom consisted of a 38 mm polymethyl methacrylate cylinder drilled to hold 12 phantom vials. The calibration materials were Au nanoparticles at 8, 4 and 2 mg Au/ml, Gd at 8 and 2

mg Gd/ml, iodine at 18, 9 and 4.5 mg I/ml, hydroxyapatite nanoparticles in resin at 800 and 200 mg HA/ml, lipid and water.

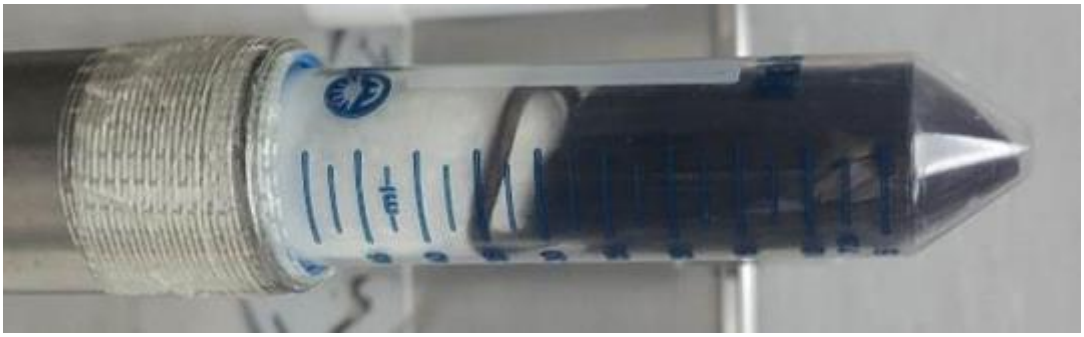

Figure 4.11: The euthanized mouse with three contrast agents was placed in a polypropylene tube for scanning. Used with permission [158]

MARS reconstruction software was used to generate attenuation based reconstructions for each energy bin which were then used to generate the MD with six components: lipid, water, calcium, iodine, gadolinium and gold. MARS vision software was used to generate all images.

Results

The material calibration phantom results are shown in Figure 4.12 as attenuation of each material versus energy bin. The k-edges for each high-Z contrast are clearly visible as a rise in attenuation from the below k-edge bin to the above k-edge bin. However, gold and hydroxyapatite show a rise in attenuation with increasing energy between the 27-36 keV bin and the 36-52 keV bin which does not match physical expectations.

The identification chart for the phantom is displayed in Figure 4.13. For the highest concentrations of each contrast agent identification was 90% for iodine, 100% for gadolinium, and 82% for gold. Hydroxyapatite is correctly identified in 98% and 93% of voxels for 800 and 200 mg HA/ml, respectively. For 2 mg Gd/ml, identification is still better than 80%, but at lower concentrations of iodine and gold considerable cross talk occurs. These results illustrate our reasoning to achieve concentrations in the mouse of near 8 mg Gd/ml and near 8 mg Au/ml (after dilution in the blood assuming ~2 ml or less of blood volume). The commercial iodine concentrates in the kidneys and bladder so its initial concentration was less critical.

Various instructive images of the mouse material decomposition are shown in Figures 4.14, 4.15 and 4.16. The three contrast materials are visible in three separate regions of the mouse while also being separated from the bones in the material images. Figure 4.14 demonstrates the anatomical visualization of various structures. The digestive tract is seen with gadolinium (green), especially the descending colon, the kidneys and bladder are clear in the iodine component (red) and the lungs, which have collapsed, and jugular veins are seen in the gold component (yellow).

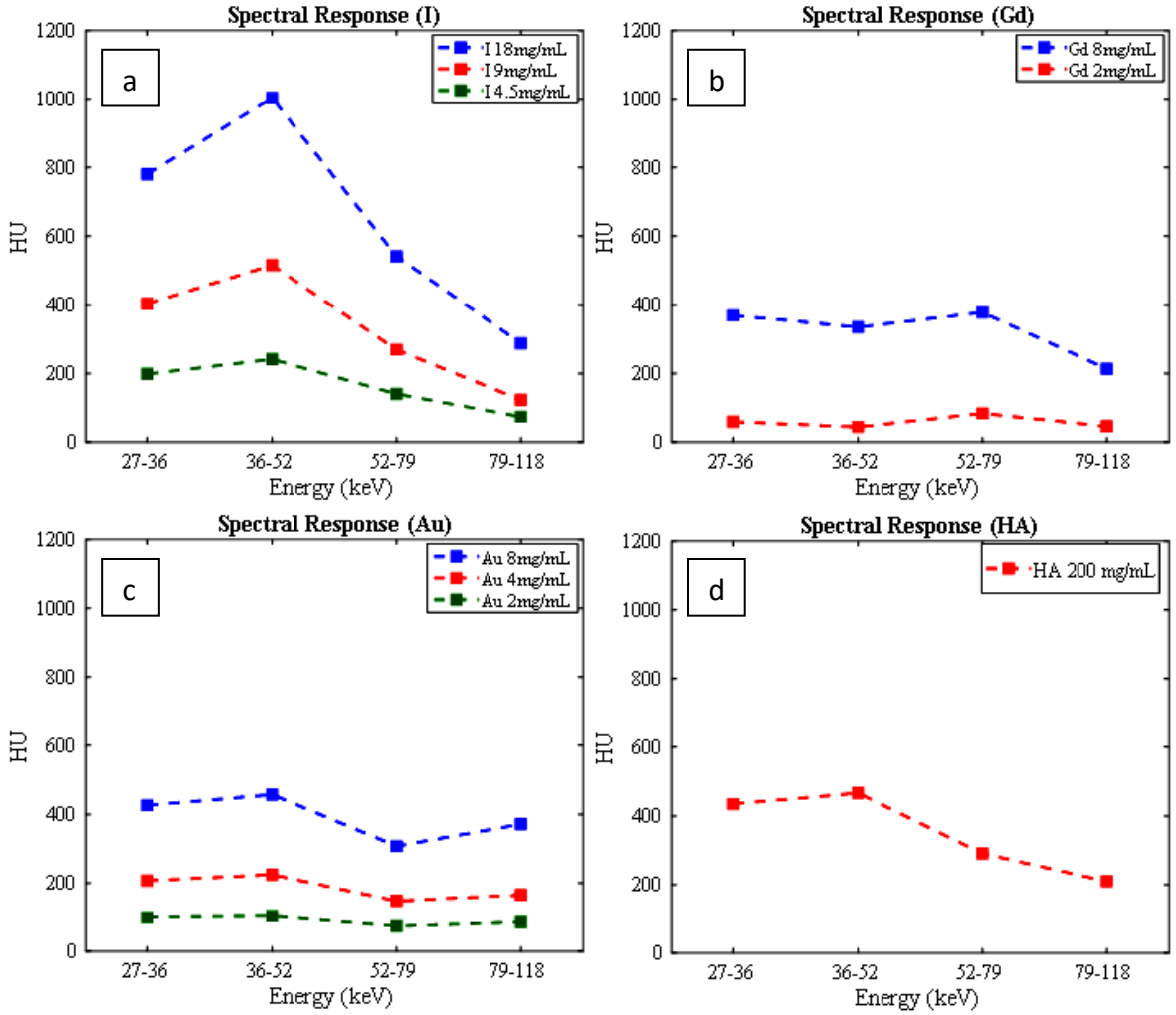

Figure 4.12: Attenuation (HU) versus energy bin for the calibration phantom. The K-edges of (a) iodine (33.2 keV), (b) gadolinium (50.2 keV) and (c) gold (80.7 keV) are all detected even at the lowest concentration. Panel (d) shows the spectral pattern for HA. The inappropriate rise in attenuation between the 27-36 keV bin and the 36-52 keV bin for gold and HA may contribute to the MD crosstalk seen in Figure 4.12. Used with permission [158]

Figure 4.15 demonstrates the potential for different windowing levels in the material reconstructions. The large intestine is seen in differing detail depending on where the lower threshold is set for gadolinium visualization.

Each component is a separate data set so bits of one material can be removed from images without affecting the visualization of other materials. In Figure 4.16, some of the bone has been removed to allow an unobstructed view of the gold component in the lungs and jugular veins while maintaining the overall anatomical perspective.

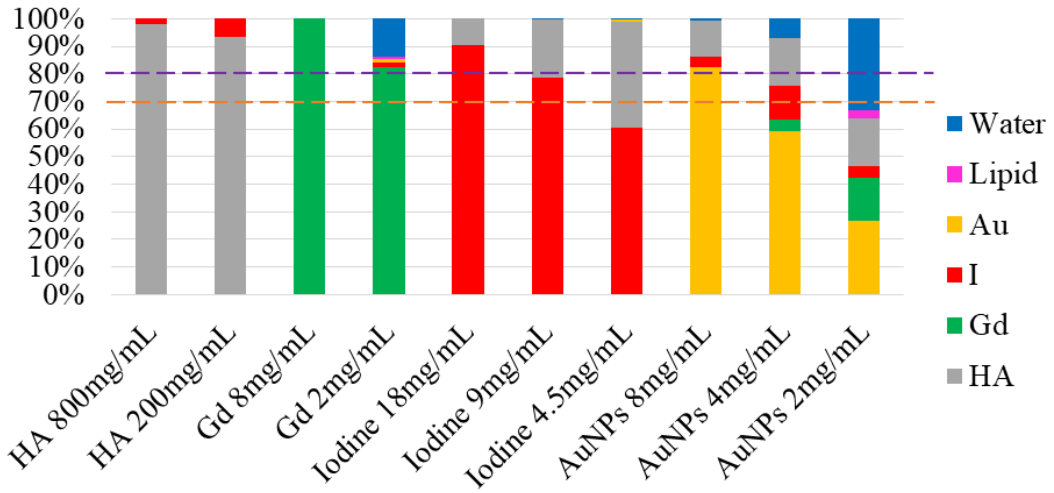

Figure 4.13: Identification chart for the six material calibration phantom. The bar labels name which calibration vial is analysed while the colours represent what percentage of the vial was identified as the material listed in the colour legend. Since all voxels have a water value, the water percentage is only voxels that have a concentration of zero for the other materials. Alternatively, a lipid voxel is any voxel with a lipid concentration above zero. Used with permission [158]

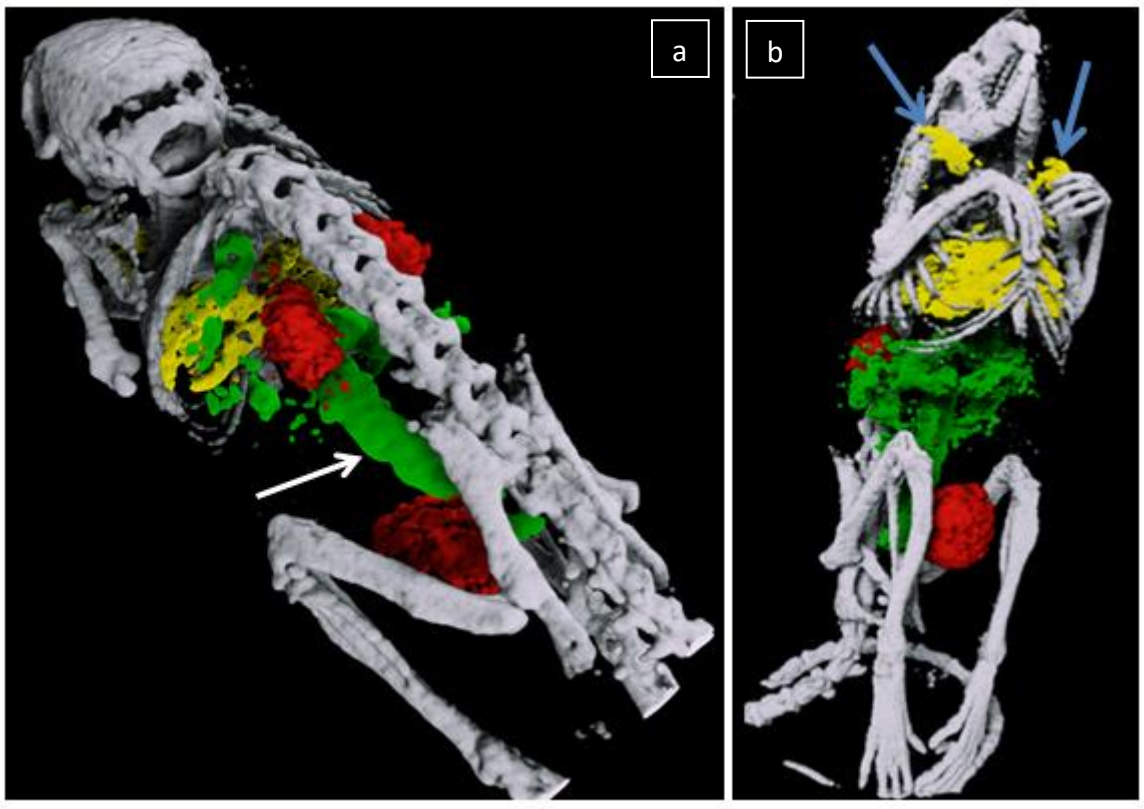

Figure 4.14: MD showing bone and three contrast materials in a mouse. Bones (gray) are distinguished from: iodine (red) in the bladder and kidneys, gadolinium (green) in the digestive tract, including the descending colon (white arrow in a) and gold (yellow) in the collapsed lungs and the jugular veins (blue arrows in b). Used with permission [158]

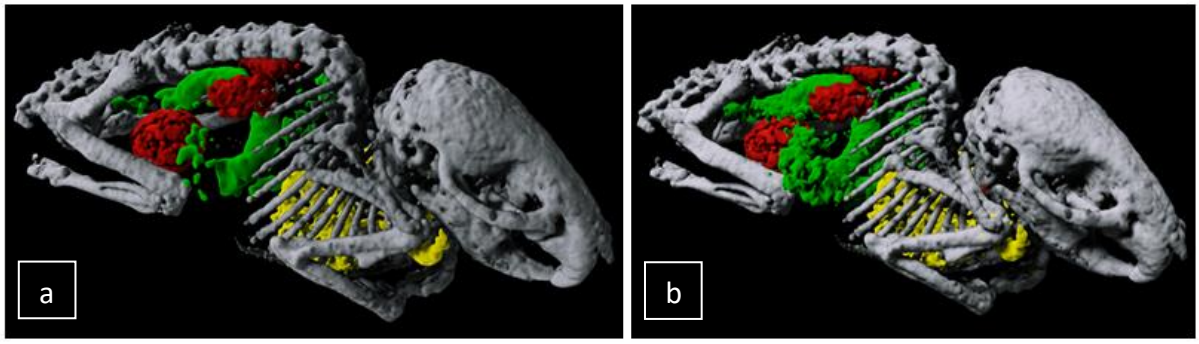

Figure 4.15: Windowing MD components allows differing examinations of the same region. The Gd (green) window in (a) is > 4 mg Gd/ml while the Gd window in (b) is > 1.5 mg Gd/ml. Used with permission [158]

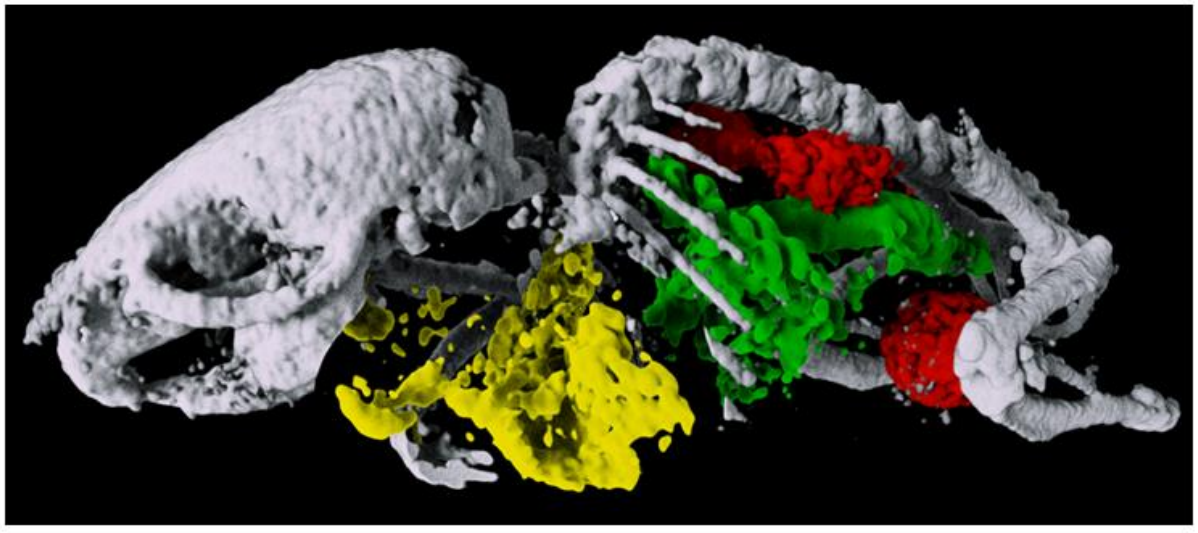

Figure 4.16: Partial bone removal allows examination of the gold MD while maintaining the overall anatomic view. Used with permission [158]

Discussion

Iodine, gadolinium, gold, bone (calcium), lipid and water components were discriminated simultaneously in a single scan using the MARS spectral CT scanner. By creating easily identified regions of known high concentration for each material, the qualitative results could be confidently interpreted without the need for chemical or histological procedures. This feasibility study confirms the potential for quantifying multiple contrasts in a single scan at higher photon energies (> 27 keV), while maintaining material identification of intrinsic materials of interest. The results presented highlight the contrast agents in relation to bone, so lipid and water components are not presented or discussed.

While the K-edges of each high-Z contrast is apparent at all concentrations in Figure 4.12, the gold and HA patterns show a physically unexpected rise in attenuation between the 27-36

keV and 36-52 keV bins. This may contribute to the crosstalk with the iodine component seen in the identification chart (Figure 4.13). The crosstalk between iodine and HA at lower concentrations is not problematic in this feasibility study due to the high concentrations attained in the kidneys and bladder for iodine and the high concentration of HA in bone; however, in studies requiring sensitivity to lower concentrations of either material, such as the imaging of calcified plaques described in Chapter 3 and Section 4.4, this misidentification could prevent confident interpretation of results. Thus, the appropriate uses of spectral CT will depend on an understanding of the sensitivity and specificity of material identification at different concentrations and in different scenarios. Continuing refinement of hardware, software and techniques should continue to expand what is possible.

Any study with multiple but varied targets or physiologic processes that could create different arrangements of contrasts might benefit from simultaneous measurement of multiple contrasts. Symons et al. [167] have shown the potential for using spectral CT in split-bolus dual-contrast multiphase kidney imaging in a canine model. By injecting commercial based gadolinium contrast followed three minutes later by iodine contrast they generated quantitative images that showed high renal cortex concentrations of iodine compared to high renal medulla concentrations of gadolinium. This study also included a bismuth contrast in the digestive tract to demonstrate three contrast separation. Cormode et al. [168] used a rabbit to show vascular and renal enhancement by gold and iodine, respectively, using a strategy similar to this study. Both of these spectral CT studies were performed on modified human scanners.

This study also sought to demonstrate some of what is possible, visually, with the MARS vision software. Figure 4.14 presents the whole mouse body from two angles and clearly visualizes the lungs and jugular veins in yellow for gold, the digestive tract in green for gadolinium and the kidneys and bladder in red for iodine all within the bone framework in grey. MARS software allows 3D imaging and rotation of the subject to view from any angle. In Figure 4.15, the potential for changing the view by altering material concentration threshold is demonstrated. By simply altering the lower threshold for gadolinium, the large intestine view is altered. This might allow details to be examined based on concentration gradients as discussed in Section 4.4. The components of the MD are separate datasets so they can be imaged alone (see Figure 4.9 (c) and (d)) or in composite. Figure 4.16 shows how a composite image can be altered by removing part of one component (in this case, the calcium) to view other components more clearly, while maintaining the overall anatomic reference.

The successful material decomposition of three contrast agents from bone in a single scan of a mouse demonstrates the potential of spectral CT for multicontrast imaging in clinical research. Upscaling to human imaging with MARS cameras is expected to be simple from a detector and data point of view because the camera and source will be the same. The first MARS human scanner prototype is constructed and will undergo testing in 2018 using cameras with larger chip arrays.

4.7 Macrophage uptake of gold nanoparticles

Introduction

Aim

Cultured human monocyte derived macrophages were incubated with two different concentrations of non-targeted gold nanoparticles both of which were below the measured sensitivity of the MARS scanner. The study sought to test if macrophages would concentrate the gold to levels detectable by MARS material reconstruction. This was a feasibility experiment to justify further exploration with macrophage targeted nanoparticles for atherosclerosis detection (though, of course, the macrophages could be associated with other disease or injury states).

Significance

With respect to atherosclerosis, concentrated macrophages associated with inflammation in plaques are considered a biomarker of advanced and vulnerable plaque [169]. This study was undertaken as an initial test of gold nanoparticle uptake by the macrophage cultures created in the Free Radical Biochemistry lab at the University of Canterbury. These cultured macrophages will be used in initial experiments aimed at creating gold nanoparticles specifically targeted to macrophages that could be used in detection of atherosclerotic plaque using spectral CT. It is important to establish if macrophages will concentrate contrast above the surrounding concentration to levels detectable by MARS scanners at this time.

Contribution

I am the primary experimental designer. I performed all the scans and image processing.

Methods

Gold nanoparticles with a proprietary coating for solubility and biocompatibility were prepared at 18 nm mean diameter and concentrated to 1000 µg Au/ml.

Human monocyte derived macrophage culture is performed under human ethics approval reference number CTY/98/07/069/AM05. Macrophages were cultured and classically activated to a pro-inflammatory phenotype following the labs standard procedure [170]. Macrophages were cultured at roughly 2 million cells per well in a 48 well cell culture plate where they are adherent to the well walls. The culture media was removed and replaced by 1 ml of fresh media plus gold nanoparticles in three treatments. Three wells were a control with no gold and received an extra 125 µl of media. Six wells received 125 µl of the 1000 µg Au/ml stock for a total addition of 125 µg of Au. Three wells received 42 µg of Au total by diluting the stock to 333 µg Au/ml with culture media and adding 125 µl. The accepted detection limit for gold in the MARS scanners at this time was 1 mg Au/ml or higher.

Two wells with 125 µg of Au added were harvested at 15, 44 and 77 hours after addition. One well of 42 µg Au added was harvested at 30 hours and two wells at 62 hours. Cell

cultures were photographed just prior to harvesting. Cells were suspended, removed by pipette, and rinsed twice with PBS by centrifuging and resuspending. Cells were then centrifuged at 1000 g for 5 minutes to a pellet. The PBS was removed by pipette and liquid agar was pipetted over the pellet to cause minimal disturbance and allowed to solidify.

Pelleted cells were then scanned according to the protocol in Table 4.1. The material calibration phantoms were included with the scan. The phantom included lipid, water, gold nanoparticles at 8, 4, and 2 mg Au/ml and gold chloride ($AuCl_3$) at 8 mg Au/ml. The 30 hour pellet for 42 µg Au added was destroyed during agar addition and so was unscannable. The supernatant from the 77 hour well was scanned to confirm that its concentration was below detectable limits.

Results

Macrophages did take up the gold nanoparticles as seen in Figure 4.17. Most cells were still alive by visual inspection at the 77 hour endpoint for the control and 125 µg Au treatment and the 62 hour endpoint for the 42 µg treatment. Gold accumulation is seen as a dark purple to black colour in the cells. Some macrophages did not take up any gold (by visual inspection). The reddish colour of the nanoparticle solutions changed to a dark purple after a few hours of incubation with the macrophages, probably due to clumping as a result of an interaction with proteins in the culture media, though this was not confirmed. Other researchers have solved this problem at this time but those results were achieved without my input and are not shown here other than to mention their success.

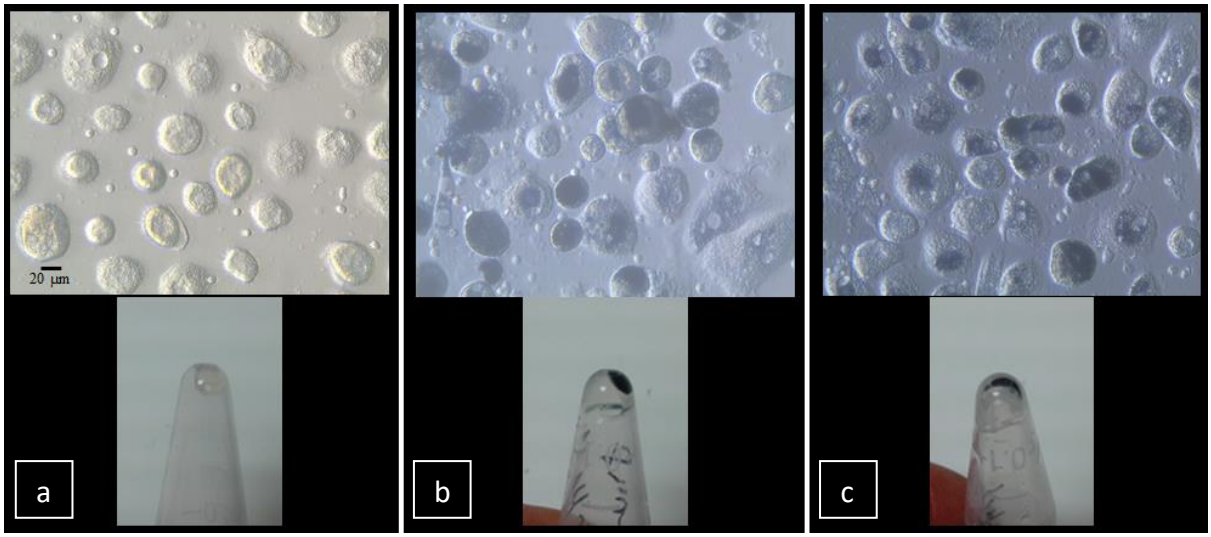

Figure 4.17: Photographs of macrophages incubated with gold nanoparticles. Macrophages and the corresponding cell pellet after centrifugation after incubation with (a) no AuNPs for 77 hours, (b) 125 µg AuNPs / ~2 million cells for 77 hours and (c) 42 µg AuNPs / ~2million cells for 62 hours. AuNP accumulation in cells appears as an obvious black/dark purple colour.

Gold was concentrated in the macrophages to levels detectable by MARS material reconstruction for all vials scanned (excluding the 15 hour time point for 125 µg Au which was missed in the scan). Figure 4.18 shows the MD with gold, gadolinium, iodine, calcium and water components. There was nearly perfect identification of gold in all cases with very few gadolinium, iodine or calcium voxels in the entire volume.

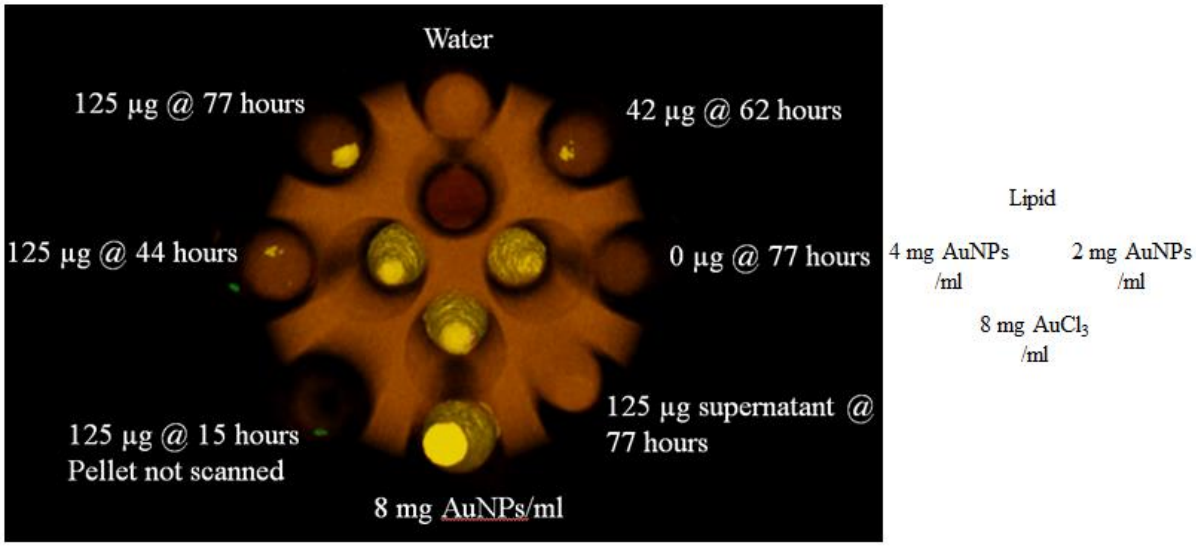

Figure 4.18: Volumetric image of the MD of the macrophage cell pellets after incubation with gold. The labels on the right are the interior four vials in the MD image. Gold is yellow and water-like is red. The water opacity is set low to maximize gold imaging. The pellet for 125 µg AuNPs for 15 hours was missed in the scan, but because of the preliminary nature of this study, rescanning was not deemed necessary. Gadolinium, iodine and calcium components are include but there was very little cross talk to these components that were not present in the sample.

Discussion

This preliminary feasibility study showed that macrophages will concentrate gold nanoparticles from levels below those detectable by MARS scanning to levels that can be distinguished as gold in MARS material reconstructions. At the time of this study, the accepted minimum detection concentration for gold in a brass filtered scan on a MARS system equipped with CZT was > 1 mg Au/ml. The detection of gold in macrophages incubated with 42 µg of gold in just over 1 ml of media means that macrophages concentrated gold by over 20 times (from < 0.042 mg Au/ml to at least 1 mg Au/ml). The control vial with 0 µg Au added showed no gold signal. The supernatant removed from the 77 hour well with 125 µg Au added did not show detected gold indicating that its concentration was below our detection limit and that the probable clumping did not create detectable clumps or settling. No settling of gold was seen at any time in any wells or supernatants.

The change of colour in the culture media, if it does represent clumping, throws doubt on the uptake of the actual 18 nm gold nanoparticles. However, the results of this study were encouraging and other researchers were able to change the culture media and show uptake of nanoparticles without the change in colour of the media (unpublished data).

Macrophages are present in almost all inflammation events and are considered a hallmark of the inflammation associated with vulnerable atherosclerotic plaque. Possibly, the degree and location of macrophage infiltration in plaque could be monitored noninvasively using targeted contrast agents and spectral CT. Cormode et al. [171] used spectral CT to visualize high density lipoprotein-like particles with a gold core in a mouse atherosclerosis model. Gold appeared near the aorta of the mice in the CT reconstruction and was confirmed to be present in plaque macrophages by microscopy. Imaging plaque macrophage burden might improve assessment of at risk patients or it might be used in time course research to gain better understanding of how macrophage populations change in plaques over time.

This study showed the possibility of using gold nanoparticles to image macrophages in our lab. The results have provided enough evidence for the continuation of targeting experiments with cultured macrophages and the hope of eventual experiments with a mouse atherosclerosis model.

4.8 Conclusions

Techniques for using MARS spectral CT and K-edge values to identify and quantify high-Z contrast agents in biologic systems were developed and demonstrated. The work concentrated on using photon energies up to ~120 keV to show relevance to scan requirements for larger objects and the K-edge of gold (80.7 keV). All studies utilized charge summing mode to correct for charge sharing in the hybrid detector.

A simple technique for choosing energy thresholds that optimize the outcome of material decomposition was developed. The simple, two-part ranking system was used to compare five possible threshold combinations for a three contrast scan including iodine, gadolinium and gold. The top two protocols were compared experimentally by scanning a multicontrast phantom. The protocol with the best rank proved to have the better overall performance in the scans.

A series of phantom and biologic sample scans demonstrated some of the possible uses for quantitative material reconstruction of contrast enhanced spectral CT scans. A second three contrast phantom study introduced the identification chart as a simple visual assessment of the quality of the MD across a range of material concentrations. The phantom results demonstrated the MD of six materials, including lipid, water, calcium and, again, three K-edge material, iodine, gadolinium and gold. For this protocol, gold was identified correctly in over 80% of voxels at 2 mg Au/ml while gadolinium identification was very good at 8 mg Gd/ml but had greater that 60% misidentification at 2 mg Gd/ml.

An excised carotid atherosclerotic plaque was scanned in air and then submerged in gadolinium contrast. The air scan indicated a lipid core and extensive spotty calcium around the perimeter, both of which were identifiable in the gadolinium scan as well. Gadolinium did not appear to extensively enter the high lipid regions of the plaque. The concentration gradient of Gd in the plaque's outer surfaces that resulted from two hours of diffusion allowed the plaque shape to be distinguished by windowing the Gd component to concentration below 3 mg Gd/ml. These results offer evidence that contrast enhanced human scans with MARS spectral CT might allow simultaneous assessment of carotid stenosis and important plaque traits such as the presence of a lipid core and spotty calcifications.

As part of a collaboration with cancer researchers, a mouse cancer model was used to demonstrate the passive accumulation over 24 hours of gold nanoparticles in a subcutaneous tumour via the EPR effect. The MD separated gold, calcium (bone), lipid and water components and allowed quantitative measures of the gold distribution in the body and tumour. MARS quantitative material images might be useful in cancer diagnosis, assessment of tumour characteristics such as size and neovascularization patterns, following the fate of nanoparticles throughout the body over time, noninvasively, and monitoring tumour progression/regression in response to treatments.

Three high-Z contrast agents were simultaneously differentiated from each other and bone in a mouse scan performed at 118 kVp and with filtration to eliminate photons below ~30 keV. This feasibility study shows the potential for identification and quantification of three contrasts in a biologic sample using the photon energies needed for human scanning. The study highlights the vast potential of the combination of spectral CT and the rapidly expanding field of targeted contrast agents.

Cultured human monocyte derived macrophages were shown to concentrate gold nanoparticles to detectable levels from a surrounding culture media that is below levels currently detectable with MARS spectral CT. In one vial, the concentrating effect was most likely, over 20 times. This feasibility study was performed in cooperation with researchers seeking various targeted contrast agent strategies including targeting macrophages resident in atherosclerotic plaques.

5 Machine and Data Assessment

5.1 Introduction

In any scientific endeavour, part of the researcher's responsibilities includes continual assessment of equipment and software performance. Machines must be properly set-up, calibrated, integrated, maintained and monitored. The MARS scanner and the imaging software that processes the raw data were both under constant developmental work during the timeframe of this thesis and so machine set-up and data assessment were a constant part of every student's role. All students working with MARS are expected to use the standardized quality assurance tests as part of their training. As these tests identify new issues with data quality, projects are outlined by the developers and students participate in finding solutions. The typical project involves several iterations by evolving groups of students as the problem is more clearly understood and the potential solutions are refined.

This chapter describes the more significant results of my work within the machine and data assessment role. A first generation pixel inhibition mask is described that is the predecessor of the more complex pixel masking software now installed on the commercial release of the MARS scanner. Important results of the commissioning regiment for two new scanners are described along with the resulting improvements in machine set-up and scanning protocols. Finally, a new graphing technique is described that identifies noise in the MD related to the partial volume effect.

5.2 Pixel masking

Introduction

Aim

Significant noise is introduced in the raw data due to faults or lack of homogeneity in the sensor crystals, the bonding of sensor to the Medipix chip and the electronics of the chip itself (see Chapter 2). Because of this, many pixels produce very poor data and it was determined that pixels should be inhibited (turned off) on the camera so that they would not produce data. This work defines the criteria by which faulty pixels should be identified, produces software to implement these criteria to form a pixel inhibition mask on the camera, produces a graphical user interface (GUI) to allow users to produce and assess the mask, and shows the impact of the mask on scan reconstructions of a biological sample.

Significance

This work established the four major criteria for defining faulty pixels that are used in the current pixel masking on the first commercial release of the MARS scanner. This initial

work only masked the camera by turning off pixels. The scans produced showed that pixel inhibition removed too much useful data and lead to the two step masking now in use that was developed by Muhammad Shamshad and Marzieh Anjomrouz.

Publication

Some of this work is presented in the Journal of Instrumentation [172]. The commercial release of the pixel masking software is described in the doctoral theses of Muhammad Shamshad and Marzieh Anjomrouz [1, 2].

Contribution

Ali Atharifard and I were co-investigators and contributed to all of the aspects of this work. The only portions where the contribution differ from 50/50 are in programming where Ali was primarily responsible for the coding of the data analysis and graphing program, while I was primarily responsible for the coding of the pixel mask algorithms into the MARS scanner control software and for the appearance of the pixel masking GUI (GUI coding was performed by Dr. Stephen Bell)

Methods

The logic for differentiating useful from faulty pixels is based on four simple concepts.

1. Pixels that count when there is no X-ray input are faulty
2. Pixels that do not count when there is an X-ray signal are faulty
3. Photon counting is expected to follow a Poisson distribution (the variance is equal to the mean of counts) over multiple measurements. Pixels that have a variance much greater than or less than the mean of counts are faulty.
4. Under the same signal, pixels should have the same mean after repeated measures. Pixels with a mean drastically different from the mean of the whole chip (after removal of the previous three groups of bad pixels) are faulty.

Software was written to apply tests related to each of the four types of faulty pixel to frames taken with the camera. The initial recommended criteria were arbitrary and refined by Shamshad and Anjomrouz. For the scans presented the masking criteria were:

Darkfield Mode: take 20 frames with the X-ray off. Any pixel with counts > 2 in any frame is inhibited.

Flatfield Mode: Take 1000 frames with the X-ray on.

Any pixel with mean counts < 3 is non-functional and is inhibited
Any pixel with a variance in counts > 3 times its mean is inhibited
The fourth criteria was not applied at this time.

A graphical user interface was developed that allowed users to choose which of the three available criteria to use, then review the created mask and choose to apply it to the camera or to run a new masking test (see Figure 5.1). The mask was displayed with each type of faulty

pixel colour-coded, red for pixels that counted in darkfield, blue for pixels that did not count in flatfield and green for pixels that failed the variance test.

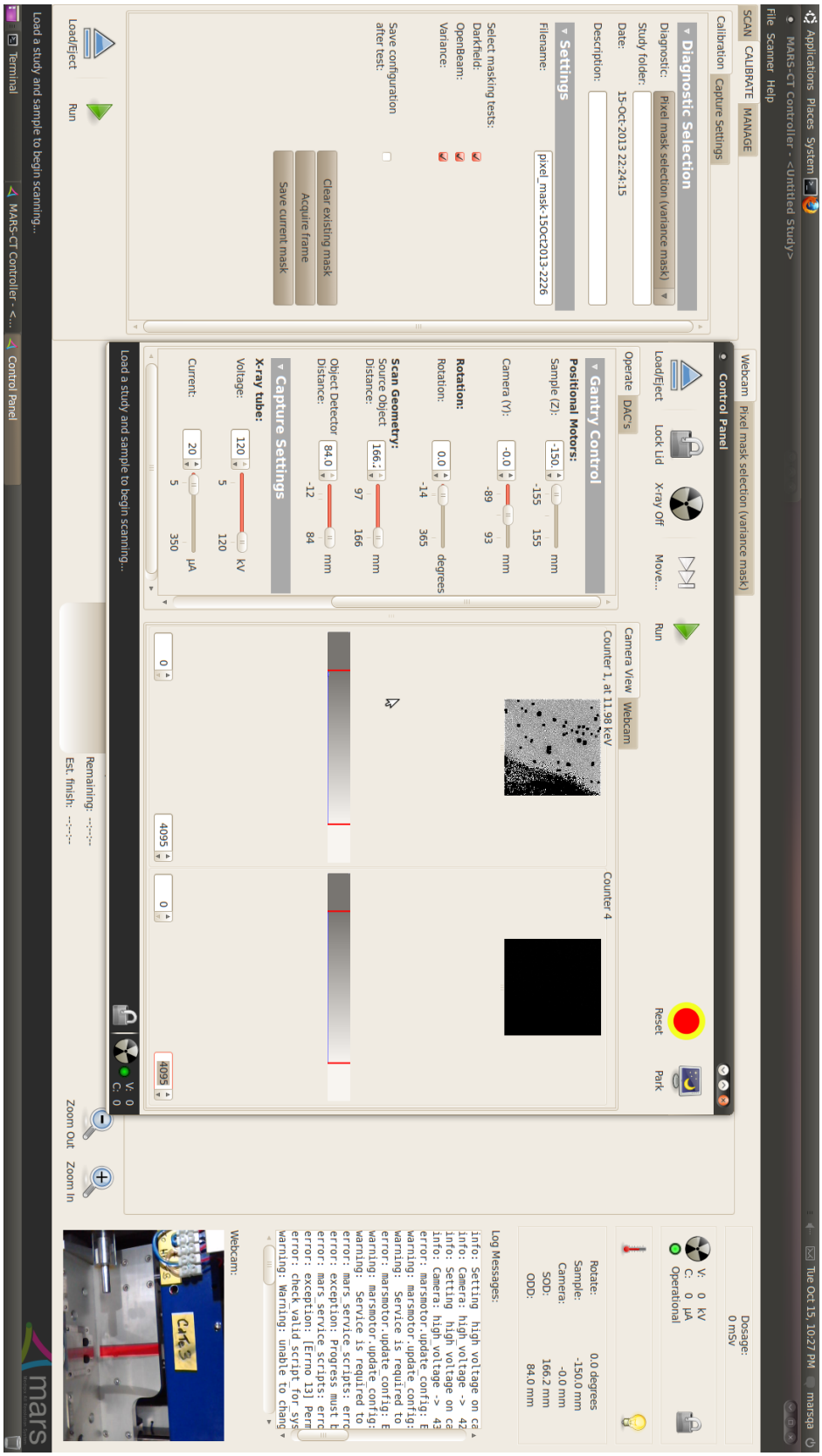

Figure 5.1: The first iteration of the pixel masking GUI.

To test the masking results, an atherosclerotic plaque was scanned with only the flatfield counts < 3 criteria applied (to eliminate non-functional pixels) and then with the full mask criteria applied. The protocol used was 2mm CdTe bonded to Medipix3RX chip, tube voltage of 80 kVp, tube current 10 µA, exposure of 50 ms, SDD 201 mm, and ThL set to 15 keV.

Results

The mask removed ~20% of all pixels on the chip used. Figure 5.2 shows the distribution of all pixels before and after masking around the expected Poisson distribution shown as a red line for variance equal to the mean. Figure 5.3 (located in the discussion) shows the mask. The black shows the pixels left on and used for scanning. The faulty pixels can be seen to be distributed widely over the entire pixel array.

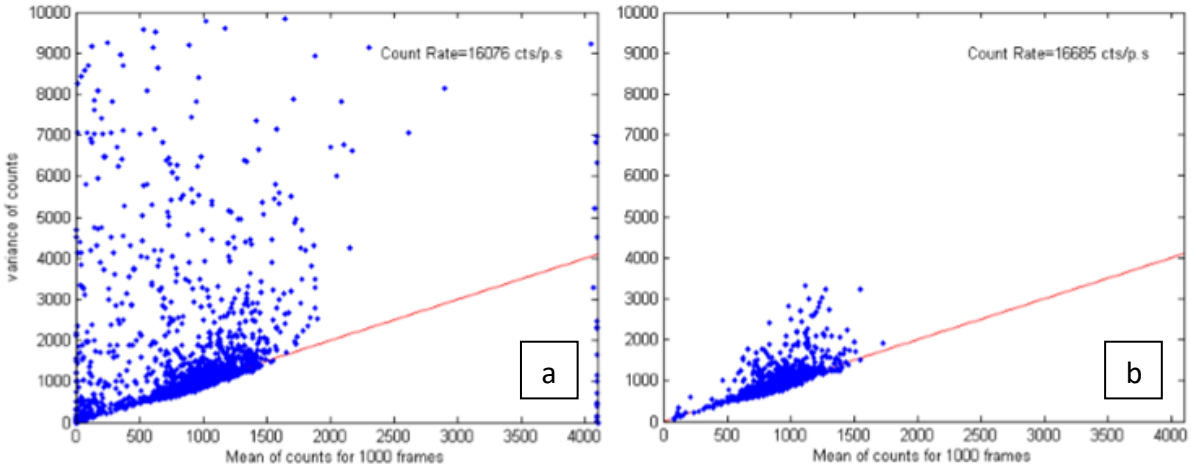

Figure 5.2: Variance in counts versus mean of counts for all pixels before and after masking. Mean counts are calculated over 1000 frames. Masking criteria were darkfield: counts > 2; flatfield: counts < 3; variance: var > 3 * mean. Used with permission [172]

Figure 5.4 (located in the discussion) shows approximately the same slice from a plaque scanned without masking on the left and with masking on the right.

Discussion

The pixel mask succeeded in removing a great deal of noise, especially ring artefacts as seen in Figure 5.4. However, in the case of this camera, so many pixels were inhibited that the data had to be filled in during post-processing using a median filter resulting in loss of resolution and contrast. This simple result indicated that inhibiting too many pixels prevented the collection of adequate data (unless an excessive amount of oversampling was used). Other researchers found that leaving most pixels on and then masking the raw data frame by frame using the same four criteria described here (but with different control values)

allowed pixels that worked properly much of the time to be used when their data was good and eliminated only when their data was faulty. Again, see the theses of Muhammad Shamshad and Marzieh Anjomrouz [1, 2].

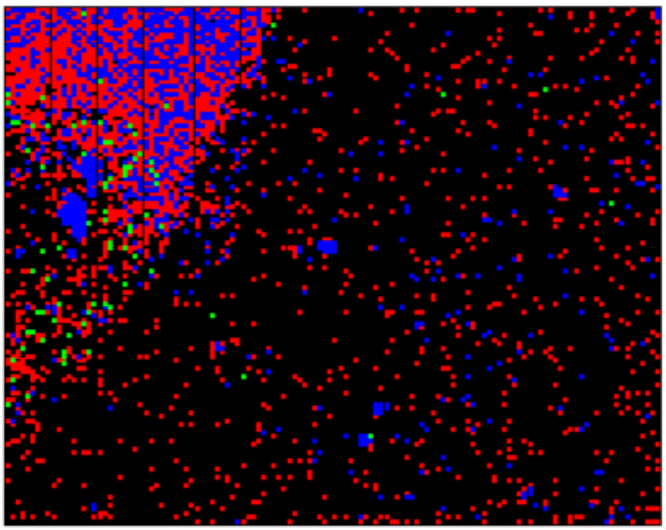

Figure 5.3: The completed mask. Red voxels are removed by the darkfield mask. Blue voxels are removed by the flatfield mask. Green voxels are removed by the variance mask. Used with permission [173]

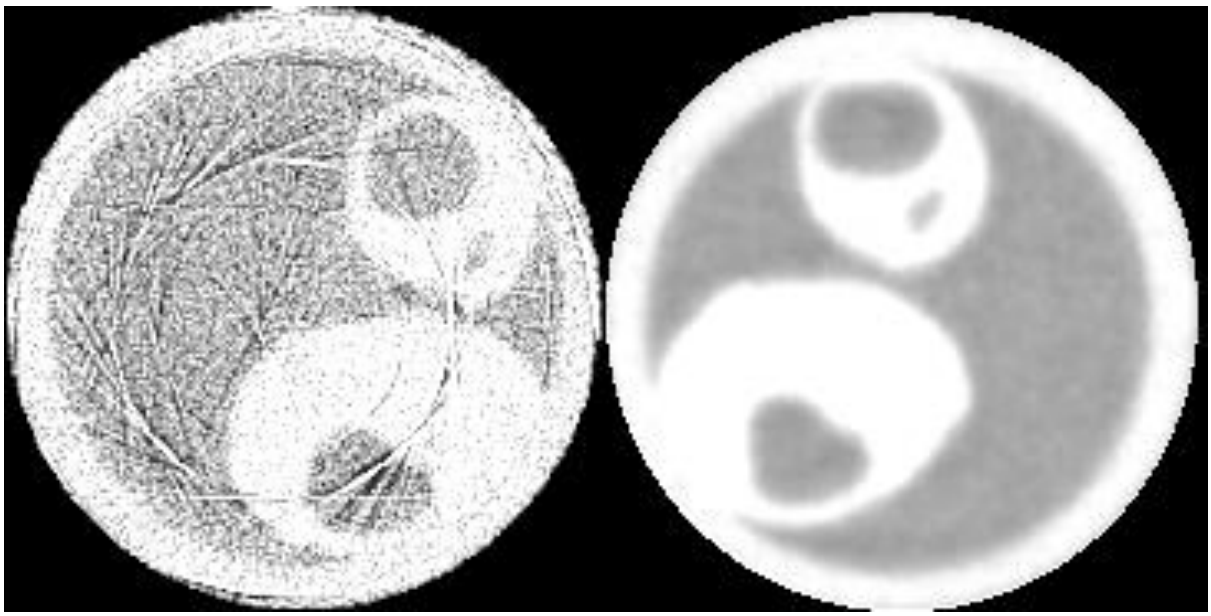

Figure 5.4: Scans of the same atherosclerotic plaque before inhibition masking and after. Both reconstructions are poor quality. The scan on the left has obvious noise produced by bad pixels. The scan on the right looks better, but so many pixels were inhibited that the reconstruction algorithm had to fill in large portions of missing data with a median filter of large radius. Both images are normalized to the mean signal of the plastic tube.

5.3 CT10 and CT11 commissioning

Introduction

Aim

Two new scanners were commissioned. Much of the testing was performed by me and Raj Panta. We set up the configuration software for the machine controllers, found the geometric alignment corrections for the reconstruction software, tested the source stability, tested the camera stability, measured the spatial resolution, and performed energy and material calibrations.

Significance

We brought two machines to full functionality for use at the University of Canterbury and the University of Otago, Christchurch. We identified issues with camera stability, source stability and CSM count rate capabilities that improved machine function and protocols. Only some key results are shown from this work.

Publication

This work was presented at MARS seminars.

Contribution

All of the work was performed in equal effort by me and Raj Panta.

Methods

The source and camera stability scans were performed with the following protocol. 3000 open beam frames were acquired. Data from a 210 pixel ROI of 'good' pixels was used. The tube voltage was set to 117 kV, the tube current was 30 µA. The first charge summing counter was set to 20 keV. The bias voltage was set to -600 V. For CT 10 the source to detector distance was 317.2 mm and for CT11 it was 282.2 mm. Filtration was 5.5 mm aluminium equivalent in CT 10 and 5.6 mm in CT 11. For source stability the camera exposure time was 5ms. For camera stability, the exposure time was 150 ms and 200 ms in two trials.

The counts should increase linearly with increases in tube current. We examined linearity in counts vs tube current in both single pixel mode and charge summing mode. The acquisition criteria were the same as for the source stability tests except that tube current was varied from 15 to 340 µA.

Results

The camera with fingerboard 3 (which holds the Medipix3RX chip) was found to behave erratically over time as seen in Figure 5.5. The mean counts over the ROI would drop to zero for extended periods and then return to normal. This behaviour was seen even when the

camera was moved to other scanners. Further investigation showed that the energy threshold setting was jumping from 20 keV to 200 keV which is above the highest photon energy for a tube kVp of 117 kV.

Figure 5.6 shows the behaviour of the measured counts, measured tube voltage and measured tube current over time for CT 10 with fingerboard 3. All three measures have a decreasing trend over time after an initial spike. The mean counts drops by ~2% over the acquisition time while the tube voltage changes by ~0.03% and the tube current changes by ~1%.

The count rate is not linear with respect to tube current in either SPM or CSM as seen in Figure 5.7. The departure from linearity is more pronounced and happens earlier for CSM.

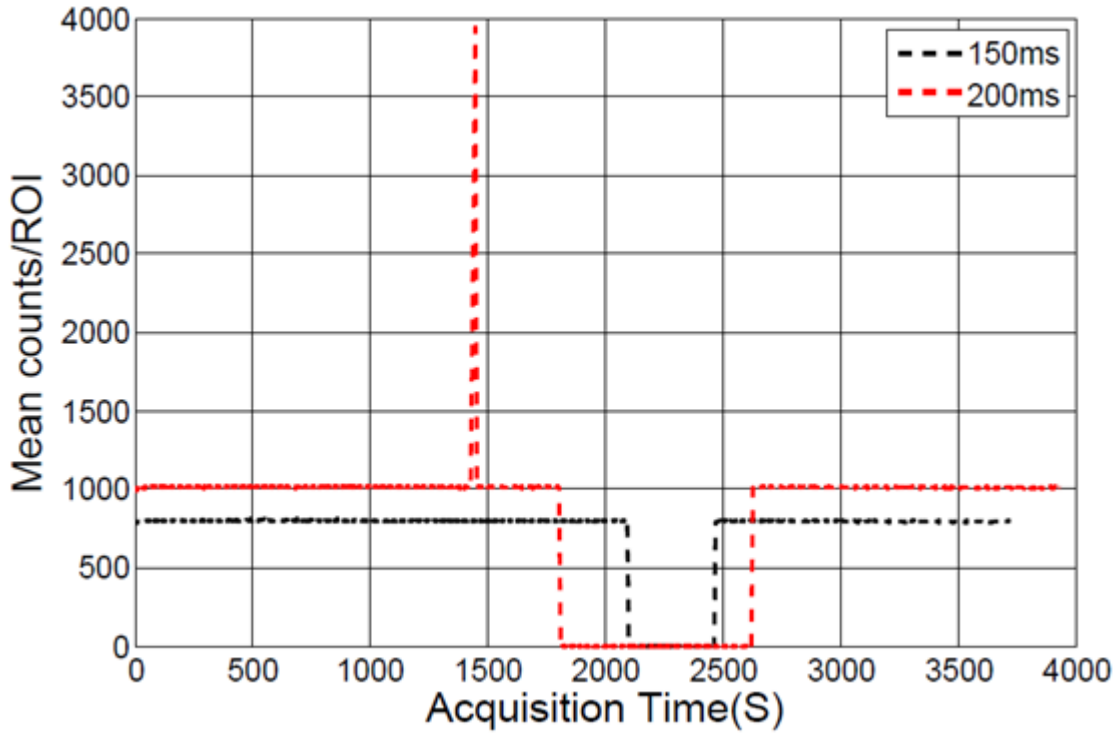

Figure 5.5: Camera instability over time for fingerboard 3 in CT 11: 2mm CdTe bonded to Medipix3RX. The mean counts per frame across a region of interest over 3000 frames. Used with permission [104]

Discussion

The commissioning of CT 10 and CT 11 prepared to machines for delivery and use. The tests highlighted here revealed several issues that needed to be resolved by developers or helped to guide protocol criteria for users.

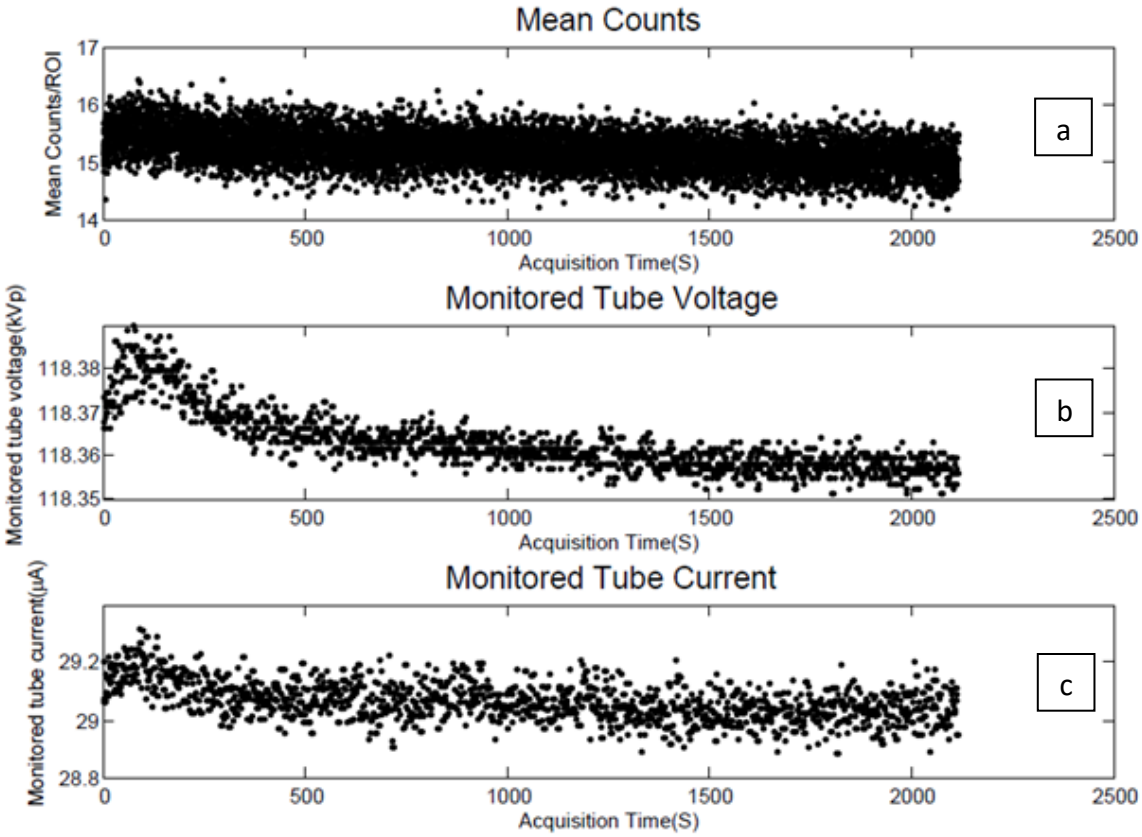

Figure 5.6: Temporal monitoring of the X-ray source in CT10. The mean counts per exposure (a), the X-ray tube voltage (b) and the x-ray tube current (c) plotted versus time in seconds. Measurement settings were 117 kVp tube voltage, 30 μA tube current, 5 ms exposure time per frame for 3000 frames. Used with permission [104]

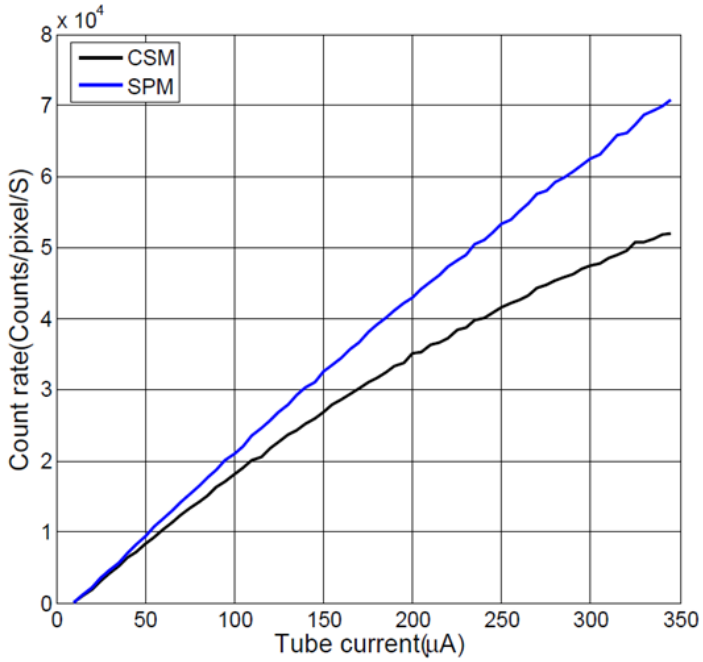

Figure 5.7: Count rate vs x-ray tube current in SPM and CSM for CT10. Used with permission [104]

The camera instability over time revealed in the plot in Figure 5.6 was found to be a result of a sudden change in the energy threshold settings for the camera. Fingerboard 3 had recently been move to a new camera body and the high voltage supply had been changed. Developers found problems with the wiring and were able to fix the instability.

The spike in voltage and current during the first 500 or so seconds of acquisition time seen in Figure 5.7 indicated that the X-ray tube needed a warm-up period before the output would stabilize. After this finding and work by other MARS developers, a 15 minute tube warm-up was applied to the machine scan software.

The count rate versus applied tube current deviates from linearity as seen in Figure 5.8. Further work by Raj Panta [104] established the departure from linearity to be at about 80 µA for SPM and about 40 µA for CSM when the tube was operated at the maximum of 120 kVp. For CSM this equated to a count rate of about 12 counts per pixel per ms and so a recommended maximum count rate for all protocols was established at 10 counts per pixel per ms.

5.4 Material decomposition analysis

Introduction

Aim

While analysing data from the plaque 108 scan (Section 3.4), I observed that many soft tissue voxels had very high Hounsfield unit values that would be expected to fall into the calcium component of the MD or very low values that would be expected to be part of the air or background. To further investigate this, I plotted the Hounsfield unit values from the 30 keV energy bin for all the soft tissue voxels in the plaque from slices 120 to 205 versus the concentration in water from the MD.

Significance

This plotting technique reveals three distinct populations of voxels in the soft tissue portion of the MD that would appear to be classified incorrectly. The voxels all appear at the border of calcifications and probably represent the MD's inability to account for the partial volume effect at the edge of dense materials. It revealed this error in the MD for the first time and lead to discussion about how to correct it in future iterations of the MD software.

Contribution

I conducted all of the work for this study.

Methods

The x, y and z coordinates of all voxels in the plaque over 86 slices (from 120 to 205) were recorded with their associated attenuation measurement in Hounsfield units from the 30 keV energy bin and water concentration in mg water/ml from the water component of the MD. Each voxel's data was then plotted on a graph of Hounsfield units versus water concentration.

Four populations of voxels were chosen from the data and each was colour coded following the colour pattern in Figure 5.8 and plotted on the attenuation reconstruction of the 30 keV energy bin. One population represented 'non-extreme' voxels (grey), while the other three had extremely low HU values (red), extremely high HU values (green) or extremely high water concentration (blue).

Results

The graph in Figure 5.8 shows the results. Three distinct populations of voxels are apparent that do not follow the expected values that should centre in a narrow range of Hounsfield units around zero and vary in water concentration from zero (for 100% lipid) to near 1000 mg water/ml for pure water (values above this are not excluded by the MD software). The legend shows the arbitrary values chosen to distinguish the extreme populations.

Colour coding the extreme voxels and plotting them on the reconstruction of the 30 keV energy bin revealed what type of voxels made up each extreme category (Figure 5.9). The low HU voxels border the air/plaque boundary, usually but not always, near calcifications as seen in the red voxels in the left hand slice. The high HU voxels are found at the plaque/plastic boundary near calcifications as seen in the green voxels in the middle slice. Finally, the high water concentration voxels were usually found within the plaque at the calcification/soft tissue boundary as seen in the blue voxels in all three slices. These voxels often formed a ring completely surrounding small calcifications.

Discussion

All three populations of extreme voxels from the plot in Figure 5.8 were found to occur at the border between two materials of very different density. This is a strong indicator that the partial volume effect is causing voxels with a spectral pattern that fits most closely to the soft tissue portion of the MD but whose HU values suggest that one material dominates the voxel's total attenuation in any given energy bin. For example, a calcified voxel near the air/plaque boundary that falls into the extremely low HU value category (red) might have a HU value of -800 that clearly indicates it is mostly air, but its spectral pattern was altered by the presence of calcification that lead the MD to include it in the soft tissue segment.

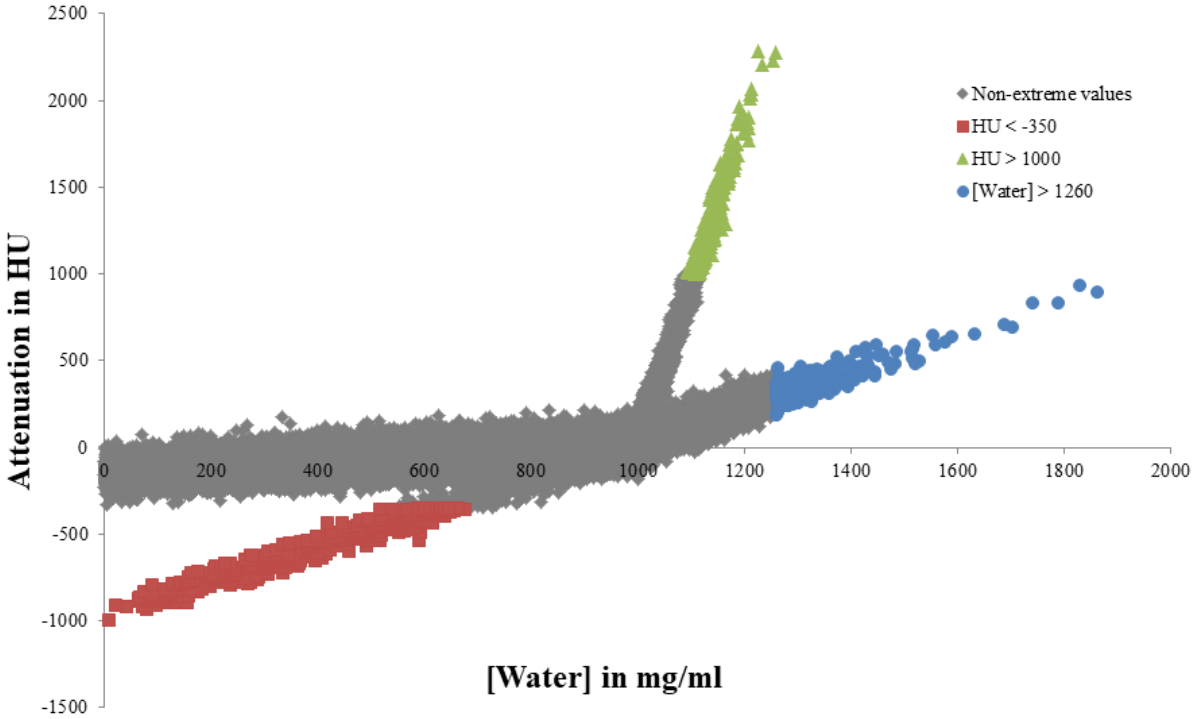

Figure 5.8: Plot of attenuation in Hounsfield units versus the concentration of water from the MD for all soft tissue voxels in slices 120 to 205 of plaque 108.

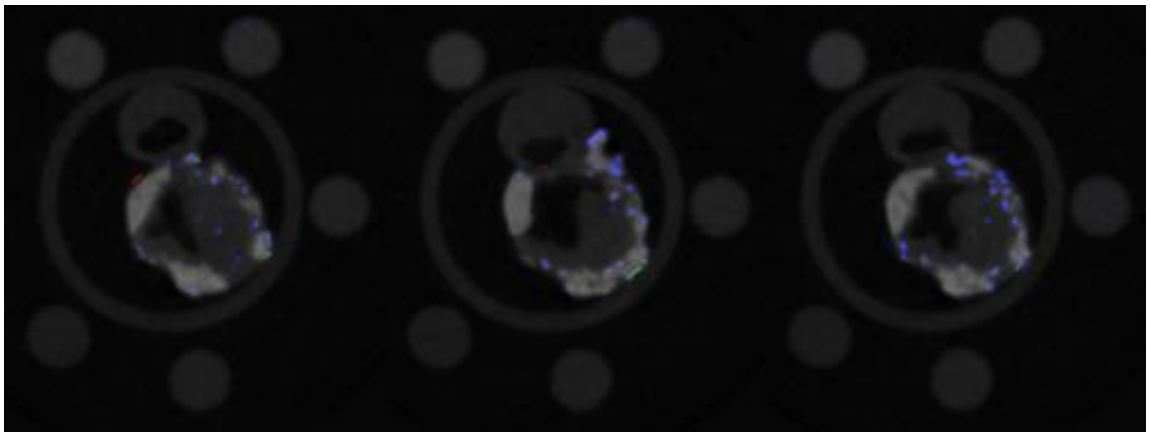

Figure 5.9: Slices of plaque 108 highlighting the three groups of aberrant soft tissue voxels from Figure 5.8. The colour scheme is the same: red for HU < -350, green for HU > 1000 and blue for water concentration over 1260 mg water/ml. The left slice highlights the red groups typical location at the air/plaque boundary near calcifications. The middle image shows the typical location of the green group at the plaque/plastic tube boundary near calcifications. The right slice highlights the blue group which occurred predominantly in the interior of the plaque within or surrounding calcifications.

Most of the voxels in all three categories were near calcifications. This may indicate that beam hardening artefacts are also affecting the data near these dense features, so the partial volume effect may not be the only factor influencing MD of these voxels.

The partial volume effect blurs the border of dense objects and prevents distinguishing small objects from surrounding soft tissue in conventional CT if the voxels size is large relative to the objects [174]. The MARS development team is aware of these issues and may attempt to account for this probable influence of the partial volume effect in future iterations of the MD.

5.5 Conclusions

I participated in various machine and data assessment projects over the course of my thesis work. This chapter highlights some of the more important results.

A first generation pixel masking algorithm was applied to the MARS camera for pixel inhibition. Results of scans with this mask revealed that most pixels should be left on and the majority of faulty pixel measurements should be masked in post-scan processing. Nevertheless, the four basic criteria for identifying faulty pixels that were defined form the core of the current pixel masking software on the commercial MARS scanner.

Two CT machines were commissioned and results from the standardized tests found several sources of error in the MARS imaging chain. The X-ray source was found to require several minutes of warm-up before its output stabilized. One camera was found to have hardware issues that caused sudden changes in the energy threshold settings. Optimal guidelines for X-ray tube operating current and camera count rate maximums were established.

A graphing technique was developed that compared HU values for a voxel to its water concentration in the soft tissue voxels of the MD. This revealed three populations of voxels with extreme HU or concentration values that usually lie on the boundary of two materials of very different density. This was a strong indicator that the partial volume effect influences the MD results for these voxels.

6 Per Pixel Energy Calibration

6.1 Introduction

The spectroscopic ability of MARS cameras is achieved with the adjustable lower thresholds for each of the eight counters on each pixel (see 2.2 and 2.4). Each pixel has independent signal processing electronics; however, the threshold settings are controlled by a 9-bit global digital to analog converter (DAC). Energy calibration is a map of photon energy in keV onto the range of available DAC values (0 to 511). Thus, every CSM_1 counter operates at the same DAC value corresponding to the user chosen energy threshold. All CSM_2 operate at another global DAC value and so on for all counters. MARS scanners are calibrated using the X-ray kVp technique (see section 2.3) applied globally, meaning a single calibration line,

$$E_\gamma = m_g I_{DAC} + c_g \quad (6.1)$$

is generated for all corresponding counters across the pixel matrix [16], giving eight lines total. E_γ is the energy in keV corresponding to I_{DAC}, the value of the global low threshold DAC for a particular counter. m_g and c_g are the slope and offset for the DAC to energy conversion, respectively.

Due to variations in sensor layer crystals, solder bonding and pixel electronics the true energy responses of the individual counters do not match, exactly, the global energy calibration (Figure 6.1)[175]. Also, limitations in pixel equalisation precision contribute to threshold dispersion [14]. This threshold dispersion distorts spatial and material information [11]. MARS images depend on the quality of spectral data, so finding the energy calibration for each pixel would improve spectral resolution and material decomposition. Several techniques exist to calibrate photon counting detector pixels individually. Most techniques use monochromatic or near-monochromatic X-ray sources like synchrotrons, radio-isotopes, and X-ray fluorescence [16, 106, 176, 177], while Panta et al. suggested but did not pursue a modification of the broad spectrum X-ray kVp technique.

I participated in two projects designed to find pixel-specific energy calibrations of the form,

$$E_{\gamma,px} = m_{px} I_{DAC} + c_{px} \quad (6.2)$$

where $E_{\gamma,px}$, m_{px}, and c_{px} are the energy, slope and offset for a specific pixel. First, I will describe a technique that uses the broad spectrum to find the energy offset of each counter from the global calibration, and thus, requires no special, monochromatic source[172]. Second, I will present work done toward an automated oblique X-ray fluorescence calibration[178].

6.2 Broad spectrum energy offset technique

Introduction

Aim

The X-ray kVp technique for calibrating MARS scanners is convenient because it uses the broad spectrum source and requires no special source or technique to create a monochromatic calibration signal. We sought to achieve a per pixel energy calibration in the same way.

The idea for this work came from the observation that if all the pixels are identical except in the threshold dispersion, then a simple threshold scan will measure the relative energy offsets of each pixel from the mean by simply finding the DAC value for each pixel that gives counts closest to the mean counts for the chip at the global DAC. Figure 6.1 shows this situation. The upper graph shows that there are 400 counts expected at ThL of 40 keV. Threshold scans for 3 pixels are shown below and the DAC value counting 400 is aligned to 40 keV, giving a per pixel calibration. If the global threshold DAC is set to 100, only pixel 1 will measure 40 keV; pixel 2 will measure 42 keV and pixel 3 will measure 38 keV.

In reality, pixels' counts differ for many reasons other than threshold dispersion. We developed a technique that would account for differences in pixel behaviour and effective pixel area, thereby isolating the inter-pixel threshold dispersion effect and producing a per pixel energy calibration.

Significance

Threshold dispersion is a known source of noise in the Medipix3RX chip [4, 16]. The global energy calibration cannot correct for this. Using the proposed technique, a calibration line is calculated for each pixel and this correction could be applied within the current reconstruction and MD process, though that work has yet to be completed. MARS is attempting to move to a simultaneous reconstruction and MD using projection data and some form of per pixel energy calibration correction will be applied. This technique offers one simple solution that requires no new equipment or materials.

Publication

The work described is published in the Journal of Instrumentation [172].

Contribution

For this work, I contributed to the concept development, experimental design, data collection and manuscript editing. My primary contribution was in the conceptual ideas and the experimental designs for both the offset and fluorescence measurements.

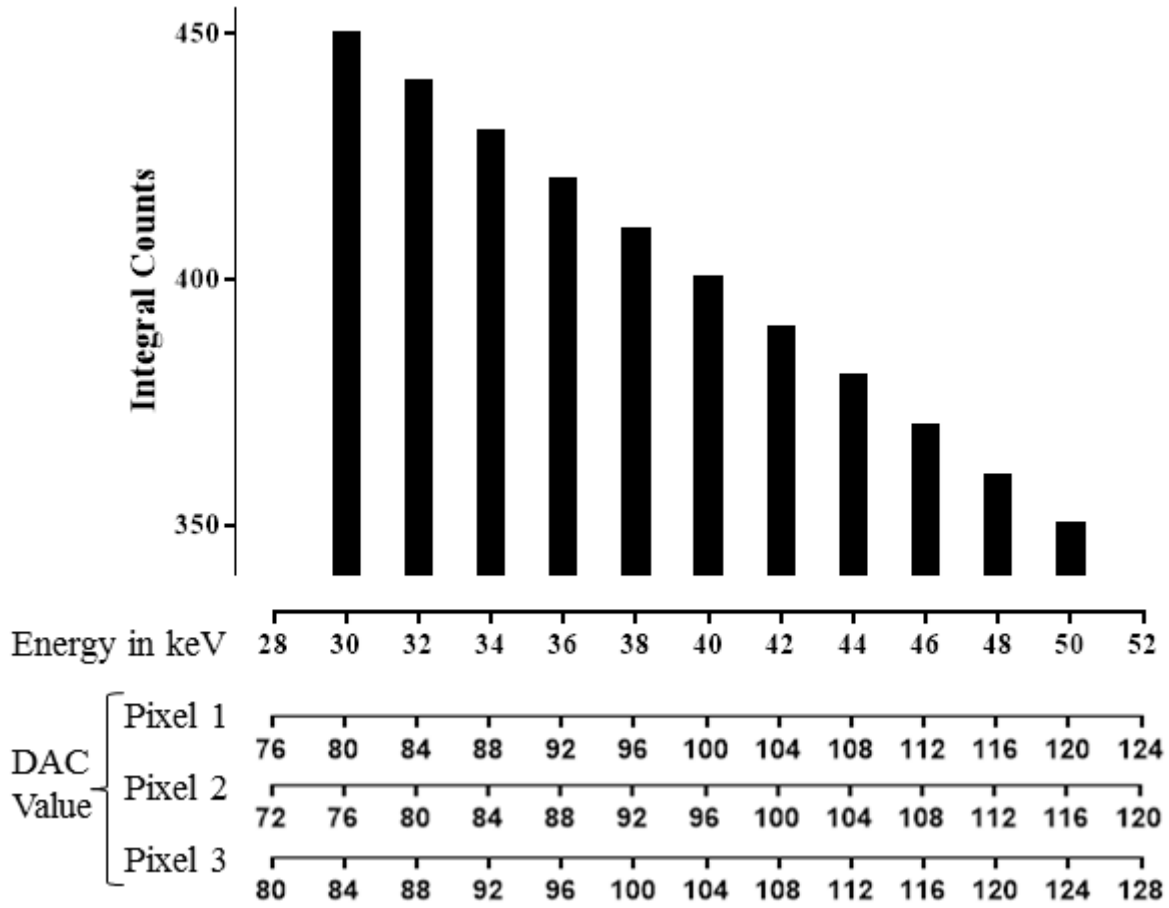

Figure 6.1: A portion of a hypothetical spectrum with integrated counts versus energy and the response of three pixels that are identical except in threshold offset. If the global threshold DAC value is 100, Pixel 1 measures 40 keV, Pixel 2 measures 42 keV and Pixel 3 measures 38 keV.

Methods

Overview and Definition of Terms

To achieve a per pixel calibration, we must isolate and quantify the threshold dispersion while accounting for counting variations between pixels due to other factors. After applying a count correction to pixel data at the global DAC value, the difference in counts between a pixel's expected counts and its actual counts is converted to an energy difference. The energy offset is measured at several energies and a line is fit to the data to give the per pixel energy calibration (Equation 6.2).

The work flow is summarized in Figure 6.2.

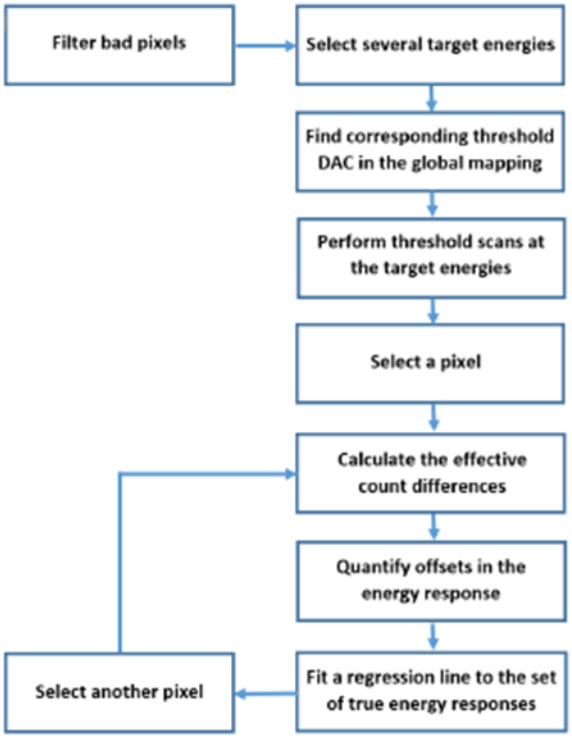

Figure 6.2: Flow chart for the broad spectrum per-pixel energy offset technique. Used with permission [172]

Data acquisition

The data presented were collected using MARS camera CdTe-3 equipped with a Medipix3RX ASIC bonded to 2mm of CdTe at a pixel pitch of $(110\ \mu m)^2$. Scan parameters were 120 kVp, tube current of 30 µA, and 2.8 mm aluminium equivalent filtration. Results are shown for a 100 pixel region of interest using counter CSM_1, but the technique can be applied to all pixels and all counters.

The camera inhibition mask was applied (see Section 5.2) to remove un-useful pixels. At ten energies, 20 to 110 keV in steps of ten, an open-beam threshold scan of five consecutive DAC values centred on the global DAC value for the chosen energy was performed (Figure 6.4). 200 frames were collected at each value and the mean counts for each pixel calculated. 200 frames are sufficient to eliminate quantum noise effects.

Effective Count Difference

We must account for inter-pixel count variations not resulting from threshold dispersion. The threshold for C_{arb} (see Chapter 2) is set during equalisation just above the noise floor[14]. With added filtration, C_{arb}'s threshold is well below the lowest energy photons in the spectrum (Figure 6.3). This means that C_{arb} data should be independent of threshold dispersion. Where C_{arb} is the mean counts for a specific pixel's arbitration counter and $\overline{C}_{arb}$ is the global mean for the detector, the ratio $C_{arb} / \overline{C}_{arb}$ is a generalized correction, termed the effective pixel area, for counting differences unrelated to threshold dispersion. Now, if there

was no threshold dispersion, then for $\overline{C}$, the mean counts for a particular counter across the detector, we define the expected counts, C_e, for a pixel as,

$$C_e = \overline{C} \left(\frac{C\text{arb}}{\overline{C}\text{arb}} \right) \quad (6.3).$$

The effective count difference, C_{diff}, for a pixel that has mean counts C_{px} is defined as,

$$C_{diff} = Ce - C_{px} \quad (6.4).$$

C_{diff} measures the threshold dispersion-related difference in counts of a pixel from the global mean at a particular global energy setting under a particular flux.

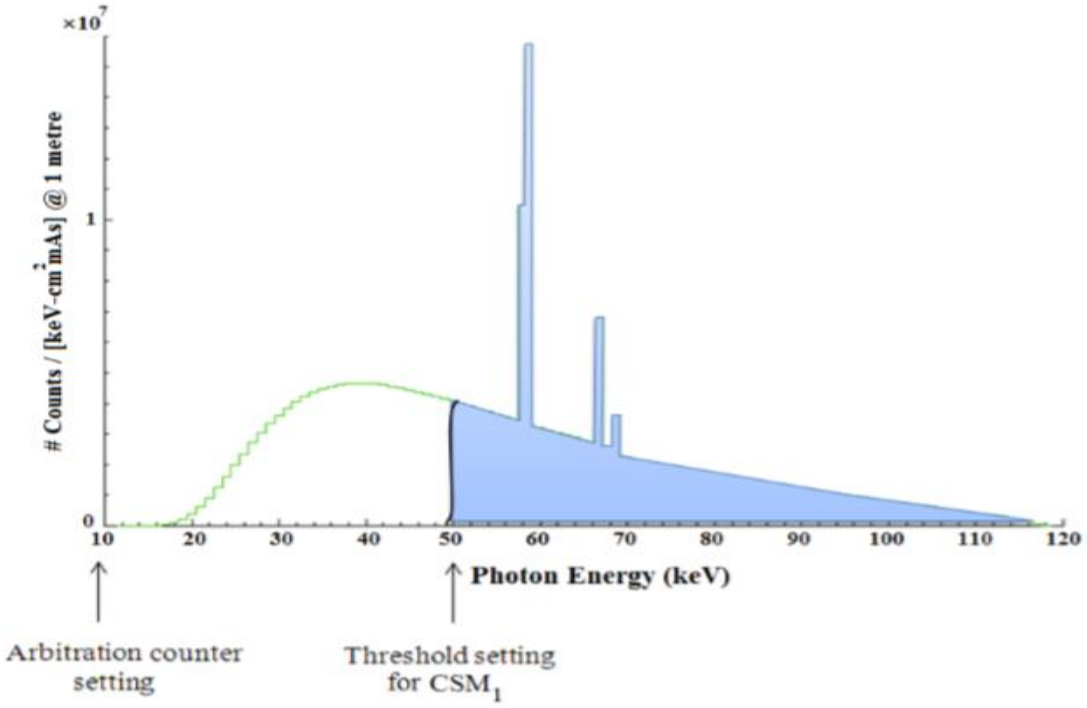

Figure 6.3: The estimated spectrum for this study. ThL for the arbitration counter is well below the low end of the spectrum. Data represents all the events counted above the ThL setting for each counter (blue region). Used with permission [172]

Per-pixel energy mapping

To progress to a per pixel energy calibration, C_{diff}, must be converted to an energy offset at each of the measured energy settings. Figure 6.4 shows the mean counts data for a single pixel at the global DAC value plotted against the global energy setting. The inset displays the pixel's behaviour for the 5-step threshold scan centred on the global DAC value (80), corresponding to 30 keV. For each pixel, a slope of counts versus ThL is calculated at each energy ($\Delta C/\Delta Th$). Assuming that the slope of the global energy calibration ($m_{g} = E\gamma/\Delta Th$) is roughly valid for all pixels, then, for the experimental spectrum used, the keV per count are given by,

$$\frac{\Delta E_\gamma}{\Delta C} = \frac{\Delta E_\gamma}{\Delta Th} \times \frac{\Delta Th}{\Delta C} \quad (6.5)$$

The energy offset for a given pixel ($\Delta E_{\gamma,\mathrm{px}}$) at a particular energy is then,

$$\Delta E_{\gamma,\mathrm{px}} = C_{\mathrm{diff}} \times \frac{\Delta E_\gamma}{\Delta C} \quad (6.6)$$

So, at a global energy setting, ($E_{\gamma,\mathrm{global}}$) the actual energy measured by a pixel at that DAC value is

$$E_{\gamma,\mathrm{px}} = E_{\gamma,\mathrm{global}} - \Delta E_{\gamma,\mathrm{px}} \quad (6.7)$$

For each pixel, a line is fit to the ten values of $E_{\gamma,\mathrm{px}}$ versus I_{DAC} to give the per pixel energy calibration, Equation 6.2.

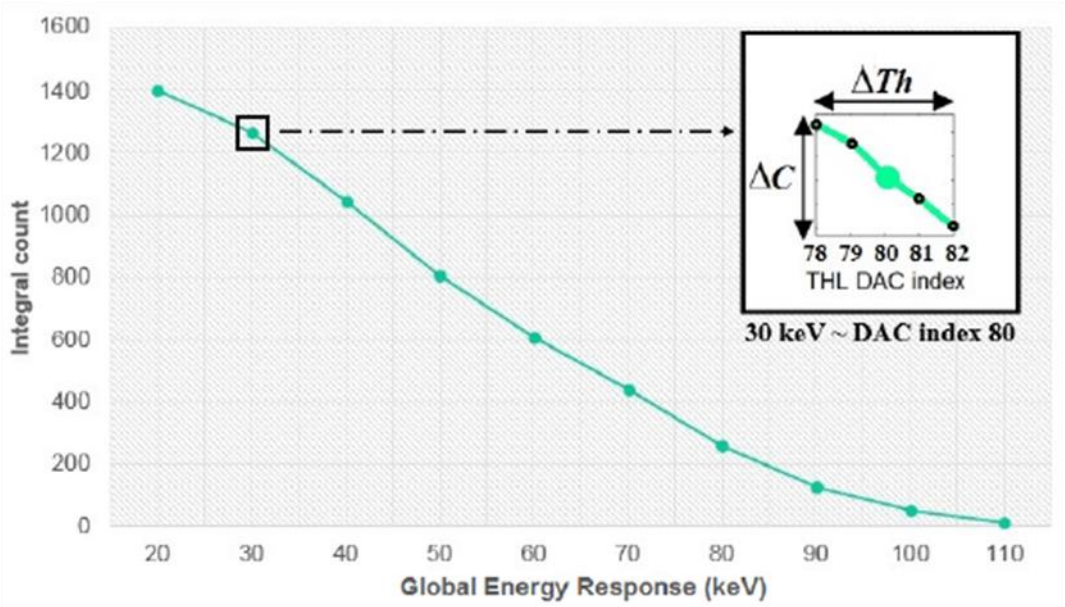

Figure 6.4: The mean counts for a single pixel at the global DAC for the experimental energies. The inset shows the additional four data points of the 5-step threshold scan around 30 keV. Used with permission [172].

Results

Per-pixel results

The slopes of the per-pixel energy calibration for the upper left 25 pixels of the 100 pixel ROI are shown in Figure 6.5 (a). The minimum R^2 value was 0.998. The magnitude of the greatest difference in slope from the global calibration is 0.0276 keV/DAC. This corresponds to a divergence of that pixel from the global calibration of 5.75 keV over 208 DAC steps (about 100 keV).

0.4529	0.4766	0.4854	0.4869	0.4840
0.4715	0.4625	0.4892	0.5008	0.4909
0.4850	0.4831	0.4822	0.4649	0.4852
0.4933	0.4993	0.4864	0.4833	0.4757
0.4845	0.4888	0.4805	0.4773	0.4838

Global Slope = 0.4805 keV/DAC keV

(a)

58.04	61.36	61.81	60.84	61.57
61.71	60.42	59.16	59.89	60.87
62.46	60.34	59.00	58.72	58.18
58.39	56.50	60.14	60.04	60.08
56.59	57.43	60.12	57.86	62.16

Global Threshold = 60

(b)

Figure 6.5: Results of the broad spectrum energy offset technique for the upper left 25 pixels of the 100 pixel ROI. (a) Slopes of the per-pixel energy calibration lines. (b) Actual energy measured by each pixel when thresholds are set to the global DAC for 60 keV. Used with permission [172]

Figure 6.5 (b) maps the per-pixel energy response at a global setting of 60 keV for the same 25 pixels. The largest difference from the global value is 3.5 keV and the largest difference between pixels is 5.96 keV. For the 100 pixels of the ROI, the root-mean-square error of the energy offsets varies from 1.38 keV (at 30 keV setting) to 1.87 keV (at 100 keV).

Evaluation using molybdenum fluorescence measurements

The per-pixel energy calibrations acquired with the broad spectrum technique were compared to the global energy calibration using threshold scans of oblique X-ray fluorescence from a molybdenum foil placed between the source and camera (see Section 6.3 for the procedure) [178]. The $K\alpha_1$ and $K\alpha_2$ fluorescence energies for molybdenum are 17.48 and 17.37 keV, respectively. The difference of 0.11 keV is insignificant in relation to the sensor sensitivity of around 0.48 keV/DAC.

Figure 6.6 plots the difference in counts between DAC settings three steps apart (e.g. counts at DAC 50 minus counts at DAC 53) versus energy for the global energy calibration (6.6 (a)) and the per-pixel calibration. To reduce quantum noise, 100 frames per DAC were averaged. Points are averaged over the100 pixel ROI. The global energy calibration has a broader, noisier peak with full width at half maximum (FWHM) of 5.69 keV. The per-pixel energy calibration has a single peak with FWHM of 4.08 keV, a reduction of 28.3%. The maxima are at 17.89 keV (error of +0.41 keV from $K\alpha_1$) for the global calibration and 17.37 keV (error of -0.11 keV) for the per-pixel method.

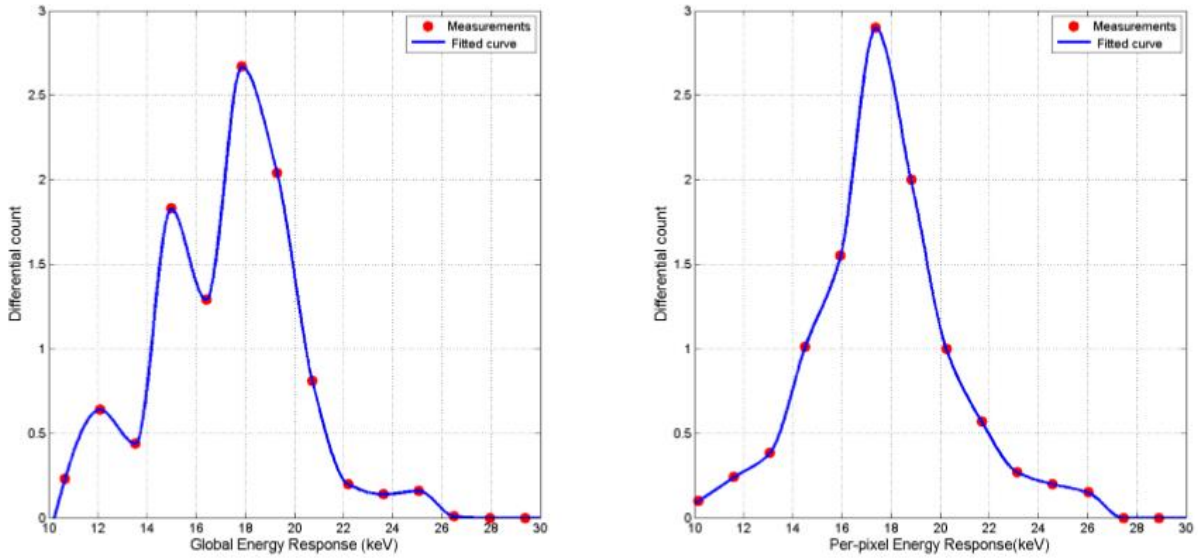

(a) (b)

Figure 6.6: Differential counts versus energy for a threshold scan across the molybdenum Kα fluorescence energy of ~ 17.5 keV. DAC values are converted to energy using (a) global energy calibration by the kVp technique [16] and (b) broad spectrum per-pixel technique [172]. Used with permission [172]

Discussion

The broad spectrum per-pixel energy offset technique produces per-pixel energy calibration lines that improve the energy resolution of the Medipix3RX based MARS camera. This should improve attenuation and material reconstructions. The accuracy and precision are both improved as shown by the molybdenum fluorescence data. The true energy response for each pixel can be calculated for any global setting and the range of energies measured by the entire chip assessed.

Like the kVp global calibration method, the technique does not require any special materials, equipment or set-up, so it can be easily implemented and automated on MARS scanners. Only two additional measures are required to achieve pixel specific calibration. The effective count difference provides a simple correction for inter-pixel count variations not due to threshold dispersion. This enables the counts per DAC step, $\Delta C/\Delta Th$, to be used to find the energy offset for each pixel due to threshold dispersion. Parameters must be constant for the entire procedure (except DAC steps of course) to ensure that the value of counts per DAC step is correlated with the effective count difference. Despite this, once the pixel specific calibration lines are established, they should apply to any scan parameters.

Because of the global DAC settings for ThL, the per-pixel calibration cannot be applied to data acquisition, but can be used to improve data processing. The algebraic reconstruction technique used could be modified to use the true energy response of each pixel and the raw count data. This process is not simple because the attenuation value for each voxel of the reconstructed volume is calculated from the input of many pixels, which would each have

different energy bin ranges. Alternatively, a library of counts per keV could be assembled for different flux rates and a rough correction to the counting data of each pixel could be performed on the raw data and flatfields before reconstructing based on the global energy thresholds. This technique could be easily applied but assembling the counts per keV library would require a large array of data points. Neither of the suggested data processing corrections has been attempted, so the actual impact of per-pixel energy calibration on reconstruction has yet to be determined.

This procedure assumes that the chip averages represent the most accurate value (i.e. pixels that count at the chip average are correctly measuring energy) and adjusts other pixels from there. Thus, while the magnitude of the energy offsets calculated may be correct, the entire calibration may have an additional, unidentified offset. This fact makes good pixel masking (Chapter 5) especially important since inclusion of malfunctioning low or high counting pixels could affect the mean count values used in the calculations. The data presented used only a 100 pixel region of interest that closely followed poisson counting statistics and had offsets of less than 4 keV. In future work with the entire chip, it will be important to monitor the effect of more extreme pixels. The uncertainty in using chip means as a standard is one argument for direct per-pixel calibration using foil fluorescence or monochromatic X-rays [16, 178].

Threshold dispersion was smallest at the lowest energies measured and largest at the highest energies. This trend is expected because pixel equalisation is performed at the noise floor (i.e. at the lowest energy)[14, 16]. The R2 value of 0.998 or higher for all per-pixel calibration lines indicates that fewer data points could be used to streamline the procedure.

As seen in Figure 6.6 (b), the energy response function still has dispersion and distortion. This is partially explained by the fact that X-ray fluorescence is not a true monochromatic input. The Kβ fluorescence of molybdenum is only 2 keV above the Kα. Other sources of error include flux variations, Fano noise, leakage current, charge trapping, incomplete charge collection, resistance and capacitance variations, charge sharing, pulse pile-up and imperfections in the per-pixel calibration [11, 17, 175, 176]. Any of these errors that are systematic in nature might be correctable if they can be quantified. The reconstruction uses flatfield correction which accounts for some of these error sources[179]. Using the Medipix charge injection electronics might allow a separation of sensor and electronic noise, but the injection pathway contains its own noise[175]. Spatial and temporal flux variations are not expected to be significant based on work done for the MARS X-ray source model[180]. Pulse pile-up is also not significant since the global, per-pixel and fluorescence calibration data are collected at count rates (less than 10 counts/pixel/ms) within the linear behaviour region of the camera used (see Section 5.3). Charge sharing is largely corrected for by using charge summing mode in the Medipix3RX but may still contribute imprecision[11]. Incomplete charge collection is more significant in thicker sensor materials such as the 2mm CdTe used for this work[107] and typically contributes to the low energy tail.

6.3 Oblique fluorescence per-pixel energy calibration

Introduction

Aim

The MARS team is attempting to use fluorescence from up to six different monoatomic foils mounted on a single aluminium filter plate to obtain a quality per-pixel energy calibration. Calibration with monochromatic X-rays of known energy provides a direct map of energy to DAC value on a per-pixel basis. However, monochromatic X-ray sources like synchrotrons and radioisotopes are not practical for periodic calibration of MARS cameras mounted in scanners due to size, cost, convenience, time and safety issues. Characteristic X-ray fluorescence from monoatomic foils mounted on the filter bar of the MARS scanner's X-ray tube provides a nearly monochromatic X-ray source (see Section 2.11) and an easily automated calibration procedure. Since the foils are closer to the detector than the source and fluorescence is emitted isotropically, a pure fluorescence signal can be detected by positioning the detector out of the main beam. Using the automated collimators between the foils and the detector, an isolated beam of fluorescence can be used to illuminate the properly positioned detector with minimal scatter contamination.

Significance

Easily automated, foil fluorescence energy calibration will allow on demand calibration and quality assurance for end users, reducing the need for factory support.

Publication

This work is featured in the Journal of Instrumentation [178]. Lieza Vanden Broeke's Master's thesis expanded on the foil thickness and fluorescence output calculations while featuring the initial fluorescence measurements that appear in this thesis [181].

Contribution

I was the team leader for the foil fluorescence project. The team consisted of me and four other MARS students or employees: Brian Goulter, Ali Atharifard, Lieza Vanden Broeke and Mohsen Ramyar. I lead the foil fluorescence team through the initial experimental design phase and the first molybdenum and lead fluorescence measurements featured in this chapter. I played a significant role in experimental design and mathematical derivations for determining optimal foil thickness [181]. I also contributed to data collection, data analysis and document editing.

Methods

Foil fluorescence measurements

We successfully measured oblique fluorescence from two of the six foils mounted in the filter bar of the MARS scanner, lead and molybdenum. The physical arrangement of the foils and scanner are illustrated in Figure 6.7. Indium was also attempted, but quality data was not obtained and is not presented here.

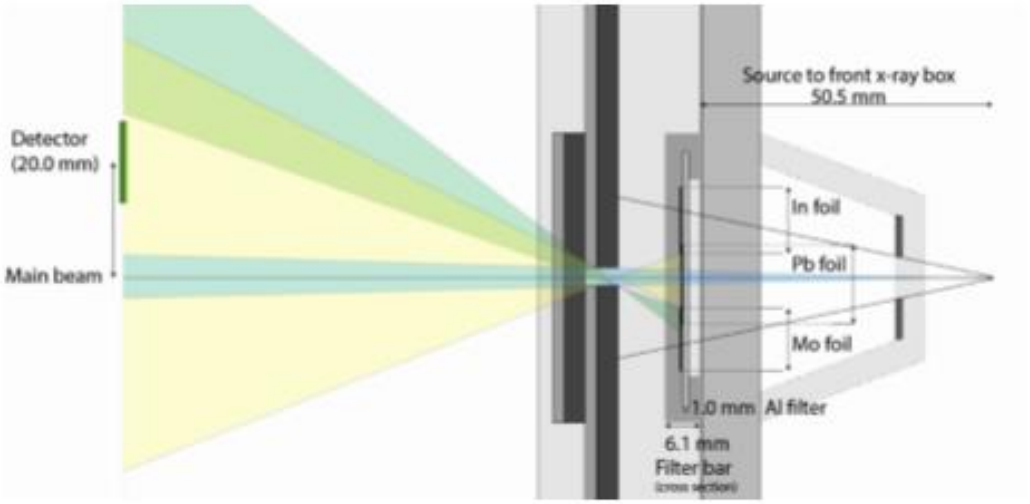

Figure 6.7: The scanner setup used to measure oblique fluorescence of lead. The detector is positioned in a region (yellow) of pure Pb fluorescence between the collimated main beam and a region of overlap between Mo and Pb fluorescence (green). By repositioning the horizontal collimator gap in front of the Mo foil, an isolated Mo fluorescence signal is created in a similar location. The source to detector plane distance is 150 mm. Used with permission [178]

Data collection consisted of a threshold DAC scan across a range of DAC values that surrounded the K_α photon energy for the foil of interest. At each DAC step, 50 (for Mo) or 100 (for Pb) frames were recorded and then averaged. A differential spectrum was calculated by subtracting every third DAC step (i.e. the averaged frame from DAC 100 is subtracted from the averaged frame from DAC 97)

Table 6.1: Scanner settings for the molybdenum and lead XRF measurements.

Foil	Molybdenum	Lead
Detector	Medipix3RX	Medipix3RX
Sensor	2 mm CdTe	2 mm CdTe
Camera mode	CSM	CSM
Bias voltage (V)	-600	-600
SDD (mm)	150	150
Frames per DAC step	50	100
Tube Voltage (kV)	40	95

Tube Current (μA)	350	300
Exposure (ms)	10,000	10,000
Filtration (mm) Al or brass	2.8 Al (1.8 intrinsic + 1 added)	2.8 Al (1.8 intrinsic + 1 added)
Focal spot size (μm)	~50	~50
DAC step range	40 to 100	165 to 220
Foil thickness (μm)	300	300

Optimal foil thickness

Difficulties, especially very low photon counts, encountered while attempting our first oblique fluorescence measurements, lead us to investigate the effect of foil thickness on fluorescence flux. At the time of the research presented here, we were still using the available foils and had not experimented with optimizing foil thickness. This work is theoretical and will guide our future efforts in foil XRF calibration.

As a broad spectrum X-ray beam passes through a monoatomic foil, K_α photons are produced and absorbed until the far side of the foil is reached, at which point a flux of fluorescence photons may travel to the detector for energy calibration. At some optimal thickness, the number of new K_α photons produced equals the number of previously produced K_α photons absorbed and a maximum number of K_α photons is emitted toward the detector. Any thicker and the number of new photons is less than the number of previous photons absorbed and the K_α flux declines.

For a monochromatic input, I_0 of photon energy, E, over the K-edge and a foil of thickness, L, combining the generation of new K_α photons at a point x in the width of a foil with the attenuation of previously generated K_α fluorescence at the same point gives:

$$N_{K_\alpha}(L,E) = \int_0^L \omega_{K_\alpha}\tau_K(E)I_0(E)e^{-\mu(E)x}e^{-\mu_{K_\alpha}(L-x)}dx$$

$$= \omega_{K_\alpha}I_0(E)\frac{\tau_K(E)}{\mu_{K_\alpha}-\mu(E)}\left[e^{-\mu(E)L}-e^{-\mu_{K_\alpha}L}\right] \qquad (6.8)$$

N_{K_α} is the number of fluorescence photons emitted, ω_{K_α} is the fluorescence yield for K_α photons, τ_K is the K-shell photoelectric linear attenuation coefficient (μ) at E, μ(E) is the linear attenuation coefficient at E, x is the distance from the input side of the foil, and $\mu_{K\alpha}$ is the linear attenuation coefficient of the material for K_α photons.

Integrating equation 6.8 over all energies from the K-edge to the maximum photon energy (or to infinity) in a broad X-ray spectrum will give the total number of fluorescence photons emitted from a foil of thickness, L. However, this integration is very complicated since the

formulas for I_0, τ_K , and μ are all complex. Thus, a numerical integration is performed by calculating a model spectrum with SpekCalc, then finding and summing N for each discreet energy bin from the K-edge to the maximum photon energy. For this work, the spectrum was calculated based on a 120 kVp source and 2.9 mm Al filtration. An energy bin size of 0.1 keV was used. Values of τ_K were obtained from Scofield (1973) [182] and then interpolated for each energy bin. Values of μ(E) were obtained from the NIST XCOM database [183].

$N_{K\alpha}$ was then calculated for a range of foil thicknesses from 0 to 1 cm. The optimal foil thickness is then simply the value of L with the largest $N_{K\alpha}$. Calculations were performed for molybdenum, indium and lead foils.

Results

The XRF measurements obtained from a single pixel are displayed as a differential spectrum in Figure 6.8. The peak for Mo occurs at DAC = 54 and corresponds to the K_α fluorescence at ~17.5 keV. The peak for Pb is at DAC = 177 and corresponds to the K_α of ~75.0 keV. Calculating the energy calibration line from this data gives a slope of 0.467 keV/DAC.

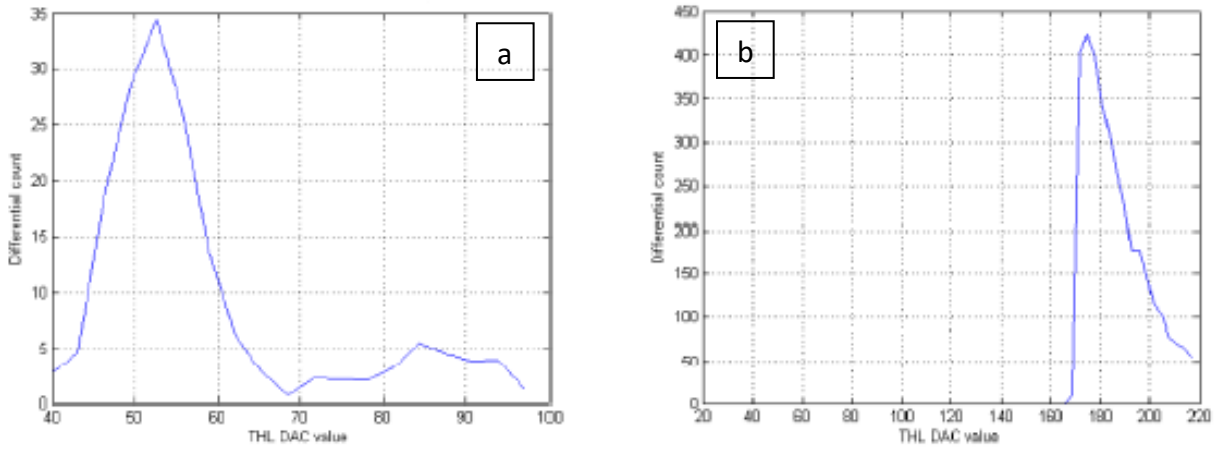

Figure 6.8: Differential XRF measurements from (a) molybdenum and (b) lead. Each graph represents data from a single pixel. Used with permission [178]

The graphs in Figure 6.8 are for a single pixel. Most well behaved pixels produced a good signal for lead; but, molybdenum was much more inconsistent, with many well behaved pixels failing to produce a clear XRF peak. These inconsistencies were even more pronounced for the indium foil (data not shown) and lead us to pursue the optimal foil thickness calculations that follow.

The theoretical calculations for optimal foil thickness are shown in Figure 6.9. The optimal thickness for molybdenum is 50 μm, for indium it is 100 μm and for lead it is 210 μm.

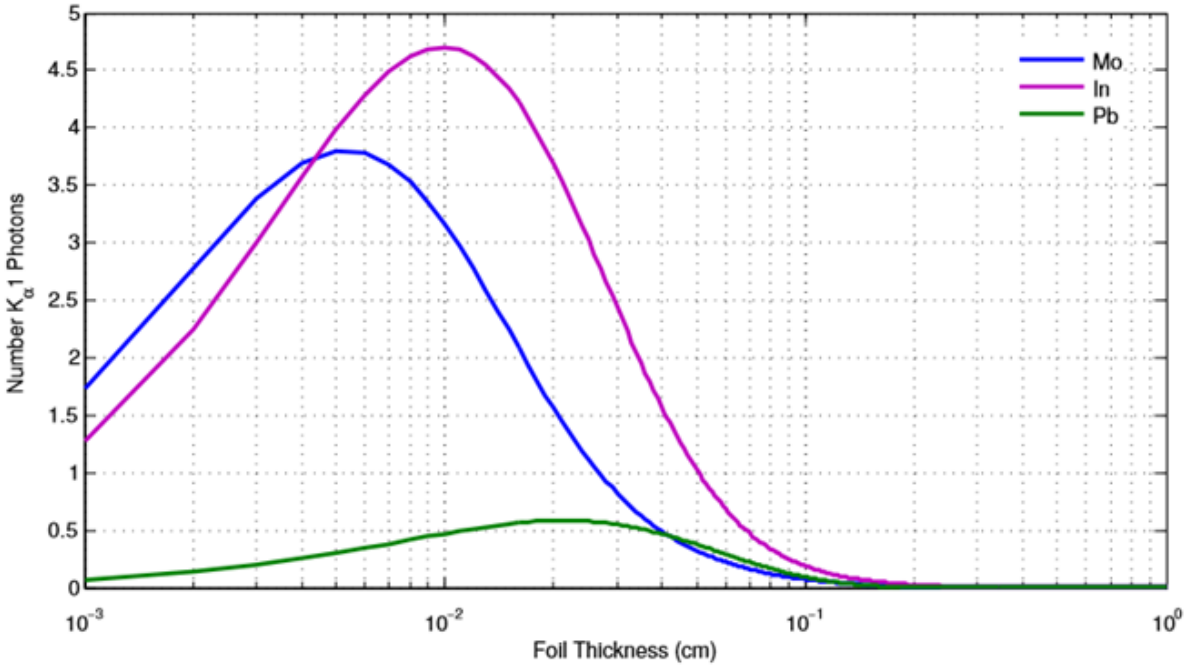

n

Figure 6.9: Number of $K_{\alpha 1}$ photons versus foil thickness for molybdenum, indium and lead. For simplicity, the calculations were performed leaving out constants, so the counts are not representative of a true expectation. Used with permission [181].

Discussion

Oblique fluorescence is a viable per-pixel energy calibration technique for the MARS scanner. A clear XRF peak was obtained for molybdenum on some pixels and for lead on most pixels. The calculations of optimal foil thickness indicate that the 300 μm Mo and In foils are not optimal (Figure 6.9) and thinner foils should be acquired for future work.

The calibration slope of 0.467 keV/DAC step for one pixel was obtained from just two points, lead and molybdenum. It is similar to the global calibration slope of 0.4805 keV/DAC and falls in the range of slopes, 0.4529 to 0.5008 keV/DAC, found for 25 pixels using the broad spectrum energy offset technique in Section 6.2. This further indicates the potential for foil fluorescence as an energy calibration technique.

The trouble in obtaining a clear fluorescence signal for all well-behaved pixels using the molybdenum and indium foils indicates that the procedure must be refined. First, the foil thicknesses should be changed to match the optimal values calculated in this work. Because Compton scattering is more prevalent in the forward direction [96], it may introduce more noise in our geometry than is found in reflection arrangements that position the detector at a greater angle from the input beam axis. MARS developers have measured significant scatter in the detector plane (internal communication) and the narrow collimation may introduce greater scatter [184].

One goal in developing the foil fluorescence technique is simplicity and ease of automation. By adding other collimators in front of the source or detector we might create a cleaner signal

[185], but at the price of either having to add equipment to the machine that would require significant redesign or losing full automation by requiring a person to attach them for each calibration procedure.

Future work will concentrate on optimizing the procedure. Foil thickness, measurement geometry and simple collimation to reduce scatter will all be investigated.

6.4 Conclusions

Two viable techniques for creating a per-pixel energy calibration for MARS scanners were presented. The broad spectrum energy offset technique is easily automated and requires no special equipment. It measures the effective pixel area to eliminate noise unrelated to threshold dispersion and relies on the effective linearity of counts versus DAC step over very short threshold windows to quantify an energy offset for each pixel from the global energy correlated to a particular DAC value. The oblique fluorescence technique requires the placement of monoatomic foils in the filter bar for the X-ray source, but is also easily automated and provides a direct map of photons of known energy onto the threshold DACs of each pixel.

The broad spectrum technique reduced the FWHM of the molybdenum energy response for a group of 100 pixels by 28%. It is a completed technique that could be implemented at any time if the reconstruction algorithm were modified to accept individual pixel calibrations. The broad spectrum offset technique provides the possibility of creating a fudge factor to correct count data that could be applied to the MARS reconstruction process as it currently exists. However, because a simultaneous reconstruction and MD carried out on projection data is currently under development, that procedure will probably not be attempted.

Foil fluorescence requires refinement to create a cleaner calibration for all pixels. MARS team members are currently working to improve the procedure and its per-pixel energy calibration will also await modification to the reconstruction algorithm before implementation.

Either technique will eventually lead to more accurate reconstruction and material decomposition.

7 Conclusion

7.1 Overview

This works most important results are the intrinsic and contrast enhanced images of biological samples scanned with an X-ray spectrum typical in actual human CT scans. The clear identification and histologic confirmation of a lipid core and spotty calcifications in an excised carotid atheroma using material reconstruction illustrates the potential for spectral CT in noninvasively identifying not just atherosclerosis, but any disease with abnormal lipid or calcification distributions. Lipid and spotty calcifications identified in the presence of gadolinium contrast mean that the benefits of contrast enhanced vascular imaging may be attainable simultaneously with the material identification of intrinsic biomarkers of atherosclerosis. Imaging and quantification of gold nanoparticle accumulation in a cancer tumour, the simultaneous identification of three contrasts, lipid and calcium in a mouse and MD of gold nanoparticle uptake by activated macrophages show the potential for contrast enhanced imaging of disease or injury with spectral CT; a potential that is limited only by the imagination of researchers in developing targeted and safe high-Z contrast agents.

The conditions of these scans were close to those needed for human *in vivo* imaging. Medical imaging is used to enhance life outcomes by identifying disease or injury and directing treatment. Spectral CT and material reconstruction will add improved and novel sources of information to the clinician's toolbox and the work described in this thesis is helping bring spectral CT to commercial use.

We have reached the above conclusions through two parallel lines of work that explored and improved the use of spectral CT with the MARS scanner to identify and quantify materials in biological samples. We explored the potential for intrinsic and contrast material measurements in biological samples using the filtered, higher energy X-ray spectrum typical in human CT scanning. Monitoring and refining the machine was performed in order to improve data and direct strategies for future improvements. Sample imaging experiments refined protocols, especially energy threshold placement, and demonstrated the accuracy of material identification spatially and quantitatively. The ability to quantify intrinsic and contrast materials in samples, simultaneously, has impacted Professor Steven Gieseg's research group's studies of macrophage activity in excised carotid atherosclerotic plaques [124] already and will impact clinical research and medical imaging in the future.

My technical developments improved the raw data by masking faulty pixels, narrowing energy resolution with per-pixel energy calibration (yet to be applied in practice), identifying X-ray tube current limitations in CSM, and demonstrating the need for proper X-ray tube warm-up. A simple graphing technique revealed the impact of the partial volume effect on material identification and will help developers account for this in future reconstruction techniques.

Imaging experiments with whole mice and excised carotid atheromas demonstrated accurate material segmentation and quantification on a spatial scale of 90 um voxels. Both intrinsic and contrast material identification was demonstrated. The potential in identifying diseases based on spatial arrangements of lipid, calcium and contrast agents was demonstrated within an atherosclerosis and a cancer model.

Spectral CT, in the form of the MARS small animal scanner, now, and soon, the MARS human scanner, measures the energy dependent attenuation patterns of a scanned volume and that data can be used to determine the spatial arrangement and concentrations of materials of interest. Quite simply, material reconstruction presents a new and possibly revolutionary dataset in clinical imaging. The diverse range of works described here in sample imaging and technical development encompass an overall goal of improved data quality and data assessment that leads to improved material imaging and demonstrations of the potential of material reconstructions in identifying disease states.

7.2 Review of achievements reported in this thesis

Chapters 1 and 2 provided a context for the research and development of spectral CT described in the thesis. The concept and potential value of material reconstruction using spectral X-ray CT datasets was described. Important specifics of the MARS scanner, MARS camera and MARS material reconstruction software were also detailed. K-edge imaging within a spectral CT environment was outlined including the potential uses of targeted high-Z contrast agents in conjunction with material reconstruction. Atherosclerosis and cancer were described briefly and their utility as testing models for intrinsic and contrast enhanced spectral CT was highlighted.

The progression of intrinsic material imaging for the quantification of lipid- and calcium-rich regions as biomarkers of atherosclerosis was given in Chapter 3. Studies presented there showed that using a filtered X-ray spectrum similar to that used in clinical human CT scans successfully identified necrotic lipid cores and spotty calcifications in excised carotid plaques. Both are highly correlated with plaques that rupture and identifying them with a noninvasive imaging technique may help to diagnose this notoriously silent disease before it causes severe clinical ischaemic events. Reconstruction at a $(90\ \mu m)^3$ voxel size is superior to current noninvasive imaging modalities and may allow detection of smaller and less advanced lesions before they are at risk of rupture. The potentials of CdTe and GaAs as sensor layers were both confirmed. SPM and CSM were both shown to provide sufficient spectral information for material identification of pathological lipid and calcium deposition. Issues were raised with respect to proper thresholding of lipid and calcium concentrations in viewing the MD data. The limitations imposed by a two component MD that prevents a simultaneous lipid and calcium measurement in the same voxel were illustrated. The importance of understanding the theoretical ability of MARS scanners to identify sub-voxel sized hydroxyapatite particle in atheromas was raised. Initial steps in moving to live sample imaging were also described for two summer student projects.

Chapter 4 added contrast agent quantification to continued intrinsic lipid and calcium measurements, again within the human relevant energy range over 30 keV. Phantom studies were used to test K-edge imaging of multiple contrasts. We showed that the K-factor and quantum signal proportion can be used to score various threshold combinations and that the scoring system was successful in choosing the optimal combination in the tested scenario. Various contrast enhanced scenarios were tested in biological samples. The physical outline of an excised carotid plaque submerged in gadolinium contrast agent was visible using proper windowing of the MD gadolinium concentrations. This important result highlights the potential uses of material reconstruction and the complex variety of viewing possibilities that may aid radiological assessment of disease and injury in contrast enhanced spectral CT. Furthermore, the lipid and calcium measurements were maintained in a contrast background compared to a scan of the plaque in air. The ability to simultaneously image clinically important intrinsic material distributions and use contrast agents to reveal additional signs of disease has important implications in reducing patient dose, number of procedures and costs. A subcutaneous Lewis lung carcinoma tumour in a mouse was imaged using gold nanoparticle accumulation via the EPR effect. Gold and bone are differentiated indicating that even tumours near bone could be viewed in detail with proper nanoparticle contrast targeting. The tumour size could be measured and the accumulated gold quantified. The ability to quantify spatial arrangements and concentrations opens myriad possibilities in assessing disease progression and regression over time, either with repeated procedures or contrasts designed to decay or be excreted in conjunction with physiologic changes. Lipid, calcium and three contrast agents were quantified simultaneously in a whole mouse. By proper compartmentalization of gadolinium to the gastrointestinal tract, gold to the vasculature and iodine to, predominantly, the kidneys and bladder, the accuracy of the spatial MD results for the contrasts and bone were easily verified. Again, the ability to use multiple contrast agents simultaneously with only one imaging procedure opens up a realm of diagnostic and research possibilities such as monitoring multiple diseases or different aspects of just one.

Contributions to machine functionality and data assessment are listed in Chapter 5. A pixel masking technique was developed and added to the MARS scanner control software. Two CT machines were commissioned with standardized testing that revealed faults in the X-ray source and camera while also providing information that lead to guidelines for scan protocols. A graphing technique comparing the Hounsfield unit values of voxels to the MD water concentration revealed the impact of the partial volume effect on MD segmentation and quantification of voxels near borders between materials of different density.

Chapter 6 describes two techniques for per pixel energy calibration. The broad spectrum energy offset technique uses the existing X-ray source to find an energy offset for each pixel from the global energy value at a given DAC and therefore, requires no special equipment or materials. It achieved a 28% reduction in full width half maximum of a measured fluorescence peak for molybdenum. The oblique fluorescence per-pixel energy calibration uses measures of off-axis fluorescence from monoatomic foils to directly map energy onto each pixel. Using fluorescence from molybdenum and lead, an energy calibration line for

each pixel can be calculated and experimental results were similar to the global calibration, indicating the quality of the measurements.

7.3 Opportunities and Issues for the Future

This work establishes the potential of spectral CT and material reconstructions in intrinsic and contrast identification using the higher energy X-ray spectrum typical in human scanning. But it also raises questions about how material reconstruction should be interpreted and points toward lines of research that can answer them. The ability to detect sub-voxel sized particles of high density such as hydroxyapatite deposition in atherosclerotic plaques or calcifications in some cancers and pseudogout could lead to much earlier diagnosis of these conditions and demands research establishing the confidence level of high Z measurements in the MD that are limited to single or small clusters of voxels. The same is true of contrast agents. As researchers develop sophisticated targeting mechanisms for high Z contrast agents like gold nanoparticles, spectral CT will develop in parallel with improving sensitivity. The lowest concentrations detectable should be constantly lowered by threshold optimization like that described here along with improved sensor purity, sensor to chip bonding, and chip electronics.

The known association of lipids and calcifications in atherosclerotic plaques that are highlighted in Chapter 3 also suggest that a 3 component MD should be a priority. Multiple contrast scans that result in mixing of contrast in the same voxel also suggest that more than two materials should be measured. Indeed MARS has a team of about six researchers investigating improved reconstruction methods, as are numerous teams worldwide. Calcium measurements in the presence of lipid are almost surely incorrect or completely missed, as evidenced by the results in Section 3.4 and Section 5.4. Alternatively, no lipid measurement is allowed currently when calcium is detected meaning that the true structure of calcified plaques cannot be assessed. Voxel material concentrations for at least three materials could solve these issues.

With superior spatial resolution to current clinical CT, the MARS scanner should be tested for imaging spatially important signs of disease. For instance, this thesis did not attempt to measure the fibrous cap thickness of plaque samples.

Material concentration thresholds will have to be established on a disease by disease basis. Lipid concentrations that are significant in atherosclerosis may mean little in assessing fatty liver disease. The detection of sub-voxel sized particles, whether calcifications in plaques or concentrated contrast agents in macrophages is surely possible but confidence levels and thresholding strategies will need to be investigated.

As we move into live animal scanning, dose measurements, which are not considered in this thesis, will be necessary. Likewise, reconstruction methods for moving, breathing subjects will also become vital. It is likely that many such issues will need to be solved before my results can be translated to the clinic.

References

1. Shamshad M (2017) Characterisation of the x-ray source and camera in the MARS spectral system. Ph.D., University of Otago

2. Anjomrouz M (2017) Investigation of MARS Spectral CT: X-ray Source and Detector Characterization. Ph.D., University of Otago

3. Doesburg, Robert M. N. (2012) The MARS Photon Processing Cameras for Spectral CT. University of Canterbury

4. Frojdh E, Ballabriga R, Campbell M, Fiederle M (2014) Count rate linearity and spectral response of the Medipix3RX chip coupled to a 300 mu m silicon sensor under high flux conditions. J Instrum 9: . doi: 10.1088/1748-0221/9/04/C04028

5. de Ruiter N (2014) Algorithms to process data from the MARS molecular imaging system. Ph.D., University of Otago

6. Bateman CJ (2014) Methods for material discrimination in MARS multi-energy CT. Ph.D., University of Otago

7. Chernoglazov A (2016) Tools for Visualising MARS Spectral CT Datasets

8. Campbell M, Heijne EHM, Meddeler G, et al (1998) A readout chip for a 64×64 pixel matrix with 15-bit single photon counting. IEEE Trans Nucl Sci 45:751–753 . doi: 10.1109/23.682629

9. Llopart X (2007) Design and characterization of 64K pixels chips working in single photon processing mode. Ph.D., Mid Sweden University

10. Ballabriga R, Campbell M, Heijne E, et al (2011) Medipix3: A 64 k pixel detector readout chip working in single photon counting mode with improved spectrometric performance. Nucl Instrum Methods Phys Res Sect Accel Spectrometers Detect Assoc Equip 633, Supplement 1:S15–S18 . doi: 10.1016/j.nima.2010.06.108

11. Ballabriga R, Alozy J, Campbell M, Fiederle M (2013) The Medipix3RX: a high resolution, zero dead-time pixel detector readout chip allowing spectroscopic imaging. J Instrum 8:C02016

12. Butler APH, Anderson NG, Tipples R, et al (2008) Bio-medical X-ray imaging with spectroscopic pixel detectors. Nucl Instrum Methods Phys Res Sect Accel Spectrometers Detect Assoc Equip 591:141–146 . doi: 10.1016/j.nima.2008.03.039

13. Campbell M, Alozy J, Ballabriga R, et al (2016) 38 - Single particle detection for spectroscopic CT and tracking in hadron therapy using Medipix chips. Radiother Oncol 118:S18–S19 . doi: 10.1016/S0167-8140(16)30038-X

14. Walsh, Michael F. (2014) Spectral Computed Tomography Development. University of Otago Christchurch

15. Rinkel J, Magalhães D, Wagner F, Frojdh E (2015) Equalization method for Medipix3RX. Nucl Inst Methods Phys Res A 801:1–6 . doi: 10.1016/j.nima.2015.08.029

16. Panta RK, Walsh MF, Bell ST, et al (2015) Energy Calibration of the Pixels of Spectral X-ray Detectors. IEEE Trans Med Imaging 34:697–706 . doi: 10.1109/TMI.2014.2337881

17. Koenig T, Hamann E, Procz S, Ballabriga R (2013) Charge Summing in Spectroscopic X-Ray Detectors With High-Z Sensors. IEEE Trans Nucl Sci 60:4713–4718 . doi: 10.1109/TNS.2013.2286672

18. Gimenez EN, Ballabriga R, Campbell M, et al (2011) Study of charge-sharing in MEDIPIX3 using a micro-focused synchrotron beam. J Instrum 6:C01031 . doi: 10.1088/1748-0221/6/01/C01031

19. Hounsfield GN (1973) Computerized transverse axial scanning (tomography): Part 1. Description of system. Br J Radiol 46:1016–1022 . doi: 10.1259/0007-1285-46-552-1016

20. de Wolff PM (1947) A theory of X-ray absorption in mixed powders. Physica 13:62–78 . doi: 10.1016/0031-8914(47)90069-4

21. Koningsberger DC, Prins R (eds) (1988) X-ray absorption: principles, applications, techniques of EXAFS, SEXAFS, and XANES

22. Brooks RA (1977) A Quantitative Theory of the Hounsfield Unit and Its Application to Dual Energy Scanning. J Comput Assist Tomogr 1:487–493

23. Anderson NG, Butler AP (2014) Clinical applications of spectral molecular imaging: potential and challenges. Contrast Media Mol Imaging 9:3–12 . doi: 10.1002/cmmi.1550

24. Pratt RH, RON A, TSENG HK (1973) Atomic Photoelectric Effect Above 10 keV. Rev Mod Phys 45:273–325 . doi: 10.1103/RevModPhys.45.273

25. Brambilla A, Gorecki A, Potop A, et al (2017) Basis material decomposition method for material discrimination with a new spectrometric X-ray imaging detector. J Instrum 12:P08014 . doi: 10.1088/1748-0221/12/08/P08014

26. Clark DP, Badea CT (2014) Spectral Diffusion: An Algorithm for Robust Material Decomposition of Spectral CT Data. Phys Med Biol 59:6445–6466 . doi: 10.1088/0031-9155/59/21/6445

27. Firsching M, Takoukam Talla P, Michel T, Anton G (2008) Material resolving X-ray imaging using spectrum reconstruction with Medipix2. Nucl Instrum Methods Phys Res Sect Accel Spectrometers Detect Assoc Equip 591:19–23 . doi: 10.1016/j.nima.2008.03.017

28. Zhang Y, Mou X, Wang G, Yu H (2017) Tensor-based Dictionary Learning for Spectral CT Reconstruction. IEEE Trans Med Imaging 36:142–154 . doi: 10.1109/TMI.2016.2600249

29. Lusic H, Grinstaff MW (2012) X-ray-Computed Tomography Contrast Agents. Chem Rev. doi: 10.1021/cr200358s

30. Cormode DP, Naha PC, Fayad ZA (2014) Nanoparticle contrast agents for computed tomography: a focus on micelles. Contrast Media Mol Imaging 9:37–52 . doi: 10.1002/cmmi.1551

31. Hahn MA, Singh AK, Sharma P, et al (2011) Nanoparticles as contrast agents for in-vivo bioimaging: current status and future perspectives. Anal Bioanal Chem 399:3–27 . doi: 10.1007/s00216-010-4207-5

32. Xi D, Dong S, Meng X, et al (2012) Gold nanoparticles as computerized tomography (CT) contrast agents. RSC Adv 2:12515–12524 . doi: 10.1039/C2RA21263C

33. Gormley AJ, Greish K, Ray A, et al (2011) Gold nanorod mediated plasmonic photothermal therapy: A tool to enhance macromolecular delivery. Int J Pharm 415:315–318 . doi: 10.1016/j.ijpharm.2011.05.068

34. Von Zur Muhlen C, Peter K, Ali ZA, et al (2008) Visualization of Activated Platelets by Targeted Magnetic Resonance Imaging Utilizing Conformation-Specific Antibodies against Glycoprotein IIb/IIIa. J Vasc Res 46:6–14

35. Raja AY (2013) Using MARS Spectral CT for Identifying Biomedical Nanoparticles. Ph.D., University of Canterbury

36. Ashton JR, West JL, Badea CT (2015) In vivo small animal micro-CT using nanoparticle contrast agents. Front Pharmacol 6: . doi: 10.3389/fphar.2015.00256

37. Smith BR, Gambhir SS (2017) Nanomaterials for In Vivo Imaging. Chem Rev 117:901–986 . doi: 10.1021/acs.chemrev.6b00073

38. Shilo M, Reuveni T, Motiei M, Popovtzer R (2012) Nanoparticles as computed tomography contrast agents: current status and future perspectives. Nanomedicine Lond 7:257–69 . doi: http://dx.doi.org.ezproxy.canterbury.ac.nz/10.2217/nnm.11.190

39. Hainfeld JF, Slatkin DN, Focella TM, Smilowitz HM (2006) Gold nanoparticles: a new X-ray contrast agent. Br J Radiol 79:248–253 . doi: 10.1259/bjr/13169882

40. Skajaa T, Cormode DP, Falk E, et al (2010) High-Density Lipoprotein–Based Contrast Agents for Multimodal Imaging of Atherosclerosis. Arterioscler Thromb Vasc Biol 30:169–176 . doi: 10.1161/ATVBAHA.108.179275

41. Kinsella JM, Jimenez RE, Karmali PP, et al (2011) X-Ray Computed Tomography Imaging of Breast Cancer by using Targeted Peptide-Labeled Bismuth Sulfide Nanoparticles. Angew Chem Int Ed 50:12308–12311 . doi: 10.1002/anie.201104507

42. Jiao P, Otto M, Geng Q, et al (2016) Enhancing both CT imaging and natural killer cell-mediated cancer cell killing by a GD2-targeting nanoconstruct. J Mater Chem B 4:513–520 . doi: 10.1039/C5TB02243F

43. Lozano R, Naghavi M, Foreman K, et al (2012) Global and regional mortality from 235 causes of death for 20 age groups in 1990 and 2010: a systematic analysis for the Global Burden of Disease Study 2010. The Lancet 380:2095–2128 . doi: 10.1016/S0140-6736(12)61728-0

44. Hopkins PN (2013) Molecular Biology of Atherosclerosis. Physiol Rev 93:1317–1542 . doi: 10.1152/physrev.00004.2012

45. Hansson GK, Libby P (2006) The immune response in atherosclerosis: a double-edged sword. Nat Rev Immunol 6:508–519 . doi: 10.1038/nri1882

46. Moore KJ, Sheedy FJ, Fisher EA (2013) Macrophages in atherosclerosis: a dynamic balance. Nat Rev Immunol 13:709–721 . doi: 10.1038/nri3520

47. Moore KJ, Tabas I (2011) Macrophages in the Pathogenesis of Atherosclerosis. Cell 145:341–355 . doi: 10.1016/j.cell.2011.04.005

48. Epstein FH, Ross R (1999) Atherosclerosis--An inflammatory disease. N Engl J Med 340:115–126

49. Libby P (2002) Inflammation in atherosclerosis. Nature 420:868–874 . doi: 10.1038/nature01323

50. Otsuka F, Kramer MCA, Woudstra P, et al (2015) Natural progression of atherosclerosis from pathologic intimal thickening to late fibroatheroma in human coronary arteries: A pathology study. Atherosclerosis 241:772–782 . doi: 10.1016/j.atherosclerosis.2015.05.011

51. Tabas I, Williams KJ, Borén J (2007) Subendothelial Lipoprotein Retention as the Initiating Process in Atherosclerosis Update and Therapeutic Implications. Circulation 116:1832–1844 . doi: 10.1161/CIRCULATIONAHA.106.676890

52. Arbab-Zadeh A, Fuster V (2015) The Myth of the “Vulnerable Plaque.” J Am Coll Cardiol 65:846–855 . doi: 10.1016/j.jacc.2014.11.041

53. Fishbein MC (2010) The vulnerable and unstable atherosclerotic plaque. Cardiovasc Pathol 19:6–11 . doi: 10.1016/j.carpath.2008.08.004

54. Naghavi M, Libby P, Falk E, et al (2003) From Vulnerable Plaque to Vulnerable Patient A Call for New Definitions and Risk Assessment Strategies: Part I. Circulation 108:1664–1672 . doi: 10.1161/01.CIR.0000087480.94275.97

55. Virmani R, Burke AP, Kolodgie FD, Farb A (2003) Pathology of the Thin-Cap Fibroatheroma: A Type of Vulnerable Plaque. J Intervent Cardiol 16:267–272

56. Narula J, Nakano M, Virmani R, et al (2013) Histopathologic Characteristics of Atherosclerotic Coronary Disease and Implications of the Findings for the Invasive and Noninvasive Detection of Vulnerable Plaques. J Am Coll Cardiol 61:1041–1051 . doi: 10.1016/j.jacc.2012.10.054

57. Redgrave JN, Gallagher P, Lovett JK, Rothwell PM (2008) Critical Cap Thickness and Rupture in Symptomatic Carotid Plaques The Oxford Plaque Study. Stroke 39:1722–1729 . doi: 10.1161/STROKEAHA.107.507988

58. Takaya N, Yuan C, Chu B, et al (2005) Presence of Intraplaque Hemorrhage Stimulates Progression of Carotid Atherosclerotic Plaques. Circulation 111:2768–2775 . doi: 10.1161/CIRCULATIONAHA.104.504167

59. Kips JG, Segers P, Van Bortel LM (2008) Identifying the vulnerable plaque: A review of invasive and non-invasive imaging modalities. Artery Res 2:21–34 . doi: 10.1016/j.artres.2007.11.002

60. Caussin C, Ohanessian A, Ghostine S, et al (2004) Characterization of vulnerable nonstenotic plaque with 16-Slice computed tomography compared with intravascular ultrasound. Am J Cardiol 94:99–104 . doi: 10.1016/j.amjcard.2004.03.036

61. Celeng C, Takx RA, Ferencik M, Maurovich-Horvat P (2016) Non-invasive and invasive imaging of vulnerable coronary plaque. Trends Cardiovasc Med Phila 26:538–547 . doi: http://dx.doi.org.ezproxy.canterbury.ac.nz/10.1016/j.tcm.2016.03.005

62. Choi B-J, Kang D-K, Tahk S-J, et al (2008) Comparison of 64-slice multidetector computed tomography with spectral analysis of intravascular ultrasound backscatter signals for

characterizations of noncalcified coronary arterial plaques. Am J Cardiol 102:988–993 . doi: 10.1016/j.amjcard.2008.05.060

63. Kim SY, Kim K-S, Seung MJ, et al (2010) The culprit lesion score on multi-detector computed tomography can detect vulnerable coronary artery plaque. Int J Cardiovasc Imaging 26:245–252 . doi: 10.1007/s10554-010-9712-2

64. Pedersen SF, Hag AMF, Klausen TL, et al (2014) Positron emission tomography of the vulnerable atherosclerotic plaque in man - a contemporary review. Clin Physiol Funct Imaging 34:413–425 . doi: 10.1111/cpf.12105

65. Soloperto G, Casciaro S (2012) Progress in atherosclerotic plaque imaging. World J Radiol 4:353–371 . doi: 10.4329/wjr.v4.i8.353

66. Tan KT, Lip GYH (2008) Imaging of the unstable plaque. Int J Cardiol 127:157–165 . doi: 10.1016/j.ijcard.2007.11.054

67. Tearney GJ, Yabushita H, Houser SL, et al (2003) Quantification of Macrophage Content in Atherosclerotic Plaques by Optical Coherence Tomography. Circulation 107:113–119 . doi: 10.1161/01.CIR.0000044384.41037.43

68. Wintermark M, Jawadi SS, Rapp JH, et al (2008) High-Resolution CT Imaging of Carotid Artery Atherosclerotic Plaques. Am J Neuroradiol 29:875–882 . doi: 10.3174/ajnr.A0950

69. Pini R, Faggioli G, Fittipaldi S, et al (2017) Relationship between Calcification and Vulnerability of the Carotid Plaques. Ann Vasc Surg. doi: 10.1016/j.avsg.2017.04.017

70. Vengrenyuk Y, Carlier S, Xanthos S, et al (2006) A hypothesis for vulnerable plaque rupture due to stress-induced debonding around cellular microcalcifications in thin fibrous caps. Proc Natl Acad Sci U S A 103:14678–14683 . doi: 10.1073/pnas.0606310103

71. Wong KK, Thavornpattanapong P, Cheung SC, et al (2012) Effect of calcification on the mechanical stability of plaque based on a three-dimensional carotid bifurcation model. BMC Cardiovasc Disord 12:1–18 . doi: 10.1186/1471-2261-12-7

72. Ehara S, Kobayashi Y, Yoshiyama M, et al (2004) Spotty Calcification Typifies the Culprit Plaque in Patients With Acute Myocardial Infarction An Intravascular Ultrasound Study. Circulation 110:3424–3429 . doi: 10.1161/01.CIR.0000148131.41425.E9

73. Han RI, Wheeler TM, Lumsden AB, et al (2016) Morphometric analysis of calcification and fibrous layer thickness in carotid endarterectomy tissues. Comput Biol Med 70:210–219 . doi: 10.1016/j.compbiomed.2016.01.019

74. Kataoka Y, Wolski K, Uno K, et al (2012) Spotty Calcification as a Marker of Accelerated Progression of Coronary AtherosclerosisInsights From Serial Intravascular Ultrasound. J Am Coll Cardiol 59:1592–1597 . doi: 10.1016/j.jacc.2012.03.012

75. Kelly-Arnold A, Maldonado N, Laudier D, et al (2013) Revised microcalcification hypothesis for fibrous cap rupture in human coronary arteries. Proc Natl Acad Sci 110:10741–10746 . doi: 10.1073/pnas.1308814110

76. Maldonado N, Kelly-Arnold A, Laudier D, et al (2015) Imaging and analysis of microcalcifications and lipid/necrotic core calcification in fibrous cap atheroma. Int J Cardiovasc Imaging 31:1079–1087 . doi: 10.1007/s10554-015-0650-x

77. Mauriello A, Servadei F, Zoccai GB, et al (2013) Coronary calcification identifies the vulnerable patient rather than the vulnerable Plaque. Atherosclerosis 229:124–129 . doi: 10.1016/j.atherosclerosis.2013.03.010

78. Cardoso L, Weinbaum S (2014) Changing Views of the Biomechanics of Vulnerable Plaque Rupture: A Review. Ann Biomed Eng 42:415–431 . doi: 10.1007/s10439-013-0855-x

79. What Is Cancer? In: Natl. Cancer Inst. https://www.cancer.gov/about-cancer/understanding/what-is-cancer. Accessed 12 Nov 2017

80. Hanahan D, Weinberg RA (2011) Hallmarks of Cancer: The Next Generation. Cell 144:646–674 . doi: 10.1016/j.cell.2011.02.013

81. Sohaib SA (2015) CT of splenic disease. Cancer Imaging 2:101 . doi: 10.1102/1470-7330.2002.0012

82. O'Connell A, Conover DL, Zhang Y, et al (2010) Cone-Beam CT for Breast Imaging: Radiation Dose, Breast Coverage, and Image Quality. Am J Roentgenol 195:496–509 . doi: 10.2214/AJR.08.1017

83. Moro K, Nagahashi M, Hirashima K, et al (2017) Benign esophageal schwannoma: a brief overview and our experience with this rare tumor. Surg Case Rep 3:97 . doi: 10.1186/s40792-017-0369-0

84. Javadi S, Menias CO, Korivi BR, et al (2017) Pancreatic Calcifications and Calcified Pancreatic Masses: Pattern Recognition Approach on CT. Am J Roentgenol 209:77–87 . doi: 10.2214/AJR.17.17862

85. Clark DP, Ghaghada K, Moding EJ, et al (2013) In vivo characterization of tumor vasculature using iodine and gold nanoparticles and dual energy micro-CT. Phys Med Biol 58:1683–1704 . doi: 10.1088/0031-9155/58/6/1683

86. Savai R, Langheinrich AC, Schermuly RT, et al (2009) Evaluation of angiogenesis using micro-computed tomography in a xenograft mouse model of lung cancer. Neoplasia 11:48–56

87. Kim D, Jeong YY, Jon S (2010) A Drug-Loaded Aptamer−Gold Nanoparticle Bioconjugate for Combined CT Imaging and Therapy of Prostate Cancer. ACS Nano 4:3689–3696 . doi: 10.1021/nn901877h

88. Popovtzer R, Agrawal A, Kotov NA, et al (2008) Targeted Gold Nanoparticles Enable Molecular CT Imaging of Cancer. Nano Lett 8:4593–4596 . doi: 10.1021/nl8029114

89. Wolf P, Freudenberg N, Bühler P, et al (2010) Three conformational antibodies specific for different PSMA epitopes are promising diagnostic and therapeutic tools for prostate cancer. The Prostate 70:562–569 . doi: 10.1002/pros.21090

90. Jain S, Hirst DG, O'Sullivan JM (2012) Gold nanoparticles as novel agents for cancer therapy. Br J Radiol 85:101–113 . doi: 10.1259/bjr/59448833

91. R.D. Deslattes, E.G. Kessler Jr., P. Indelicato, et al (2009) X-Ray Transition Energies Database. In: NIST. https://www.nist.gov/pml/x-ray-transition-energies-database. Accessed 31 May 2017

92. Bambynek W, Crasemann B, Fink RW, et al (1972) X-Ray Fluorescence Yields, Auger, and Coster-Kronig Transition Probabilities. Rev Mod Phys 44:716–813 . doi: 10.1103/RevModPhys.44.716

93. McQueen FM, Doyle A, Dalbeth N (2011) Imaging in gout - What can we learn from MRI, CT, DECT and US? Arthritis Res Ther 13:246 . doi: 10.1186/ar3489

94. Adams LA, Angulo P, Lindor KD (2005) Nonalcoholic fatty liver disease. Can Med Assoc J 172:899–905 . doi: 10.1503/cmaj.045232

95. Burger PC, Heinz ER, Shibata T, Kleihues P (1988) Topographic anatomy and CT correlations in the untreated glioblastoma multiforme. J Neurosurg 68:698–704 . doi: 10.3171/jns.1988.68.5.0698

96. Bushberg JT, Seibert JA, Leidholdt EM, Boone JM (2011) The Essential Physics of Medical Imaging, Third. LIppincott Williams & Wilkins

97. Aamir R, Chernoglazov A, Bateman CJ, et al (2014) MARS spectral molecular imaging of lamb tissue: data collection and image analysis. J Instrum 9:P02005–P02005 . doi: 10.1088/1748-0221/9/02/P02005

98. Ding H, Ducote JL, Molloi S (2013) Measurement of breast tissue composition with dual energy cone-beam computed tomography: A postmortem study. Med Phys 40:n/a-n/a . doi: 10.1118/1.4802734

99. Hamann E, Koenig T, Zuber M, et al (2015) Performance of a Medipix3RX Spectroscopic Pixel Detector With a High Resistivity Gallium Arsenide Sensor. IEEE Trans Med Imaging 34:707–715 . doi: 10.1109/TMI.2014.2317314

100. Zainon R, Ronaldson JP, Janmale T, et al (2012) Spectral CT of carotid atherosclerotic plaque: comparison with histology. Eur Radiol 22:2581–2588 . doi: 10.1007/s00330-012-2538-7

101. Panta RK, Bateman CJ, Healy JL, et al (2013) Simultaneous discrimination of multiple intrinsic bio-markers in excised atheroma with spectral molecular imaging. N Z Med J 126:1375

102. Sıdır İ, Gülseven Sıdır Y (2015) Estimation of ground and excited state dipole moments of Oil Red O by solvatochromic shift methods. Spectrochim Acta A Mol Biomol Spectrosc 135:560–567 . doi: 10.1016/j.saa.2014.07.049

103. Hirsch D, Azoury R, Sarig S, Kruth HS (1993) Colocalization of cholesterol and hydroxyapatite in human atherosclerotic lesions. Calcif Tissue Int 52:94–98 . doi: 10.1007/BF00308315

104. Panta RK (2015) Toward human MARS scanning: improving spectral performance for soft tissue imaging. Ph.D., University of Otago Christchurch

105. Ballabriga R, Alozy J, Campbell M, et al (2016) Review of hybrid pixel detector readout ASICs for spectroscopic X-ray imaging. J Instrum 11:P01007 . doi: 10.1088/1748-0221/11/01/P01007

106. Koenig T, Schulze J, Zuber M, et al (2012) Imaging properties of small-pixel spectroscopic x-ray detectors based on cadmium telluride sensors. Phys Med Biol 57:6743 . doi: 10.1088/0031-9155/57/21/6743

107. Mainprize JG, Hunt DC, Yaffe MJ (2002) Direct conversion detectors: The effect of incomplete charge collection on detective quantum efficiency. Med Phys 29:976–990 . doi: 10.1118/1.1477235

108. Ruiz JL, Weinbaum S, Aikawa E, Hutcheson JD (2016) Zooming in on the genesis of atherosclerotic plaque microcalcifications: Microcalcifications and atherosclerotic plaque rupture. J Physiol 594:2915–2927 . doi: 10.1113/JP271339

109. Joseph L Healy (2015) Differentiating lipid, water and calcium-rich regions within atherosclerotic plaques using multi-energy CT

110. Poludniowski G, Landry G, DeBlois F, et al (2009) SpekCalc: a program to calculate photon spectra from tungsten anode x-ray tubes. Phys Med Biol 54:N433 . doi: 10.1088/0031-9155/54/19/N01

111. Poludniowski GG, Evans PM (2007) Calculation of x-ray spectra emerging from an x-ray tube. Part I. Electron penetration characteristics in x-ray targets. Med Phys 34:2164–2174 . doi: 10.1118/1.2734725

112. Poludniowski GG (2007) Calculation of x-ray spectra emerging from an x-ray tube. Part II. X-ray production and filtration in x-ray targets. Med Phys 34:2175–2186 . doi: 10.1118/1.2734726

113. Sarig S, Weiss T, Katz I, et al (1994) Detection of cholesterol associated with calcium mineral using confocal fluorescence microscopy. Lab Investig J Tech Methods Pathol 71:782–787

114. Mitchinson MJ, Hothersall DC, Brooks PN, De Burbure CY (1985) The distribution of ceroid in human atherosclerosis. J Pathol 145:177–183 . doi: 10.1002/path.1711450205

115. Kruth HS (1984) Localization of unesterified cholesterol in human atherosclerotic lesions. Demonstration of filipin-positive, oil-red-O-negative particles. Am J Pathol 114:201–208

116. Hurrell MA, Butler APH, Cook NJ, et al (2012) Spectral Hounsfield units: a new radiological concept. Eur Radiol 22:1008–1013 . doi: 10.1007/s00330-011-2348-3

117. Woodard HQ, White DR (1986) The composition of body tissues. Br J Radiol 59:1209–1218 . doi: 10.1259/0007-1285-59-708-1209

118. Fowler SD, Greenspan P (1985) Application of Nile red, a fluorescent hydrophobic probe, for the detection of neutral lipid deposits in tissue sections: comparison with oil red O. J Histochem Cytochem 33:833–836 . doi: 10.1177/33.8.4020099

119. NIST X-Ray Form Factor, Atten. Scatt. Tables Form Page. https://physics.nist.gov/PhysRefData/FFast/html/form.html. Accessed 31 Oct 2017

120. Ferencik M, Schlett CL, Ghoshhajra BB, et al (2012) A Computed Tomography-Based Coronary Lesion Score to Predict Acute Coronary Syndrome Among Patients With Acute Chest Pain and Significant Coronary Stenosis on Coronary Computed Tomographic Angiogram. Am J Cardiol 110:183–189 . doi: 10.1016/j.amjcard.2012.02.066

121. Wang J, Garg N, Duan X, et al (2011) Quantification of iron in the presence of calcium with dual-energy computed tomography (DECT) in an ex vivo porcine plaque model. Phys Med Biol 56:7305 . doi: 10.1088/0031-9155/56/22/019

122. Yonetsu T, Kakuta T, Lee T, et al (2011) In vivo critical fibrous cap thickness for rupture-prone coronary plaques assessed by optical coherence tomography. Eur Heart J 32:1251–1259 . doi: 10.1093/eurheartj/ehq518

123. Janmale T, Genet R, Crone E, et al (2015) Neopterin and 7,8-dihydroneopterin are generated within atherosclerotic plaques. Pteridines 26:93–103 . doi: 10.1515/pterid-2015-0004

124. Prebble H, Cross S, Marks E, et al Induced macrophage activation in live excised atherosclerotic plaque. Immunobiology. doi: 10.1016/j.imbio.2018.03.002

125. Pietrobelli A, Formica C, Wang Z, Heymsfield SB (1996) Dual-energy X-ray absorptiometry body composition model: review of physical concepts. Am J Physiol - Endocrinol Metab 271:E941–E951

126. Bodanapally UK, Dreizin D, Issa G, et al (2017) Dual-Energy CT in Enhancing Subdural Effusions that Masquerade as Subdural Hematomas: Diagnosis with Virtual High-Monochromatic (190-keV) Images. Am J Neuroradiol 38:1946–1952 . doi: 10.3174/ajnr.A5318

127. Abraham JL, Higgins CB, Newell JD (1980) Uptake of iodinated contrast material in ischemic myocardium as an indicator of loss of cellular membrane integrity. Am J Pathol 101:319–330

128. Adam J-F, Elleaume H, Joubert A, et al (2003) Synchrotron radiation therapy of malignant brain glioma loaded with an iodinated contrast agent: First trial on rats bearing F98 gliomas. Int J Radiat Oncol 57:1413–1426 . doi: 10.1016/j.ijrobp.2003.07.007

129. Cademartiri F, Mollet NR, van der Lugt A, et al (2005) Intravenous Contrast Material Administration at Helical 16–Detector Row CT Coronary Angiography: Effect of Iodine Concentration on Vascular Attenuation. Radiology 236:661–665 . doi: 10.1148/radiol.2362040468

130. Bae KT, McDermott R, Gierada DS, et al (2004) Gadolinium-enhanced computed tomography angiography in multi-detector row computed tomography: initial observations1. Acad Radiol 11:61–68 . doi: 10.1016/S1076-6332(03)00536-1

131. Gierada DS, Bae KT (1999) Gadolinium as a CT Contrast Agent: Assessment in a Porcine Model. Radiology 210:829–834

132. Boote E, Fent G, Kattumuri V, et al (2010) Gold Nanoparticle Contrast in a Phantom and Juvenile Swine: Models for Molecular Imaging of Human Organs using X-ray Computed Tomography. Acad Radiol 17:410–417 . doi: 10.1016/j.acra.2010.01.006

133. Danila D, Johnson E, Kee P CT Imaging of Myocardial Scars with Collagen-targeting Gold Nanoparticles. Nanomedicine Nanotechnol Biol Med. doi: 10.1016/j.nano.2013.03.009

134. Sadauskas E, Danscher G, Stoltenberg M, et al (2009) Protracted elimination of gold nanoparticles from mouse liver. Nanomedicine Nanotechnol Biol Med 5:162–169 . doi: 10.1016/j.nano.2008.11.002

135. Maeda H (2010) Tumor-Selective Delivery of Macromolecular Drugs via the EPR Effect: Background and Future Prospects. Bioconjug Chem 21:797–802 . doi: 10.1021/bc100070g

136. He P, Wei B, Cong W, Wang G (2012) Optimization of K-edge imaging with spectral CT. Med Phys 39:6572–6579 . doi: 10.1118/1.4754587

137. He P, Wei B, Feng P, et al (2013) Material Discrimination Based on K-edge Characteristics. Comput Math Methods Med 2013: . doi: 10.1155/2013/308520

138. Panta RK, Bell ST, Healy JL, et al (2018) Element-specific spectral imaging of multiple contrast agents: a phantom study. J Instrum 13:T02001 . doi: 10.1088/1748-0221/13/02/T02001

139. Moghiseh M, Raja A, Panta RK, et al (2016) Discrimination of Multiple High-Z Materials by MultiEnergy Spectral CT– A Phantom Study. JSM Biomed Imaging Data Pap 3:1007

140. Cai J, Hatsukami TS, Ferguson MS, et al (2005) In Vivo Quantitative Measurement of Intact Fibrous Cap and Lipid-Rich Necrotic Core Size in Atherosclerotic Carotid Plaque Comparison of High-Resolution, Contrast-Enhanced Magnetic Resonance Imaging and Histology. Circulation 112:3437–3444 . doi: 10.1161/CIRCULATIONAHA.104.528174

141. Sandfort V, Lima JAC, Bluemke DA (2015) Noninvasive Imaging of Atherosclerotic Plaque Progression: Status of Coronary Computed Tomography Angiography. Circ Cardiovasc Imaging 8:e003316 . doi: 10.1161/CIRCIMAGING.115.003316

142. Yuan Chun, Kerwin William S., Ferguson Marina S., et al (2002) Contrast-enhanced high resolution MRI for atherosclerotic carotid artery tissue characterization. J Magn Reson Imaging 15:62–67 . doi: 10.1002/jmri.10030

143. Pourmorteza A, Symons R, Sandfort V, et al (2016) Abdominal Imaging with Contrast-enhanced Photon-counting CT: First Human Experience. Radiology 279:239–245 . doi: 10.1148/radiol.2016152601

144. Silva JM de S e, Utsch J, Kimm MA, et al (2017) Dual-energy micro-CT for quantifying the time-course and staining characteristics of ex-vivo animal organs treated with iodine- and gadolinium-based contrast agents. Sci Rep 7:17387 . doi: 10.1038/s41598-017-17064-z

145. Sun Z (2014) Atherosclerosis and Atheroma Plaque Rupture: Imaging Modalities in the Visualization of Vasa Vasorum and Atherosclerotic Plaques. Sci World J 2014:e312764 . doi: 10.1155/2014/312764

146. Michel J-B, Martin-Ventura JL, Nicoletti A, Ho-Tin-Noé B (2014) Pathology of human plaque vulnerability: Mechanisms and consequences of intraplaque haemorrhages. Atherosclerosis 234:311–319 . doi: 10.1016/j.atherosclerosis.2014.03.020

147. Nishida N, Yano H, Nishida T, et al (2006) Angiogenesis in Cancer. Vasc Health Risk Manag 2:213–219

148. Nagy JA, Chang S-H, Shih S-C, et al (2010) Heterogeneity of the Tumor Vasculature. Semin Thromb Hemost 36:321–331 . doi: 10.1055/s-0030-1253454

149. Carmeliet P, Jain RK (2000) Angiogenesis in cancer and other diseases. Nat Lond 407:249–57 . doi: http://dx.doi.org.ezproxy.canterbury.ac.nz/10.1038/35025220

150. Sarin H (2010) Physiologic upper limits of pore size of different blood capillary types and another perspective on the dual pore theory of microvascular permeability. J Angiogenesis Res 2:14 . doi: 10.1186/2040-2384-2-14

151. Matsumura Y, Maeda H (1986) A New Concept for Macromolecular Therapeutics in Cancer Chemotherapy: Mechanism of Tumoritropic Accumulation of Proteins and the Antitumor Agent Smancs. Cancer Res 46:6387–6392

152. Maeda H (2012) Macromolecular therapeutics in cancer treatment: The EPR effect and beyond. J Controlled Release 164:138–144 . doi: 10.1016/j.jconrel.2012.04.038

153. Ventola CL (2017) Progress in Nanomedicine: Approved and Investigational Nanodrugs. Pharm Ther 42:742–755

154. Connor Ellen E., Mwamuka Judith, Gole Anand, et al (2005) Gold Nanoparticles Are Taken Up by Human Cells but Do Not Cause Acute Cytotoxicity. Small 1:325–327 . doi: 10.1002/smll.200400093

155. Khlebtsov N, Dykman L (2011) Biodistribution and toxicity of engineered gold nanoparticles: a review of in vitro and in vivo studies. Chem Soc Rev 40:1647–1671 . doi: 10.1039/C0CS00018C

156. Jenkins JT, Halaney DL, Sokolov KV, et al (2013) Excretion and toxicity of gold–iron nanoparticles. Nanomedicine Nanotechnol Biol Med 9:356–365 . doi: 10.1016/j.nano.2012.08.007

157. 1115A AuroVist -15 nm X-ray Contrast Agent: Instructions and Protocols. http://www.nanoprobes.com/instructions/Inf1115-AuroVist-II-15-nm-Instructions.html. Accessed 26 Mar 2018

158. Moghiseh M (2017) Optimisation of spectral CT for novel applications of nano-particles. Ph.D., University of Otago Christchurch

159. Zhang Z, D. Ross R, K. Roeder R (2010) Preparation of functionalized gold nanoparticles as a targeted X-ray contrast agent for damaged bone tissue. Nanoscale 2:582–586 . doi: 10.1039/B9NR00317G

160. Hainfeld JF, O'Connor MJ, Dilmanian FA, et al (2011) Micro-CT enables microlocalisation and quantification of Her2-targeted gold nanoparticles within tumour regions. Br J Radiol 84:526–533 . doi: 10.1259/bjr/42612922

161. Rajendran K, Löbker C, Schon BS, et al (2016) Quantitative imaging of excised osteoarthritic cartilage using spectral CT. Eur Radiol 1–9 . doi: 10.1007/s00330-016-4374-7

162. Riches AC, Sharp JG, Thomas DB, Smith SV (1973) Blood volume determination in the mouse. J Physiol 228:279–284

163. Hashimoto M, Sasaki JI, Yamaguchi S, et al (2015) Gold Nanoparticles Inhibit Matrix Metalloproteases without Cytotoxicity. J Dent Res 0022034515589282 . doi: 10.1177/0022034515589282

164. von Elverfeldt D, Meißner M, Peter K, et al (2012) An approach towards molecular imaging of activated platelets allows imaging of symptomatic human carotid plaques in a new model of a tissue flow chamber. Contrast Media Mol Imaging 7:204–213 . doi: 10.1002/cmmi.482

165. Schlepper-Schäfer J, Hülsmann D, Djovkar A, et al (1986) Endocytosis via galactose receptors in vivo. Ligand size directs uptake by hepatocytes and/or liver macrophages. Exp Cell Res 165:494–506

166. Rieg T (2013) A High-throughput Method for Measurement of Glomerular Filtration Rate in Conscious Mice. J Vis Exp JoVE. doi: 10.3791/50330

167. Symons Rolf, Krauss Bernhard, Sahbaee Pooyan, et al (2017) Photon-counting CT for simultaneous imaging of multiple contrast agents in the abdomen: An in vivo study. Med Phys 44:5120–5127 . doi: 10.1002/mp.12301

168. Cormode DP, Si-Mohamed S, Bar-Ness D, et al (2017) Multicolor spectral photon-counting computed tomography: in vivo dual contrast imaging with a high count rate scanner. Sci Rep 7: . doi: 10.1038/s41598-017-04659-9

169. Davies MJ, Richardson PD, Woolf N, et al (1993) Risk of thrombosis in human atherosclerotic plaques: role of extracellular lipid, macrophage, and smooth muscle cell content. Br Heart J 69:377–381 . doi: 10.1136/hrt.69.5.377

170. Shchepetkina AA, Hock BD, Miller A, et al (2017) Effect of 7,8-dihydroneopterin mediated CD36 down regulation and oxidant scavenging on oxidised low-density lipoprotein induced cell death in human macrophages. Int J Biochem Cell Biol 87:27–33 . doi: 10.1016/j.biocel.2017.03.017

171. Cormode DP, Roessl E, Thran A, et al (2010) Atherosclerotic Plaque Composition: Analysis with Multicolor CT and Targeted Gold Nanoparticles. Radiology 256:774–782 . doi: 10.1148/radiol.10092473

172. Atharifard A, Healy JL, Goulter BP, et al (2017) Per-pixel energy calibration of photon counting detectors. J Instrum 12:C03085 . doi: 10.1088/1748-0221/12/03/C03085

173. Atharifard A (2017) Characterization of X-ray Detectors for MARS Spectral CT Technology. Ph.D., University of Otago Christchurch

174. Langheinrich AC, Kampschulte M, Cröβmann C, et al (2009) Role of computed tomography voxel size in detection and discrimination of calcium and iron deposits in atherosclerotic human coronary artery specimens. J Comput Assist Tomogr 33:517

175. Fröjdh C, Krapohl D, Reza S, et al (2013) Spectral resolution in pixel detectors with single photon processing. pp 88520O-88520O–12

176. Gimenez EN, Ballabriga R, Campbell M, et al (2011) Characterization of Medipix3 With Synchrotron Radiation. IEEE Trans Nucl Sci 58:323–332 . doi: 10.1109/TNS.2010.2089062

177. Uher J, Harvey G, Jakubek J (2012) X-Ray Fluorescence Imaging With the Medipix2 Single-Photon Counting Detector. IEEE Trans Nucl Sci 59:54–61 . doi: 10.1109/TNS.2011.2173352

178. Broeke LV, Atharifard A, Goulter BP, et al (2016) Oblique fluorescence in a MARS scanner with a CdTe-Medipix3RX. J Instrum 11:C12063 . doi: 10.1088/1748-0221/11/12/C12063

179. Nieuwenhove VV, Beenhouwer JD, Carlo FD, et al (2015) Dynamic intensity normalization using eigen flat fields in X-ray imaging. Opt Express 23:27975–27989 . doi: 10.1364/OE.23.027975

180. Muhammad Shamshad Semi-analytic x-ray source model for mars spectral CT

181. Vanden Broeke L (2015) Foil fluorescence in MARS spectral imaging. Master's, University of Canterbury

182. Scofield JH (1973) Theoretical Photoionization Cross Sections from 1 to 1500 Kev. CALIFORNIA UNIV., LIVERMORE. LAWRENCE LIVERMORE LAB.

183. Suplee C (2009) XCOM: Photon Cross Sections Database. In: NIST. https://www.nist.gov/pml/xcom-photon-cross-sections-database. Accessed 29 Nov 2017

184. Butler AP, Butler PH, Bell ST, et al (2015) Measurement of the energy resolution and calibration of hybrid pixel detectors with GaAs:Cr sensor and Timepix readout chip. Phys Part Nucl Lett 12:59–73 . doi: 10.1134/S1547477115010021

185. Tran CQ, Jonge MD de, Barnea Z, Chantler CT (2004) Absolute determination of the effect of scattering and fluorescence on x-ray attenuation measurements. J Phys B At Mol Opt Phys 37:3163–3176 . doi: 10.1088/0953-4075/37/15/011